

**Comparison of cloud systems simulated with two-dimensional and  
three-dimensional cloud resolving models**

by

**Justin A. Covert**

A thesis submitted to the graduate faculty  
in partial fulfillment of the requirements for the degree of  
**MASTER OF SCIENCE**

**Major: Meteorology**

Program of Study Committee:  
Xiaoqing Wu, Major Professor  
William Gallus  
Andy VanLoocke

The student author, whose presentation of the scholarship herein was approved by the program of study committee, is solely responsible for the content of this thesis. The Graduate College will ensure this thesis is globally accessible and will not permit alterations after a degree is conferred.

Iowa State University

Ames, Iowa

2019

Copyright © Justin A. Covert, 2019. All rights reserved.

## TABLE OF CONTENTS

	Page
LIST OF TABLES .....	iv
LIST OF FIGURES .....	v
ACKNOWLEDGMENTS .....	vii
ABSTRACT .....	viii
CHAPTER 1. INTRODUCTION .....	1
CHAPTER 2. CLOUD RESOLVING MODELS AND EXPERIMENTAL DESIGN .....	8
2.1 Models .....	8
2.2 Large Scale Forcing .....	9
2.3 Wind and Surface Fluxes .....	10
2.4 Observational Data .....	10
2.5 Methodology .....	12
CHAPTER 3. BASIC ATMOSPHERIC PROPERTIES .....	13
3.1 Temperature .....	13
3.2 Moisture .....	13
3.3 Precipitation .....	14
3.4 Radiative Fluxes and Radiative Heating Tendencies .....	14
CHAPTER 4. CLOUD PROPERTIES AND DYNAMICS .....	16
4.1 Cloud Mass Fluxes .....	16
4.2 Cloud Fraction .....	16
4.3 Cloud Top Frequency .....	17
4.4 Liquid Water Path/Ice Water Path .....	17
4.5 Cloud Water/Ice Content .....	18
4.6 Momentum Transport .....	19
4.7 Apparent Momentum Source .....	20
4.8 Energy Conversion .....	21
CHAPTER 5. CLOUD THERMODYNAMICS .....	24
5.1 Heat Source ( $Q_1$ ) and Moisture Sink ( $Q_2$ ) .....	24
5.2 Energy from Phase Changes .....	26
CHAPTER 6. COMPARISON OF CONVECTIVE AND NON-CONVECTIVE CLOUDS .....	28
6.1 Precipitation .....	28
6.2 Vertical Motion .....	29
6.3 Cloud Mass Fluxes .....	29
6.4 Heat Source ( $Q_1$ ) and Moisture Sink ( $Q_2$ ) .....	30

6.5 Energy from Phase Changes.....	30
6.6 Apparent Momentum Source.....	31
6.7 Pressure Gradient, Subsidence, and Detrainment.....	31
 CHAPTER 7. DISCUSSION AND CONCLUSIONS .....	 33
REFERENCES .....	86

**LIST OF TABLES**

	Page
Table 1. Mean and standard deviation values of simulated radiative fluxes .....	85
Table 2. Mean and standard deviation values of simulated phase change heating terms .....	85

## LIST OF FIGURES

	Page
Figure 1. Domain of the DYNAMO field campaign .....	39
Figure 2. Large scale forcing time series.....	40
Figure 3. Zonal wind time series.....	41
Figure 4. Meridional wind time series .....	42
Figure 5. Sea surface temperature and sensible/latent heat flux time series.....	43
Figure 6. Temperature bias time series .....	44
Figure 7. Moisture bias time series .....	45
Figure 8. Budget-derived and observed precipitation time series.....	46
Figure 9. Top of the atmosphere radiative fluxes time series .....	47
Figure 10. Surface radiative fluxes time series.....	48
Figure 11. Vertical profile of surface shortwave and longwave heating tendencies .....	49
Figure 12. Updraft mass flux time series .....	50
Figure 13. Downdraft mass flux time series .....	51
Figure 13. Cloud fraction time series.....	52
Figure 15. Cloud fraction vertical profile .....	53
Figure 16. Cloud top frequency time series .....	54
Figure 17. Liquid water path and ice water path time series .....	55
Figure 18. Total cloud water content vertical profile .....	56
Figure 19. Cloud water and cloud ice vertical profile .....	57
Figure 20. Momentum flux time series.....	58
Figure 21. Momentum flux vertical profile for the u-component.....	59
Figure 22. Apparent momentum source time series .....	60

Figure 23. Apparent momentum source vertical profile .....	61
Figure 24. Mean K to eddy K conversion vertical profile .....	62
Figure 25. Mean K to eddy K conversion time series.....	63
Figure 26. Pot. to eddy K conversion vertical profile.....	64
Figure 27. Pot. to eddy K conversion time series .....	65
Figure 28. Heat source ( $Q_1$ ) time series .....	66
Figure 29. Moisture sink ( $Q_2$ ) time series .....	67
Figure 30. Heat source ( $Q_1$ ) vertical profile.....	68
Figure 31. Moisture sink ( $Q_2$ ) vertical profile .....	69
Figure 32. Phase change heating terms vertical profile .....	70
Figure 33. Precipitation rate and areal coverage of precipitation time series for convective and non-convective clouds .....	71
Figure 34. Vertical velocity within convective clouds vertical profile.....	72
Figure 35. Vertical velocity within non-convective clouds vertical profile .....	73
Figure 36. Cloud mass flux within convective clouds vertical profile .....	74
Figure 37. Cloud mass flux within non-convective clouds vertical profile .....	75
Figure 38. $Q_1$ and $Q_2$ vertical profiles within convective clouds.....	76
Figure 39. $Q_1$ and $Q_2$ vertical profiles within non-convective clouds .....	77
Figure 40. Phase change heating terms within convective clouds vertical profile .....	78
Figure 41. Phase change heating terms within non-convective clouds vertical profile.....	79
Figure 42. Apparent momentum source within non-convective clouds vertical profile.....	80
Figure 43. Apparent momentum source within convective clouds vertical profile .....	81
Figure 44. Pressure gradient within convective and non-convective clouds vertical profile .....	82
Figure 45. Subsidence within convective and non-convective clouds vertical profile .....	83
Figure 46. Detrainment within convective and non-convective clouds vertical profile .....	84

## **ACKNOWLEDGMENTS**

I would like to thank my major professor, Dr. Xiaoqing Wu, and my committee members Dr. William Gallus and Dr. Andy VanLoocke for their guidance throughout the course of this research. I would also like to thank the department and my friends for making my time at Iowa State University a wonderful experience.

In addition, I would also like to acknowledge my parents, Doug and Chris Covert, and my brother Jared Covert as I would not have made it this far without all their love and support.

## ABSTRACT

Two-dimensional (2D) and three-dimensional (3D) cloud resolving models (CRM) are some of the best tools that can be used to simulate convective cloud systems and their properties relative to larger scale models. But, when attempting to understand when a certain type of CRM should be used, previous studies on the effects of dimensionality within CRMs have returned conflicting results. Equivalent 2D and 3D CRMs were used to produce 30-day simulations of the Madden-Julian Oscillation (MJO) during the first month of the Dynamics of the Madden-Julian Oscillation (DYNAMO) field campaign (October 2011) to study the effects of dimensionality to increase understanding of convective cloud processes and the processes behind the MJO. The MJO is a 30 – 90 day oscillation that occurs in multiple rainy and dry phases within the Eastern Indian and Western Pacific Ocean, but the mechanisms as to why it occurs is relatively unknown. By using CRMs to simulate cloud systems during the MJO, results can provide insight into one of the main theories of the MJO, the building block theory, which is based on cloud formation and organization. The simulations are broken down into suppressed (dry) and active (rainy) MJO phases; precipitating clouds are further separated based on convective precipitation and non-convective precipitation gain further understanding of the difference in weak and strong convection.

Differences between the two- and three- dimensional models during the suppressed MJO phase are shown to be small mainly due to a lack of strong forcing or convection. The 3D model is slightly drier during this time, but it does produce more precipitation than the 2D model. Differences are shown to be larger during the active phase of the MJO, especially in the cloud

mass flux and momentum fluxes in which values are larger in the 3D model. Cloud properties within non-convective precipitation are found to have small differences between the 2D and 3D CRMs, but cloud properties during convective precipitation are shown to be much larger. The 3D model simulates stronger vertical motion, larger cloud mass fluxes, and larger momentum fluxes within this type of precipitation.

The results show that 3D simulations result in more cloud and stronger vertical motion. Results also suggest that momentum, vertical motion, and pressure are sensitive to dimensionality. Understanding how sensitive these processes are to dimensionality is important for the use of CRMs for MJO simulations and within global models climate models. Vertical wind shear plays an important role within these cloud processes, and future studies should focus on the impact of the wind shear to better understand the differences in momentum and cloud formation in 2D and 3D models.

## CHAPTER 1

### INTRODUCTION

Cloud systems play a major role in global climate and weather prediction, but their representation within climate models is fairly limited (Grabowski et al. 1996, Arakawa 2004). While climate models are very detailed and resolve large scale features, the size of individual convective cloud and convective cloud systems are much smaller and cannot be explicitly resolved leading to these models having a hard time simulating clouds accurately. Convective cloud systems have a key role in weather and climate by influencing energy balances within the atmosphere, water and hydrologic cycles, and other large scale radiative and dynamical processes (Arakawa 2004, Fan et al. 2017, Labbouz et al. 2018).

Large varieties of convective clouds exist within the atmosphere, and they embody all atmospheric processes that occur and lead to changes in large scale circulations and climate (Bony et al. 2015). Not only do clouds impact water within the atmosphere, but rainclouds and precipitation have direct effects on other areas of Earth's water cycle (Chahine 1992). Major sources of error can also occur in predicting precipitation due to uncertainties in complicated convective cloud processes, including moisture transport and how cloud systems directly interact and modify their environment (Browning 1990). Convective cloud systems interact with the surface as well, leading to effects on the atmospheric boundary layer. Cloud processes cause boundary layer turbulence, interact with eddy fluxes, and impact surface heat fluxes such as latent and sensible heat processes (Browning 1990, Moncrieff et al. 1997).

In addition to the surface, convective cloud systems have strong impacts on other heat and radiative fluxes within the atmosphere. Radiative processes such as the reflection, absorption, and scattering of longwave and shortwave energy and changes in overall cloud cover lead to large changes in radiative heat transfer and the overall energy balance of the atmosphere (Stephens 2005). This variability highlights just how important clouds are to overall climate and climate change. Since 1995, the IPCC has even identified cloud systems and their properties to being a major factor in understanding climate change (Moncrieff et al. 1997), and past studies have shown that representing cloud processes in global models have been shown to cause a large degree of uncertainty in future predictions (Randall et al. 2003, Schneider 2019).

The scale of most climate models range from the tens to hundreds of kilometers, while individual clouds occur on scales of a few kilometers or even smaller (Krishnamurti et al. 1998, Randall et al. 2003, Labbouz et al. 2018). As a result, this requires cloud systems and their properties to be parameterized within large-scale models. Many types of cloud parameterizations have been developed and used within prior research. Early cloud parameterization schemes involving basic cloud mass fluxes, heat transfer, and moisture transport (i.e., Kuo 1965, Manabe et al. 1965, Arakawa and Schubert 1974) have become widely accepted and incorporated within most climate models. Newer cloud parameterization schemes have been developed to help improve simulations by focusing on more specific cloud properties such as cloud feedback mechanisms, momentum dynamics, hydrometeor transport, and other prognostic variables (Tiedtke 1989, Emanuel 1991, Donner 1993, Webb 2015). Some even focus on parameterizing cloud ice microphysics, which occur at scales even smaller than 1 kilometer. These types of parameterization schemes (i.e., Koenig 1972, Ferrier 1994, Morrison and Milbrandt 2015) help

to simplify the processes that intertwine most larger scale cloud processes, leading to more accurate climate model simulations.

Although widely used, many parameterization schemes do not fully represent all of the effects that cloud systems have on the atmosphere and can lead to limitations within simulations. These limitations arise from a lack of understanding of cloud microphysical processes and variables that are not being explicitly calculated (Cess et al 1990, Sullivan et al. 2016, Zhang et al. 2016). To avoid this issue newer ways of representing cloud systems within climate models have been developed, such as by super-parameterization or even a convection permitting model.

Super-parameterization is the process in which a small cloud model is used within a global climate model in place of typical parameterization schemes. A two-dimensional cloud resolving model (CRM) is used at each vertical column of the climate model to simulate cloud systems and their properties (Khairoutdinov and Randall 2001, Arakawa 2004, Liu et al. 2012). A CRM is a type of model that has a fine enough resolution to be able to calculate and resolve the processes that occur within individual clouds. Typically, each column only interacts with one another through the larger scale dynamics of the global climate model and the global model drives the CRM through its simulated large scale processes. This type of representation of clouds within climate models allows for more accurate simulations by improving the interaction of cloud and climate scale processes (Grabowski 2001).

With more uses than just super-parameterization, the high resolution (typically on the scale of a few kilometers or even smaller) of a CRM gives it the ability to simulate a wide variety of cloud systems and cloud properties. This provides a more detailed understanding of how cloud ice and water processes affect the overall cloud system (Zeng et al. 2007). Prescribed large scale forcing, CRMs can accurately simulate many different types of cloud systems and

their radiative and dynamical properties (Grabowski et al. 1996, Wu et al. 1998, Wu et al. 1999, Guichard and Couvreux 2017).

While original CRMs were developed as a two-dimensional model (2D), advances in computer power have allowed the creation and use of three-dimensional (3D) CRMs. 2D and 3D CRMs are very similar in nature, but 2D variants are more frequently used due to the cost of computer resources and time for a 3D model (Xu and Randall 1996, Zeng et al. 2007). Early studies completed by Wilhelmson (1974) comparing the two types of models showed that clouds within the 3D model tended to develop and grow faster and become much deeper (1974). Pressure perturbations and effects of the vertical pressure gradient force within mid-level updrafts has also been identified to be sensitive to dimensionality, ie. the addition of more dimensions within a model (Schlesinger 1984, Morrison 2016). Others have also shown that 2D models tend to be drier to their 3D counterparts (Phillips and Donner 2006, Tompkins 2000)

Though many studies agree that updrafts and vertical motion is stronger within 3D CRMs (Wilhelmson 1974, Schlesinger 1984, Redelsperger et al. 2000, Phillips and Donner 2006, Zeng 2008, Morrison 2016), others have demonstrated conflicting results. Some studies suggest that cloud thermodynamical properties and surface fluxes are similar between 2D and 3D models (Tao et al. 1987, Grabowski et al. 1998), but Donner et al. (1999) found larger differences in ice and moisture content in the upper troposphere which lead to stronger interactions between radiative and cloud dynamical processes. While Wilhelmson (1974) and Redelsperger et al. (2000) agree that thunderstorm organization between 2D and 3D models are comparable, Skamarock et al. (1994) showed that 2D models under predicted the strength of most mesoscale-convective systems. Although many of these studies seem to indicate contradictory results on the effects of dimensionality on CRMs, some propose that this may be due in part to the

sensitivity of the cloud ice microphysics used within the model (Redelsperger et al. 2000, Phillips and Donner 2006, Zeng 2007, Zeng 2008).

Without direct observations, understanding the interaction of cloud scale processes within the atmosphere can be difficult. Thus, CRMs can be especially useful over oceans or areas without in-situ measurements to provide insight into many cloud properties. Atmospheric simulations from field projects such as the Atlantic Tropical Experiment (GATE) in 1974 and the Tropical Ocean-Global Atmosphere Coupled Ocean-Atmosphere Response Experiment (TOGA COARE) in the early 1990's showed that not only could a CRM accurately depict the general climate of the region, but it was able to provide insight as to how small scale cloud dynamics contribute to other atmospheric processes (Tao et al. 2004). It also helped identify and model certain regional disturbances and circulations such as the intraseasonal Madden-Julian Oscillation (MJO).

The MJO is a tropical disturbance first discovered by Madden and Julian (1971,1972) that occurs that initiates in the Indian Ocean and propagates slowly eastward at around  $5 \text{ ms}^{-1}$  with a cycle of about 30-90 days. It has multiple phases, including an active phase, in which deep convection occurs while strong westerly winds occur west of precipitation and easterlies occur to the east with the winds reversing in the upper atmosphere (Zhang 2005). The MJO plays a notable role in the weather and climate of the region as it impacts other ocean oscillations, the El-Nino – Southern Oscillation (ENSO), and various tropical activity (Tang and Yu 2008, Klotzbach 2014).

While the MJO has been studied for decades, there is still uncertainty as to its formation and evolution over time. There are many theories that suggest that the MJO may be caused by Kelvin waves or linked to the latent heat release of convection connected to Kelvin waves

(Roundy 2008). Blade and Hartmann (1993) suggested a “recharge-discharge” theory that was first proposed by Hendon and Liebmann in 1990 that is based on warming and moistening of the ocean and surface to develop instability (“recharge”) followed by a dry period that stabilizes the atmosphere following the period of convection (“discharge”). Other theories are based upon a cloud “building block” theory that was first proposed by Mapes et al (2006) that describes how the growth and evolution of mesoscale convection plays a role in the formation of tropical waves. Different types of cloud systems within a wave occur at different frequencies during different phases, building upon one another and leading to the growth and evolution of the MJO over time.

In an attempt to better understand the dynamics and evolution of cloud systems during MJO phases, the Dynamics of the Madden-Julian Oscillation (DYNAMO) field campaign was conducted during October 1<sup>st</sup> - December 29<sup>th</sup>, 2011 in the Indian Ocean. The main goals of the field campaign were to identify how the troposphere gains moisture during the first stage of MJO, determine the role of cloud types and frequencies in the initiation of the MJO, and to find the role of air – sea interactions in the beginning and evolution of the MJO (Johnson and Ciesielski 2013). Two predominant MJO events occurred during this time, with a third that was less pronounced (Xu and Rutledge 2014). The initiation of the MJO is very apparent in these three events, and they all show periods of heavy precipitation for a period of 1 to 2 weeks that are followed by suppressed convection and calm conditions.

While DYNAMO helped increase knowledge about the formation and progression of the MJO, there are still important details to discover. Most research has focused on attempting to use better parameterization techniques or higher resolution GCMs to improve simulations of the MJO. But, even with new high resolution models or parameterization schemes, models will only

be as good as the assumptions made within the model. To be able to confidently increase the accuracy of GCM simulations of the MJO, it is imperative to be able to fully understand convective cloud processes and the role that they have within large scale atmospheric processes. While the recharge-discharge theory of the MJO focuses on sea surface temperatures, the building block theory takes into account different types of cloud systems and their organization within the atmosphere. The focus of this paper is to simulate cloud systems during the MJO using identical 2D and 3D CRMs to identify differences between the two models to increase understanding of convective cloud processes and cloud organization, thus providing more evidence behind the building block theory. The use of CRMs will allow for analysis into small scale cloud properties that cannot be easily observed or calculated with GCMs, providing new insight into the MJO. Based on prior research, it is hypothesized that the 3D simulation will result in larger vertical motion, thus leading to stronger cloud mass fluxes.

Chapter 2 describes the cloud resolving model, large scale forcing, observational data, and experimental design. Chapter 3 investigates basic atmospheric properties and radiative properties that are simulated by the models while chapter 4 analyzes cloud properties and dynamics. Chapter 5 analyzes cloud thermodynamic properties and chapter 6 compares various cloud properties separated by the occurrence of convective and non-convective precipitation. A summary and discussion are given in chapter 7.

## CHAPTER 2

### **CLOUD RESOLVING MODELS AND EXPERIMENTAL DESIGN**

#### **2.1 Models**

The numerical models used in this study are the Iowa State University CRMs, which are based on the Clark-Hall CRM (1996) and are extensively detailed by Grabowski et al. (1996). They have identical setup with the only difference being that one model is 2 dimensional and the other is 3 dimensional. Both models are non-hydrostatic and use a finite-difference formulation. The models are forced by observed large-scale observations, with a relaxation term included for the horizontal wind field. They have a 3 km horizontal resolution with x in the east to west component. The dimensions of the models are 200 km horizontally and 30 km vertically. The vertical component has 34 levels with a stretched grid, starting at 100 m at the surface and increasing to 1500 m at the top of the domain. A time step of 10 seconds is used. Both simulations ran for 30 days from October 1, 2011 – October 30, 2011. The Coriolis term is set to zero within these simulations and the models use basic periodic boundary conditions. Rigid bottom, free-slip and top boundary conditions are coupled with a gravity wave absorber within the upper 14 km of the domain. Radiation calculations are completed every 150 seconds using an effective radii of 10  $\mu\text{m}$  for water droplets and 30  $\mu\text{m}$  for ice particles. Radiative properties are parameterized using the National Center for Atmospheric Research (NCAR) Community Climate Model 3 (CCM3) as described by Kiehl et al. (1996). Surface fluxes within both models are controlled by observations. Cloud liquid water processes are represented by the Kessler (1969) bulk warm rain parameterization scheme while ice processes are represented by the

Koenig and Murray bulk parameterization scheme (1976). In this model, the ice parameterization scheme uses two types of ice that takes density into account; Type A is lower density slow falling ice, such as fine ice crystals, while Type B is high density faster falling ice, such as graupel and hail. Only the Type A ice is used in radiation calculations. While both schemes are older, previous studies (Grabowski et al. 1996, Wu et al. 1998, Wu et al. 1999, Wu et al. 2007) have demonstrated that using these microphysics schemes create simulations that are comparable to observations.

## 2.2 Large Scale Forcing

The large scale forcing data used in this study is provided by Richard Johnson and Paul Ciesielski from the DYNAMO field campaign taken in 2011. This data includes array averaged values for wind, moisture, temperature, vorticity, and divergence. Advection tendencies for variables such as heat source and sink, surface heat fluxes, and temperature and moisture are included as well. This data comes from the Northern Sounding Array of the experiment (Figure 1) which is set between four boundary points. These points are located at the sites of Malé ( $4.19^{\circ}$  N and  $73.53^{\circ}$  E), Colombo ( $6.91^{\circ}$  N and  $79.87^{\circ}$  E), Gan ( $0.69^{\circ}$  S and  $73.15^{\circ}$  E), and Revele ( $0.00^{\circ}$  N and  $80.50^{\circ}$  E). The data set has a temporal resolution of 6 hours was created using interpolation of upper-air dropsonde data onto a grid (Johnson and Ciesielski 2013). The grid has a horizontal and vertical resolution of 1 degree and 25 hPa, respectively. Figure 2 shows the domain averaged temperature and moisture large scale forcing used in this study. The period starts off with generally weak warming and dryness, but much stronger moistening and cooling starts to occur on October 15<sup>th</sup> with the beginning of the MJO.

### 2.3 Wind and Surface Fluxes

Figures 3 and 4 represent the zonal and meridional wind speed over the Northern Sounding Array. The modeled wind is domain averaged and is relaxed to the observed wind. Compared to the large scale forcing, wind shear tends to be stronger during the second half of the month when it is moistening and cooler. Overall, weak westerlies transition into strong easterlies as the MJO begins halfway through the period. Compared to one another, differences between the 2D and 3D model are very small due during the entire simulation period.

Figure 5 illustrates a surface flux time series of observed sea surface temperature (SST), sensible heat, and latent heat averaged over the domain for the period. While varying slightly, SSTs remain relatively constant around 29°C throughout the period. Sensible heat flux values start out lower and gradually increase as the MJO begins and peak at the end of the month. Latent heat fluxes change somewhat over the period but generally fluctuate around 100 W/m<sup>2</sup>.

### 2.4 Observational Data

Observational data is used for many variables in this study, including precipitation, radiation, heat source and moisture sink, liquid and ice water content, liquid and ice water path, and cloud fraction. Observed radiation data, cloud data, ice and liquid water path and content are taken from the CERES SYN1deg product at Gan Island, Maldives. This data has a spatial resolution of 1° by 1° that is then domain averaged and a temporal resolution that is daily. Although the CERES data has a much larger spatial resolution compared to the resolution of the CRMs used in this study, results are expected to be similar as both the observations and model simulations are domain averaged to the same temporal resolution as opposed to being compared

on a per grid cell basis. Radiation data used in this study includes top of the atmosphere (TOA) shortwave (SW) radiation upward and downward, TOA longwave (LW) radiation upward, surface SW radiation upward and downward, and surface LW radiation upward and downward. The liquid water path is calculated using the liquid condensate and the ice water path is calculated using both large and small ice particles, such as ice crystals and hail/graupe. Liquid and ice water path is a measure of the total amount of liquid or ice in a column in the atmosphere. Two types of precipitation observations are used, with one being domain averaged  $Q_2$  budget derived precipitation and the other being calculated through the high resolution rain-rate retrieval and estimate from the Tropical Rainfall Measuring Mission (TRMM) 3B42v7 product with a spatial resolution of  $0.25^\circ$  by  $0.25^\circ$  that is up-scaled to  $1^\circ$  by  $1^\circ$  to match other observations. Heat source is computed using (1) while moisture sink is computed using (2):

$$Q_{1o} = \left(\frac{p}{p_0}\right)^\kappa \left[ \frac{\partial \theta}{\partial t} + U \frac{\partial \theta}{\partial x} + V \frac{\partial \theta}{\partial y} + W \frac{\partial \theta}{\partial z} \right] \quad (1)$$

$$Q_{2o} = -\frac{L_v}{c_p} \left[ \frac{\partial Q_v}{\partial t} + U \frac{\partial Q_v}{\partial x} + V \frac{\partial Q_v}{\partial y} + W \frac{\partial Q_v}{\partial z} \right] \quad (2)$$

where  $U$ ,  $V$ ,  $W$ ,  $Q_v$ , and  $\theta$  are large-scale observed wind, moisture, and potential temperature, the specific heat of dry air at constant pressure ( $c_p$ ) is  $1004 \text{ J K}^{-1} \text{ kg}^{-1}$ ,  $p$  is the pressure while  $p_0$  is  $1000 \text{ hPa}$ , the latent heat of condensation ( $L_v$ ) is  $2.5 \times 10^6 \text{ J kg}^{-1}$ , and  $\kappa = R_d/c_p$  in which  $R_d$  is the dry gas constant. Sea surface temperature observations were obtained from both the NOAA/ERSL website as well as the Woods Hole Oceanographic Institution.

## 2.5 Methods

The results in this study will be discussed by a separation into two time periods, which are a suppressed MJO period (October 1<sup>st</sup> – October 15<sup>th</sup>) and an active MJO period (October 16<sup>th</sup> – October 30). Overall trends are identified through a comparison of variables to observations as well as a comparison of the 2D simulation to the 3D simulation for a deeper understanding of the convective cloud processes during these two periods. Variables are split into the categories of basic atmospheric properties, cloud properties, and cloud thermodynamics. A will represent figures for the 2D model and B will represent figures for the 3D model.

## CHAPTER 3

### BASIC ATMOSPHERIC PROPERTIES

#### 3.1 Temperature

Figure 6 shows the bias of model simulated temperature compared to observations. The model output is time averaged to every 6 hours to match available observations. Overall, both 2D and 3D models tend to be cooler than the observations with the 3D model being the coolest, especially during the middle of the period. The 2D model has a warm bias of 0 to 2 degrees within the upper troposphere during the end of the suppressed MJO phase and beginning of the active MJO phase that does not occur within the 3D model. But, this does not lead to any major differences between the two models during the overall period as the mean temperature bias for the 2D model is  $-1.220 \pm 0.842^\circ\text{C}$  and  $-2.471 \pm 0.843^\circ\text{C}$  for the 3D model.

#### 3.2 Moisture

The bias of model simulated moisture compared to observations is shown in Figure 7. Like temperature, the model simulated moisture is averaged to 6-hour time periods. Both the 2D and 3D model are similar to observations, with only a small dry bias within the lowest 4 km of the atmosphere. This dry bias is more prevalent during the suppressed MJO phase than the active MJO phase. Compared to one another, the both models average nearly the same amount of moisture during the entire period, as the 2D model averaged  $-0.658 \pm 0.001$  and  $-0.785 \pm 0.001$ .

### 3.3 Precipitation

Model simulated precipitation compared to observed rainfall as well as Q2 budget derived precipitation is represented by Figure 8. During the suppressed period of the MJO, simulated and observed rainfall was minimal. A period of enhanced precipitation followed as the active phase of the MJO started. Both the 2D and 3D models compared well to TRMM observations, but TRMM observations had higher peaks in precipitation during stronger events. The modeled precipitation tended to follow the trend of the budget-derived precipitation much more closely than TRMM observations, except for during the suppressed MJO period when the budget-derived precipitation had occasional spikes in rainfall. The 3D model and 2D model produced similar amounts of precipitation overall during the entire period with a mean precipitation of  $0.322 \pm 0.398$  for the 2D model and  $0.305 \pm 0.350$  for the 3D model.

### 3.4 Radiative Fluxes and Radiative Heating Tendencies

This study focuses on the comparison of radiation from the top of the atmosphere, including the incoming solar flux, outgoing longwave flux, and the reflected shortwave flux between the 2D model, 3D model, and observations (Figure 9). Radiative fluxes at the surface include the incoming longwave flux, incoming shortwave flux, outgoing longwave flux, and outgoing shortwave flux (Figure 10). Modeled radiative fluxes compare well with CERES, with most fluxes following the same trend as observations. Surface incoming longwave radiation is the only flux in which both models deviate from observations, with a decreasing trend toward the end of the suppressed MJO period before increasing to near observed values while the observed flux remains constant and then slowly increases. 2D and 3D simulated radiative fluxes compare well, with similar means for both models (Table 1). The largest difference between the two

models are in the longwave up at the top of the atmosphere and shortwave down at the surface, with a difference in means of about  $7 \text{ W/m}^2$ .

Figure 11 represents the mean vertical profile of shortwave and longwave radiative heating tendencies. The shortwave heating tendency is very similar between the 2D and 3D model within this study. Both models follow the same trend and value. Below 6km, the surface shortwave heating tendency is about  $0.5 \text{ K/day}$ . The shortwave heating tendency peaks at  $1 \text{ K/day}$  near 11km and then decreases to near zero in the top of the atmosphere. The longwave heating tendency is also similar between the 2D and 3D models in this study, but there are some differences. The longwave heating tendency is negative throughout the entire atmosphere. Both models show the longwave heating tendency decreasing near the surface and peaking at 1km. The longwave tendency increases slightly above 2km but decreases again near 5km and peaks near 11km. The longwave tendency within both the 2D and 3D model then increases to near zero in the top of the atmosphere. Near the surface, between 4km to 8km and 9km to 12km, the 2D model loses more heating due to the longwave tendency. When added together, the total radiative heating tendency is very similar to the longwave heating tendency in both models, but it is slightly smaller. Cooling is predominant throughout much of the atmosphere and it peaks near 1km and 11km similarly to the longwave heating tendency.

## CHAPTER 4

### CLOUD PROPERTIES AND DYNAMICS

#### 4.1 Cloud Mass Fluxes

Cloud mass flux describes the vertical transport of cloud mass within the atmosphere. Updraft mass flux is a positive, upward cloud mass flux while downdraft mass flux is a negative, downward cloud mass flux. Figure 11 shows a time series of model simulated updraft cloud mass flux while Figure 12 represents model simulated downdraft cloud mass flux. During the suppressed period of the MJO, both downdraft and updraft mass flux are very small or non-existent. When convection and clouds occur during the active MJO period, vertical motion and cloud mass flux increases. The mass fluxes are typically about the same value, except during strong convection when the updraft mass flux can be 1 to 2 times the strength of the downdraft mass flux. The largest values of cloud mass flux occur within the lowest 4 to 5 km of the atmosphere. Overall, updraft mass fluxes are larger in the 3D model with a mean of  $3.678 \pm 4.167$  mb/hr compared to the 2D mean of  $2.461 \pm 4.023$  mb/hr. Downdraft mass fluxes are similar during the overall period between the 2D model and 3D model with a mean flux of  $-0.908 \pm 1.934$  mb/hr for the 2D model and mean flux of  $-0.921 \pm 1.816$  mb/hr for the 3D model.

#### 4.2 Cloud Fraction

Cloud fraction represents the portion of the domain that is covered in clouds. Figure 13 depicts the time series of cloud fraction domain averaged over the Northern Sounding Array, while Figure 14 is averaged in both space and time to give a cloud fraction vertical profile. The cloud fraction is lowest in both models during the suppressed MJO period, with values between 0

and 0.2 and most clouds occurring near 10km. Once convection begins during the active MJO phase, the cloud fraction significantly increases. The highest values of cloud fraction occur in the middle of the layer between 6km and 10km, with some areas having a cloud fraction of 0.8 or higher in deep convection. Over the entire period, the 3D model has a larger mean cloud fraction of  $12.095 \pm 0.094\%$  while the 2D model has a mean cloud fraction of  $7.518 \pm 0.088\%$ .

#### 4.3 Cloud Top Frequency

To help better understand the overall cloud structure, cloud top frequency was calculated by both models based on the cloud top height and cloud top temperature (Figure 15). During the suppressed period of the MJO, cloud top heights were generally within the lowest 2km to 3km of the atmosphere. During this time, both models also indicate cloud top temperatures between  $10^{\circ}\text{C}$  and  $30^{\circ}\text{C}$ . Convective clouds grew and became deeper during the active phase of the MJO, with a higher frequency of cloud top heights between 8km and 12km. Cloud top temperatures were also much colder as models indicated a higher frequency of clouds having temperatures between  $-20^{\circ}\text{C}$  and  $-50^{\circ}\text{C}$ , with some cloud tops having temperatures even colder. While the 2D model and 3D model both had a similar range of cloud top heights and temperatures, the frequency of which they occurred is much more centered for the 3D model than the 2D model. Overall, the 3D model had higher cloud tops with an average of  $5.427 \pm 9.092$  km compared to the 2D model with an average of  $3.054 \pm 7.087$  km.

#### 4.4 Liquid/Ice Water Path

Figure 16 shows the domain-averaged cloud ice and liquid water path for both models compared to CERES observations. Model simulated ice and liquid water path is generally larger than observed values, except for the last 2 to 3 days of the active MJO period. During the

suppressed MJO period, liquid water path is larger than the ice water path. Ice water path is almost zero during this period mainly due to the presence of mostly shallow, warmer clouds as shown through cloud top temperatures. Both ice and liquid water path greatly increase during the active MJO period, with the highest peaks of water path occurring during the strongest convection. The ice water path is larger than liquid water path during the active MJO period as convection is much deeper and allows for more ice within the clouds. Compared to one another over the entire period, the 2D model has a larger mean liquid water path of  $0.409 \pm 0.001 \text{ kg/m}^2$  while the 3D model has a mean liquid water path of  $0.218 \pm 0.001 \text{ kg/m}^2$ . But, the 3D model has a larger mean ice water path of  $0.154 \pm 0.017 \text{ kg/m}^2$  compared to the 2D model of  $0.080 \pm 0.012 \text{ kg/m}^2$ .

#### 4.5 Cloud Water and Ice Content

Breaking down the cloud microphysics further, Figure 17 shows a vertical profile of model simulated total cloud water content. The largest values of cloud water content occur between 4 km and 6km within the atmosphere. A second, smaller spike occurs around 1km where the total water content is increasing and then decreases sharply around 2km. The 2D and 3D model follow a very similar trend with only small differences. The 2D model has more cloud water in the lowest 6km while the 3D model has slightly more cloud water above 6km. To better understand this difference, the total cloud water content was also broken down into its microphysical components (Figure 18). The total cloud water content is made up of the condensate ( $Q_c$ ), rainwater ( $Q_r$ ), type-A ice ( $Q_a$ ), and type-B ice ( $Q_b$ ). Type-A ice represents small ice crystals that form through nucleation while type-B ice represents larger ice particles that form through collision and coalescence processes, such as hail or graupel. Type-A ice is the most predominant type of ice or water content within both models and peaks in the middle of the

atmosphere around 6km to 7km. Type-B ice is relatively small, with values of  $0.01\text{g/m}^3$  or less throughout the profile. It peaks a bit lower than type-A ice in both models around 5km. Condensate varies throughout the profile, with small peaks near the surface, 4km, and 10km. Rainwater is highest in the lowest 3km of the atmosphere with values approaching  $0.02\text{g/m}^3$ , but it decreases quickly to near zero above 4km in both the 2D and 3D model. While  $Q_r$  and  $Q_a$  are similar between the 2D and 3D model,  $Q_c$  tends to be larger in the 2D model while  $Q_b$  is almost doubled in the 3D model. Over the entire period, both the 2D and 3D model average the same amount of total cloud water with the 2D model averaging  $0.007 \pm 0.001 \text{ g/m}^3$  and the 3D model averaging  $0.006 \pm 0.001 \text{ g/m}^3$ .

#### 4.6 Momentum Transport

Momentum transport within simulated cloud systems was computed using (3):

$$F_u = \frac{\rho}{N} \sum_i w_i (V_i - \bar{V}) \quad (3)$$

This equation originates from analysis completed by Zhang and Wu (2003). Overall, the momentum flux within cloud systems is negative in easterlies and positive in westerlies. During the suppressed MJO phase, most momentum transport is negative and occurs in the lowest 5km to 6km of the atmosphere within both models (Figure 19). During the active MJO phase, the momentum transport greatly increases. While the momentum flux is still negative in the lowest 5km of the atmosphere, strong positive momentum transport occurs above this in both the 2D and 3D model. Peaks in the momentum flux during this time coincide with the strongest convection. The highest momentum transport occurs generally between 6km to 10km within the atmosphere.

Figure 20 depicts the mean vertical profile of the momentum flux in the u-component.

Near the surface, the momentum flux is negative in both models. While in the 3D model the momentum flux becomes positive near 2km, momentum flux does not become positive in the 2D model until above 3km. Both the 2D model and 3D model follow the same trend in the middle of the atmosphere, but the 3D model is consistently stronger below 12km. Momentum flux peaks in both models near 4km. In the top of the troposphere, the 2D model becomes slightly larger than the 3D model. During the entire period, the 3D model has much larger momentum flux values with an average of  $0.124 \pm 0.497 \times 10^{-2}$  kg/m/s<sup>2</sup> compared to the 2D model average of  $-0.032 \pm 0.577 \times 10^{-2}$  kg/m/s<sup>2</sup>.

#### 4.7 Apparent Momentum Source

Figure 21 depicts the time series of the divergence of the momentum flux, or apparent momentum source. During the suppressed MJO period, the momentum source is small and exists mostly below 3km. When the active MJO period begins, the momentum source increases in both models. It is generally negative in the lowest 4km and between 8km to 10km while it is positive in the middle troposphere and near the top of the atmosphere during this period. Most differences between the 2D and 3D model during this time occur within the strongest convection.

Figure 22 depicts the vertical profile of the momentum source. When time averaged, differences between the 2D and 3D model become much smaller. In both models, the momentum source is positive near the surface and above 5km but negative between near 1km and 5km. The 2D model is larger below 2km while the 3D model is larger between 2km to 4km and above 10km. When averaged over time, the 3D model has a mean of almost double the 2D model of  $0.078 \pm 0.576$  m/s/day compared to the 2D model mean of  $0.043 \pm 0.497$  m/s/day, respectively.

#### 4.8 Energy Conversion

In understanding the momentum budget, the momentum transport can be related to the mean flow energy, eddy kinetic, and potential energy conversion. The equations for mean flow energy conversion to eddy kinetic (5) and potential energy to eddy kinetic energy (6) originate from Asai (1970) and are calculated as follows:

$$\langle \bar{K}, K' \rangle = -\overline{u'w'} \frac{\partial \bar{u}}{\partial z} \quad (4)$$

$$\langle P, K' \rangle = g \frac{\overline{T'w'}}{\bar{T}} \quad (5)$$

Figure 24 represents the mean vertical conversion from mean flow energy to eddy kinetic energy. Eddy kinetic energy is created when momentum transport is downgradient, which occurs when the vertical wind shear is negative and the conversion is positive. When the vertical wind shear is positive, eddy kinetic energy is converted to mean flow energy. The 2D model and 3D model follow the same trend throughout except for the lowest 3km of the atmosphere. Besides near the surface where both models show downgradient transport, the energy conversion in the 2D model below 3km is negative, indicating upgradient transport, while the 3D model has very small conversion values. Between 3km to 13km, both models have positive conversion values with larger conversion values in the 3D model, representative of downgradient transport. Above 14km, conversion values become negative in both the 2D and 3D model.

Figure 25 shows the timeseries of the conversion of energy from mean flow to eddy kinetic. During the suppressed MJO period, there is little energy conversion within both the 2D and 3D model. The 2D model does simulate some energy conversion from eddy kinetic to mean

flow below 3km, but it is small. When the active MJO period begins, energy conversions begin to increase in both models. Within the 3D model, most energy conversion is positive, indicating downgradient transport between 2km to 6km and 8km to 12km. Weak upgradient transport is also noticeable in the upper part of the atmosphere in the 3D simulation. In the 2D simulation, energy conversion is positive in the lowest 4km and between 8km to 12km. But, unlike in the 3D model, upgradient transport occurs more often in the mid to upper levels. Large energy conversion from eddy kinetic to mean flow in the lowest 6km of the atmosphere during the last period of strong convection also indicates upgradient transport. The largest energy conversion to eddy kinetic occurs during the end of the period for the 3D model during a period of strong convection.

Figure 26 represents the conversion from potential to eddy kinetic energy. Near the surface and above 13km to 14km of the atmosphere, eddy kinetic energy is converted to potential energy within both models. But, throughout most of the atmosphere between 1km to 13km there is a large conversion of potential energy to eddy kinetic energy. While the 2D and 3D models follow the same trend overall, the 2D model has slightly larger conversion values near 3km to 4km, but the 3D model has more conversion from potential energy to eddy kinetic energy near the surface and above 4km. The 2D model has two peaks near 3km and 9km whereas the 3D model has one major peak near 9km.

Figure 27 shows a timeseries of potential to eddy kinetic energy. Similar to the mean flow to eddy kinetic conversion, little potential energy is converted to eddy kinetic during the suppressed MJO period. During the active MJO period, potential energy is converted to eddy kinetic throughout much of the atmosphere within both models. Above 12km, there is some small eddy kinetic converted back to potential in the 2D and 3D simulations. When compared to

one another, the 3D model has higher values of energy converted to eddy kinetic during the active MJO period between the surface and 12km. But, in the center of deep cloud systems during strong convective periods, the 2D model simulates higher values of potential energy converted to eddy kinetic.

## CHAPTER 5

### CLOUD THERMODYNAMICS

#### 5.1 Heat Source and Moisture Sink

The interaction of heat and moisture is one of the most important thermodynamic processes of convective cloud systems. To better understand the heat and moisture budgets of clouds, apparent heat source ( $Q_1$ ) and apparent moisture sink ( $Q_2$ ) are used. Introduced by Yanai et. al (1973), they are derived from temperature and moisture conservation equations and thus can be calculated from observations or in the case of CRMs, directly modeled. Equations for  $Q_1$  and  $Q_2$  used within this CRM originate from Grabowski et al. (1996) and are as follows:

$$Q_1 = Q_{1e} + Q_{1c} + Q_{1r} + Q_{1d} \quad (6)$$

$$Q_2 = Q_{2e} + Q_{2c} + Q_{2d} \quad (7)$$

and

$$Q_{1e} = -\frac{\pi}{\rho_0} \frac{\partial \rho_0 \langle w' \theta' \rangle}{\partial z} \quad (8)$$

$$Q_{1c} = \frac{L_v}{c_p} \langle c - e \rangle + \frac{L_f}{c_p} \langle f - m \rangle + \frac{L_s}{c_p} \langle d - s \rangle \quad (9)$$

$$Q_{1d} = \pi \langle D_\theta \rangle \quad (10)$$

$$Q_{1r} = \langle Q_r \rangle \quad (11)$$

$$Q_{2e} = \frac{L_v}{c_p} \frac{1}{\rho_0} \frac{\partial \rho_0 \langle w' q'_v \rangle}{\partial z} \quad (12)$$

$$Q_{2c} = \frac{L_v}{c_p} [\langle c - e \rangle + \langle d - s \rangle] \quad (13)$$

$$Q_{2d} = -\frac{L_v}{c_p} \langle D_{q_v} \rangle \quad (14)$$

The primed variables in these equations represent deviations from the means;  $\rho_0$  is air density;  $L_s$ ,  $L_v$ , and  $L_f$  are the latent heats of sublimation, condensation, and fusion;  $c$ ,  $e$ ,  $d$ ,  $s$ ,  $f$ , and  $m$  are the rates of condensation, evaporation, deposition, sublimation, freezing, and melting. The  $Q_1$  equation (4) is comprised of the eddy transport ( $Q_{1e}$ ), the phase change ( $Q_{1c}$ ), radiation that includes both the shortwave and longwave tendencies ( $Q_{1r}$ ), and sub-grid scale eddy diffusion which includes the divergence of parameterized vertical flux that is connected to surface sensible heat flux ( $Q_{1d}$ ). Similarly, the  $Q_2$  equation (5) is made up of the eddy transport ( $Q_{2e}$ ), phase change ( $Q_{2c}$ ), and sub-grid scale eddy diffusion ( $Q_{2d}$ ) which also includes the divergence of parameterized vertical flux, but unlike  $Q_1$  it is connected to the surface latent heat flux instead of surface sensible heat flux.

Figures 28 and 29 depict the domain-averaged time series of model simulated heat source and moisture sink as well as a comparison to  $Q_1$  and  $Q_2$  computed using observations. Figures 30 and 28 show a 30 day mean vertical profile of simulated heat source and moisture sink. Overall, trends are similar between the 2D and 3D model.  $Q_1$  is very small during the suppressed MJO phase but increases substantially during the active MJO phase.  $Q_1$  peaks during the strongest

convection and is greatest in the middle of the atmosphere between near 6km. Compared to observations, both models have smaller  $Q_1$  values during the suppressed MJO period and tend to have higher  $Q_1$  values in the lowest 5km of the atmosphere during the active MJO period. The 2D model and 3D model have similar  $Q_1$  means of  $1.393 \pm 1.536$  K/day and  $1.533 \pm 1.418$  K/day, respectively.

The 2D and 3D models also follow a similar trend for  $Q_2$ .  $Q_2$  is negative within the lowest 2km of the atmosphere, with the largest values occurring near 6km like  $Q_1$ . During the suppressed MJO period,  $Q_2$  is mainly negative below 4km and near zero above 4km.  $Q_2$  becomes positive during the active MJO period when the strongest convection and forcing occurs. Compared to observations, both models have larger  $Q_2$  values above 4km during the suppressed MJO period. Model simulated  $Q_2$  values are closer to observed values during the active MJO period, but overall the simulated  $Q_2$  is somewhat larger. Similar to  $Q_1$ , the 3D model and 2D model have comparable means during the entire period of  $1.143 \pm 1.117$  K/day and  $1.097 \pm 1.167$  K/day, respectively.

## 5.2 Energy from Phase Changes

Figure 29 shows a vertical profile of heat absorbed and released by 5 main phase change heating terms. The heating terms include the processes of condensation, evaporation, deposition, sublimation, and fusion. Condensation and evaporation play the largest role in heat transfer within the atmosphere, with condensation providing the largest release of heat while evaporation contributes to the largest removal of heat. These processes are largest towards the lowest 4km of the atmosphere and gradually decrease as height increases. Deposition also provides heating within the atmosphere, mainly between 4km and 12km, but it is not as strong as condensation. Sublimation processes remove energy in the same range of the atmosphere as deposition

processes, but they are smaller. Fusion is the weakest heating term within the convective clouds over the region, as values for these processes are mainly zero except for two slight peaks of negative and positive heating near 4km and 5km, respectively. Overall, the 2D and 3D simulations are very close to one another. The 3D model has slightly smaller values for deposition and sublimation, while the 2D model has slightly smaller values for evaporation. Fusion processes are almost the same between the two models, and condensation processes are larger for the 2D model in the lowest 6km but larger for the 3D model between 6km and 12km. Overall, mean 2D phase change values are similar to 3D phase change values (Table 2). The 3D model has slightly larger values for condensation and fusion processes during the entire period, while the 2D model has larger values for deposition processes.

## CHAPTER 6

### COMPARISON OF CONVECTIVE AND NON-CONVECTIVE CLOUDS

#### 6.1 Precipitation

To increase the understanding of convective cloud processes over the DYNAMO region, various cloud properties were divided and analyzed based on the classification of precipitation. Model simulated precipitating clouds was separated into two categories; convective or non-convective (also known as stratiform). Based upon the findings of Lang et. al (2003), precipitating clouds are defined as clouds that result in precipitation of at least 0.01 mm/hr and they are assumed to be non-convective unless the precipitation rate is greater than 10 mm/hr or the maximum vertical velocity within the cloud is greater than 1 m/s. Figure 30 depicts precipitation rate and the area of the Northern Sounding Array that is covered by precipitation. In both the 2D and 3D simulation, precipitation rate is larger during convective precipitation than non-convective precipitation. Also, within both models non-convective precipitation predominantly covers the domain as opposed to the convective precipitation. Compared to one another, the 2D model and 3D model are similar in areal precipitation coverage but they have some small differences in simulated rain rate. During non-convective precipitation the 2D model has a higher rain rate, but during convective precipitation the 3D model has larger peaks in the rain rate and overall precipitation.

## 6.2 Vertical Motion

In addition to precipitation, vertical motion within precipitating clouds was broken down into its convective and non-convective parts. Figures 31 and 32 depict the vertical profile of vertical velocity within convective and non-convective precipitation, respectively. Within convective precipitation, the mean vertical velocity is positive and peaks near 4km within the atmosphere, indicating that updrafts are dominant. In non-convective (stratiform) precipitation, the vertical velocity is negative between the surface and roughly 6km and then positive higher within the atmosphere. Peak downdrafts occur near 3km and are slightly larger than peak updrafts which occur between 9km to 10km. The 3D model has larger updrafts during convective precipitation, and it also has stronger downdrafts during non-convective precipitation. 3D updrafts are slightly smaller during non-convective precipitation between 6km and 9km, but they become stronger than the 2D simulated vertical velocity between 9km and 13km.

## 6.3 Cloud Mass Flux

Figures 33 and 34 represent the vertical profiles of mean cloud mass flux separated by occurrence within convective and non-convective precipitation. Within convective precipitating clouds, cloud mass flux is positive and peaks near 3km within the atmosphere. 3D simulated cloud flux during this type of precipitation is almost a third larger than that of the 2D model. In non-convective precipitation, the cloud mass flux is positive near the surface but then quickly becomes negative as height increases. Cloud mass flux negatively peaks near -2 mb/hr at 2km and then increases until it is positive after 5km to 6km. The 2D and 3D cloud mass fluxes are nearly identical near the surface, and then the 2D model becomes slightly larger than the 3D model between 3km to 9km. Above 9km, the 3D model is slightly larger than the 2D model until cloud mass flux nears zero in the upper troposphere.

#### 6.4 Heat Source and Moisture Sink

Figures 35 and 36 represent model simulated  $Q_1$  and  $Q_2$  during convective and non-convective precipitation, respectively. In convective precipitation,  $Q_1$  and  $Q_2$  are positive within both models.  $Q_1$  peaks at 4 K/day near 3km in the atmosphere, while  $Q_2$  is smaller but has a large spike near 1km. The 3D model is consistently larger than the 2D model within these clouds, especially near the spike in  $Q_2$  at 1km. Within non-convective precipitation, model simulated  $Q_1$  and  $Q_2$  are both negative below 4km in the atmosphere. Peak values in  $Q_1$  and  $Q_2$  during this precipitation are both near 2 K/day at 6km to 7km. Both models also indicate a sharp decrease in  $Q_2$  near 1km. The trend of both the 2D and 3D model are similar, but unlike convective precipitation, the 2D model has larger values of  $Q_1$  and  $Q_2$  during this type of precipitation.

#### 6.5 Energy from Phase Changes

The 5 phase change heating terms were also divided into their convective and non-convective parts to see how heating differs between the two types of precipitating clouds. Figures 37 and 38 represent the 5 heating terms for convective and non-convective precipitation, respectively. During convective precipitation, condensation is the primary source of heating within the atmosphere. It peaks near 3km in both models and is much stronger than the other 4 terms. During this precipitation, both models are very similar and only have slight differences in deposition. During non-convective precipitation, evaporation and condensation are the major terms. During this precipitation, 2D and 3D models differ greater than during convective precipitation. The 2D model has larger values of condensation but also smaller values of evaporation. Sublimation and fusion processes are very similar, but for deposition processes the 2D model has larger peaks than the 3D model.

## 6.6 Apparent Momentum Source

Figures 39 and 40 depict the apparent momentum source separated by convective and non-convective precipitation. Within non-convective precipitation, the momentum source in both the 2D and 3D models is weak. Both models have a peak in the momentum source near the surface and then become negative between 1km to 6km. The momentum source is near 0 m/s/day between 6km to 10km and mostly positive in the top of the atmosphere. The 3D model is stronger in the lower levels and near the top of the atmosphere, while the 2D model is stronger near the surface. Within convective precipitation, the momentum source in both models is stronger than in non-convective precipitation. Both models follow the same trend and are negative between 2km to 4km and positive near the surface and in the mid to upper troposphere. The models show a small positive peak near 1km while having a sharp decrease to a negative peak near 3km. The 3D model tends to have stronger momentum source values within convective precipitation above 3km, while the 2D model has a larger momentum source near the surface and between 7km to 10km.

## 6.7 Pressure Gradient, Subsidence, and Detrainment Terms

Figures 41, 42, and 43 represent the pressure gradient, subsidence, and detrainment terms of the apparent momentum source, respectively. The main term of the apparent momentum source is the subsidence term, which is very similar between the 2D and 3D model. In non-convective precipitation, the subsidence is positive below 5km and slightly negative between 5km to 11km. It peaks in both models near 3km. In convective precipitation, the subsidence in both models is negative throughout most of the troposphere. Like non-convective precipitation, it peaks near 3km but it is almost twice as large as the subsidence during non-convective

precipitation. The subsidence then decreases in both models as height increases with a small increase in subsidence near 12km.

The pressure gradient within non-convective precipitation is small, but differences do appear in the trend between the 2D and 3D model. Both models have a positive pressure gradient below 2km in which the 2D peaks at almost double the value of the 3D model, but between 2km to 7km the pressure gradient in the 2D model is negative while it is positive in the 3D model. Above 7km, the pressure gradient is consistently negative in the 3D model while between 7km to 12km it is positive in the 3D model. During convective precipitation, the 2D model and 3D model follow the same trend for the pressure gradient, but the 2D model has larger negative values. The pressure gradient starts near zero at the surface and decreases to a peak near 4km to 5km, but the 2D model pressure gradient is almost double the pressure gradient of the 3D model. The pressure gradient in both models then increases slowly until it returns to near zero at the top of the atmosphere.

The detrainment within non-convective precipitation is also different between the 2D and 3D models. Below 2km, detrainment within the 2D model is positive but negative in the 3D model. Between 2km and 5km, both the 2D and 3D model indicate negative values of detrainment, but it is stronger within the 2D model. Above 6km, detrainment within the 3D model is near zero, but the 2D model has a positive spike in detrainment near 10km before decreasing to near zero in the upper troposphere. Within convective precipitation, detrainment follows a similar pattern between the two models in the mid to upper troposphere, but they are quite different below 5km. Detrainment is positive overall in the 3D model but negative between 2km to 12km in the 2D model. While both models have similar low-level peaks, it occurs higher in the atmosphere near 4km in the 3D model compared to 1km in the 2D model.

## CHAPTER 7

### DISCUSSION AND CONCLUSIONS

Clouds play a vital role in climate and weather prediction. Understanding the role clouds play in numerical weather models is important in understanding many larger scale processes. CRMs are one of the best tools that can be used to simulate convective cloud systems, but differences in their representation are not fully understood. Previous studies completed comparing 2D vs 3D CRMs (Grabowski et al. 1998, Donner et al. 1999, Tompkins 2000, Phillips and Donner 2006) tended to have conflicting conclusions on effects of dimensionality besides a general agreement on stronger vertical motion within 3D models. In this study, two CRMs were used to simulate convective cloud systems and their properties over the DYNAMO region during an MJO event to compare how dimensionality affects CRM simulations and thus increase understanding of the convective cloud process during the MJO. The CRMs used in this study are identical in setup except for their dimensionality, as one is a 2D model and the other is a 3D model. While averaging the 2D and 3D model simulated variables result in similar trends and values, differences are seen when broken down into periods of strong and weak convection. During the suppressed MJO period, many differences are small due to weak large scale forcing and limited moisture. Little convection and clouds occur as precipitation and cloud fractions are small and similar in both models, but the cloud mass and momentum fluxes do vary during this period.

During the active phase of the MJO, differences between the 2D and 3D model become much larger. The 3D model simulates more clouds, as the cloud fraction is greater than the 2D

model during this period. Cloud top frequencies based on both temperature and height indicate that the 3D simulated clouds are deeper and colder during this period. This may be attributed to a larger ice content and larger ice water path in the 3D model.  $Q_1$  is larger within the 2D model, but  $Q_2$  is larger within the 3D model. Radiative fluxes also correlate well with other atmospheric variables as there is a smaller longwave flux up and more reflected shortwave radiation at the top of the atmosphere with more longwave reflected down and less shortwave down at the surface due to more cloud cover produced by the 3D model. Differences between the 2D and 3D model in the radiation budget are relatively small during this period. The largest differences during the active MJO phase are shown in the cloud mass flux and momentum flux. During times of stronger convection, the cloud mass flux within the 3D model is larger than the cloud mass flux of the 2D model and the momentum flux within the 3D model is much larger than the 2D model.

Within non-convective precipitating clouds, differences between the 2D and 3D models are small. Mean vertical velocity within both models is similar, but it is larger within the 2D model between 3km and 9km. This trend is also seen in the profile of total mass flux as the mass flux within the clouds is dependent on vertical motion and density, of which density is relatively equal in both models. Simulated  $Q_1$  and  $Q_2$  follow the same trend, but the 2D model has slightly larger values within the middle of the troposphere. In the upper and lower part of the atmosphere, 2D and 3D values of  $Q_1$  and  $Q_2$  are nearly identical. In terms of heating and cooling within the atmosphere the processes of fusion, deposition, and sublimation are alike between the 2D model and 3D model. Condensation and evaporation processes result in similar trends, but they both peak at higher values within the 2D model. In terms of the precipitation itself, the 2D model simulates an overall higher rain rate for non-convective precipitation while areal coverage simulated by both models is comparable.

Differences between the two models during convective precipitation are small, but the 3D model tends to have larger values during this type of precipitation. While overall precipitation areal coverage and rain rate are similar, the 3D model has much larger peaks in the rain rate during times of strong convection. Mean vertical velocities are generally positive, indicating updrafts are dominant. The 3D model simulates larger vertical motion, which in turn is shown through a larger cloud mass flux than the 2D model as well. Heating due to phase changes is similar between both models during this type of precipitation but condensation processes in the 3D model are larger, especially in the middle of the troposphere. This heating could contribute to the larger  $Q_1$  values that are seen within the 3D model.  $Q_2$  is also larger in the 3D model, especially near the surface.

While most thermodynamic properties had only minor differences between the 2D and 3D model, others showed some differences. The 3D model in this study simulates more clouds and cloud cover which is indicated by a larger cloud fraction. The combination of higher and colder cloud tops with stronger vertical motion and mass fluxes suggest that clouds are deeper and better organized within the 3D model. This leads to direct impacts on the radiation budget as increased cloud cover will reflect more incoming shortwave radiation and trap more outgoing longwave radiation, affecting the overall surface energy budget. While the shortwave heating tendency is similar in this study between the 2D and 3D model, less incoming shortwave radiation would result in a smaller shortwave heating tendency in the 3D model. Heating profiles show some difference as  $Q_1$  and heat release from condensation are larger in the 3D model in the middle to upper troposphere, and changes in the radiation budget would impact them as well. A weaker vertical temperature gradient would exist with less surface heating, possibly leading to less instability. Over time, this suggests cooler surface temperatures during times of peak clouds

and convection. Combined with other dynamical atmospheric processes, these cloud feedbacks demonstrate how fluid the atmosphere is and how many processes can attribute to changes in the atmosphere.

Cloud mass fluxes and vertical velocities also demonstrated differences between the 2D and 3D simulations. As previously hypothesized, cloud mass fluxes are shown to be larger within convective clouds and vertical motion is shown to be on average larger within the 3D model compared to the 2D model, supporting past findings (Wilhelmson 1974, Schlesinger 1984, Redelsperger et al. 2000, Phillips and Donner 2006, Zeng 2008, Morrison 2016). This not only has implications on cloud formation and evolution as previously stated, but on other fluxes as well. The average momentum flux for the 3D model is almost 3 to 4 times the average 2D modeled momentum flux. Previous studies have shown that momentum flux differs between 2D and 3D CRMs and suggest that it plays an important role in overall cloud and convection organization (Tao and Soong 1986, Moeng et al. 1996, Tompkins 2000). The largest differences in the momentum flux are seen during the strongest convective periods. The apparent momentum source, while following a similar trend when domain averaged, also shows some difference between the two models when analyzing smaller convective periods as the model domain average reduces the impact of larger variations.

By breaking down the apparent momentum source into its components it is shown that the subsidence term, which is the main term of the momentum source, is similar between the 2D and 3D model during both convective and non-convective periods. But, the pressure gradient term and the detrainment term show larger differences in trend and value between the 2D and 3D model. The pressure gradient is also a main component of the detrainment term, suggesting that

small differences in the pressure gradient leads to impacts on the momentum source and overall momentum budget.

The vertical transport of momentum, while predominately downgradient in both models of this study, indicates some difference during times of clouds and convection. During times of peak convection in the active MJO period, mean flow energy is converted into eddy kinetic energy. This generally agrees with the work of Asai (1970) as the energy conversion seen within the models of this study are the result of longitudinal perturbations. However, there are times within the 2D model that longitudinal perturbations result in upgradient transport, mainly above 12km and once in the lower levels of convection at the end of the period. Also, convection in the 3D is mainly three-dimensional mesoscale cloud clusters as the vertical wind shear is consistent throughout the troposphere. Two-dimensional squall lines are not seen as low-level wind shear is not present. This also supports mainly downgradient transport within the model simulations. While the vertical profile of mean flow energy converted to eddy kinetic energy does indicate slightly more downgradient transport in the 3D model of this study, this average conceals some of the larger variability that occurs between the models during stronger convection. Over time, this larger momentum within the 3D model would contribute to the differences as previously discussed in other variables. Increased vertical motion and larger cloud mass fluxes combined with the greater momentum flux and larger downgradient transport suggest more cloud formation and deeper cloud, thus contributing and continuing the cycle of effects on radiation, heating, energy, and instability within the atmosphere of the 3D model.

Understanding the influence of dimensionality is imperative in order to better understand convective cloud processes within CRMs. Momentum transport and vertical motion play a major role in cloud formation and organization, and the amount and size of these clouds then lead to

impacts among other radiative, heating, and surface processes. Understanding how dimensionality impacts these variables in CRMs can also lead to more evidence of the building block theory of the MJO. The building block theory is centered on the development and structure of clouds and convection to initiate the MJO. By understanding how clouds will form, grow, and interact with dynamical processes in the atmosphere when using a certain type of CRM, it can provide insight as to how GCMs might simulate the initiation and evolution of the MJO if using super-parameterization. If a 3D CRM is used, more clouds, stronger vertical motion, and larger fluxes would be introduced into the GCM affecting the overall simulation. Although a 2D CRM is less computationally expensive, the interaction of cloud properties simulated within a GCM may not be the best representation of the MJO or other climate processes.

Results from this study indicate more clouds within a 3D simulation and suggest that the vertical transport of momentum, vertical motion in clouds, and cloud-scale pressure gradient are sensitive to dimensionality. This may be due in part to impacts from the vertical wind shear within the 3D model. Vertical wind shear plays an important role within the atmosphere and how it changes within the 3D model could lead to direct impacts on the momentum budget and other cloud processes. Future studies should analyze the vertical wind shear to increase understanding on its effects within the atmosphere with the addition of a 3<sup>rd</sup> dimension. Such a study could include idealized 3D simulations using constant forcing and multiple constant wind profiles. By using multiple wind profiles with different amounts of vertical shear, the simulations could be run to equilibrium to further analyze the impact of the wind shear on the momentum budget and cloud organization.

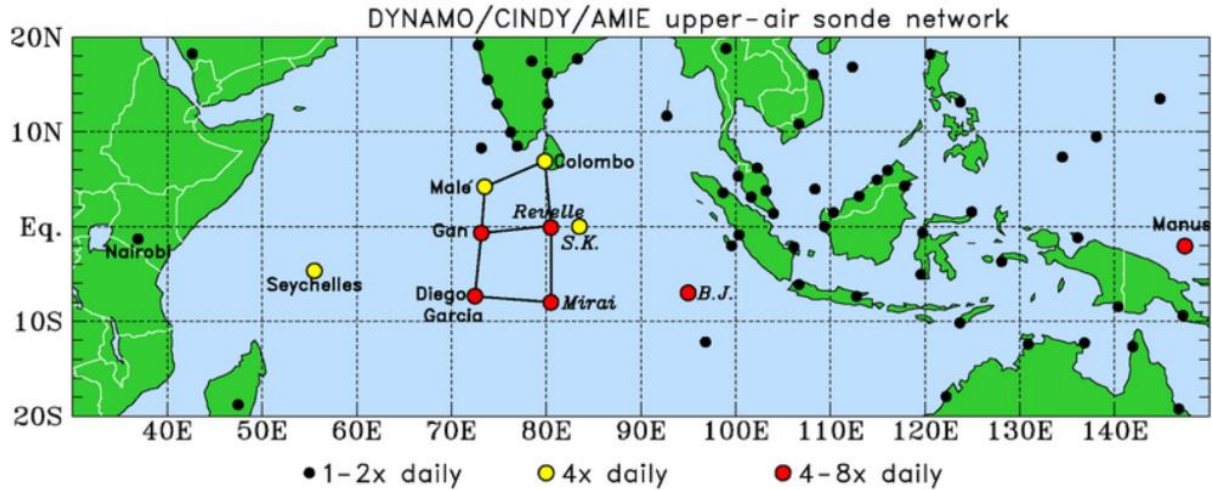


**Figure 1.** The domain of the DYNAMO field experiment, with this research focusing on the Northern Sounding Array.

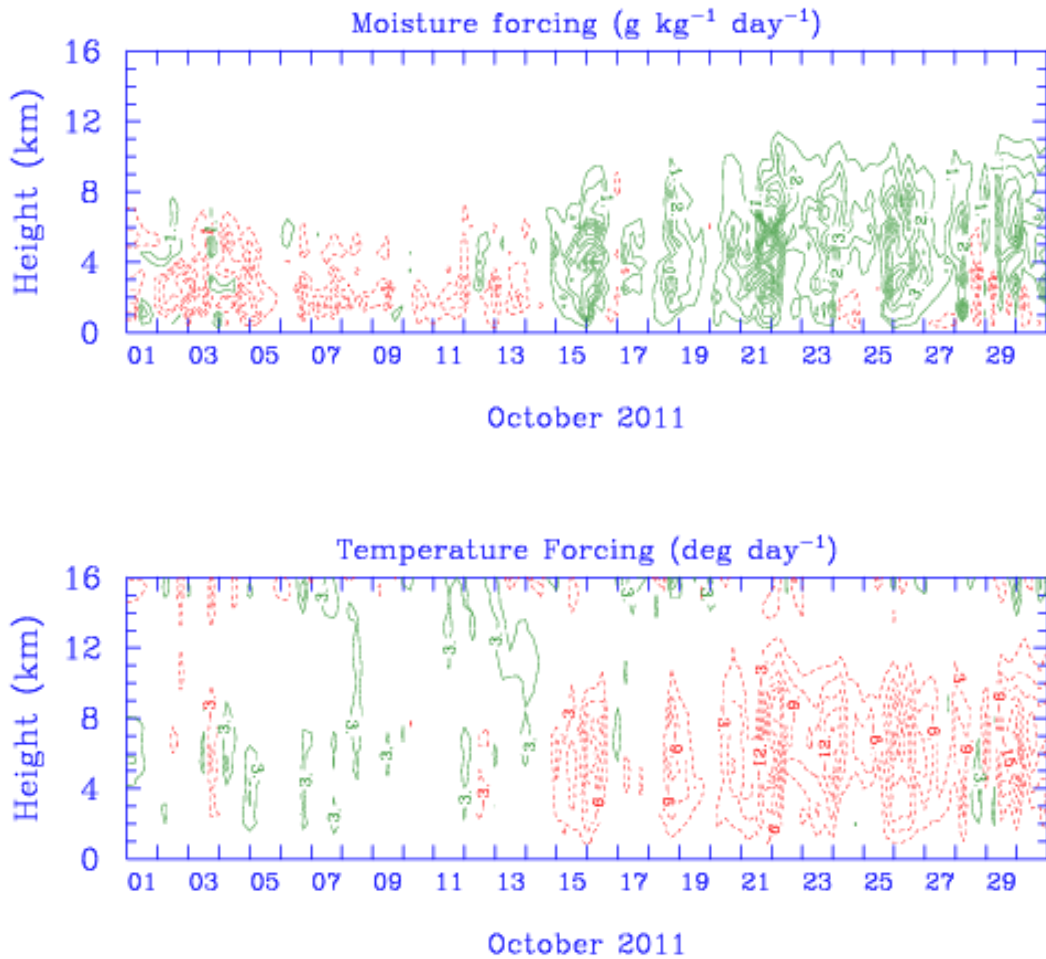


**Figure 2.** Large scale temperature and moisture forcing used within both models, domain averaged over the Northern Sounding Array for 30 days. Green represents positive values while red represents negative values.

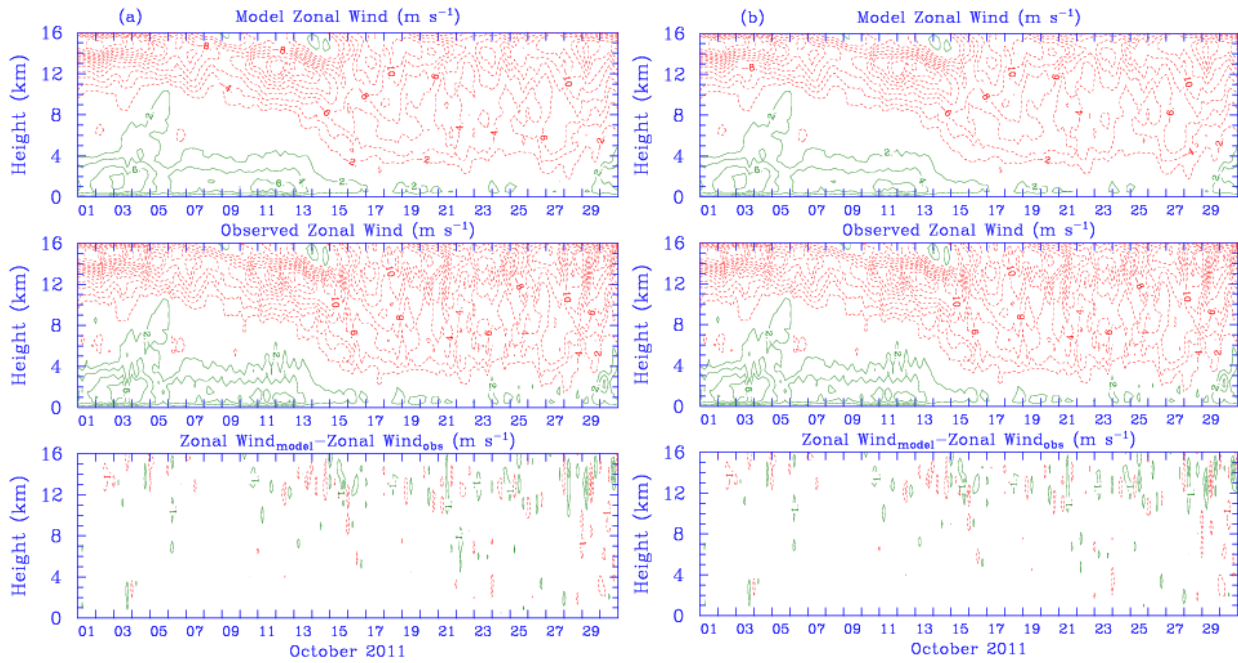


**Figure 3.** The model simulated zonal wind (top), observed wind (middle) and comparison of the observed wind subtracted from the simulated wind (bottom) for the 2D (a) and 3D (b) model domain averaged over the Northern Sounding Array for 30 days. Green represents westerlies while red represents easterlies.

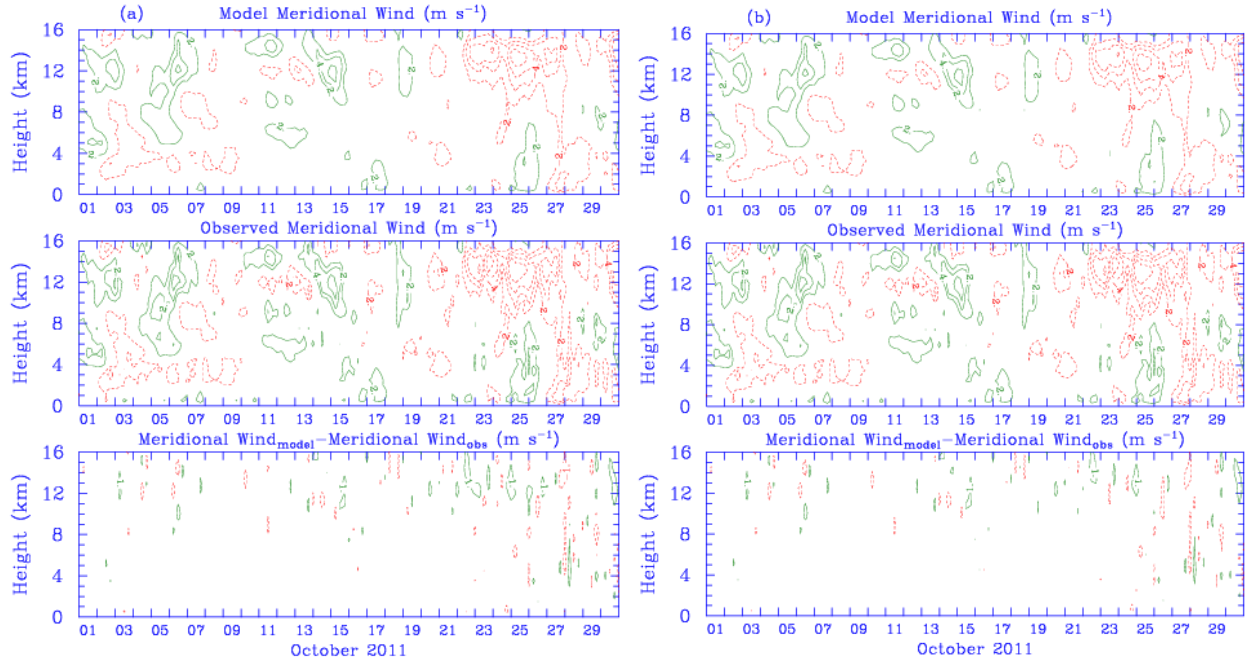


**Figure 4.** The model simulated meridional wind (top), observed wind (middle) and comparison of the observed wind subtracted from the simulated wind (bottom) for the 2D (a) and 3D (b) model domain averaged over the Northern Sounding Array for 30 days. Green represents northerlies while red represents southerlies.

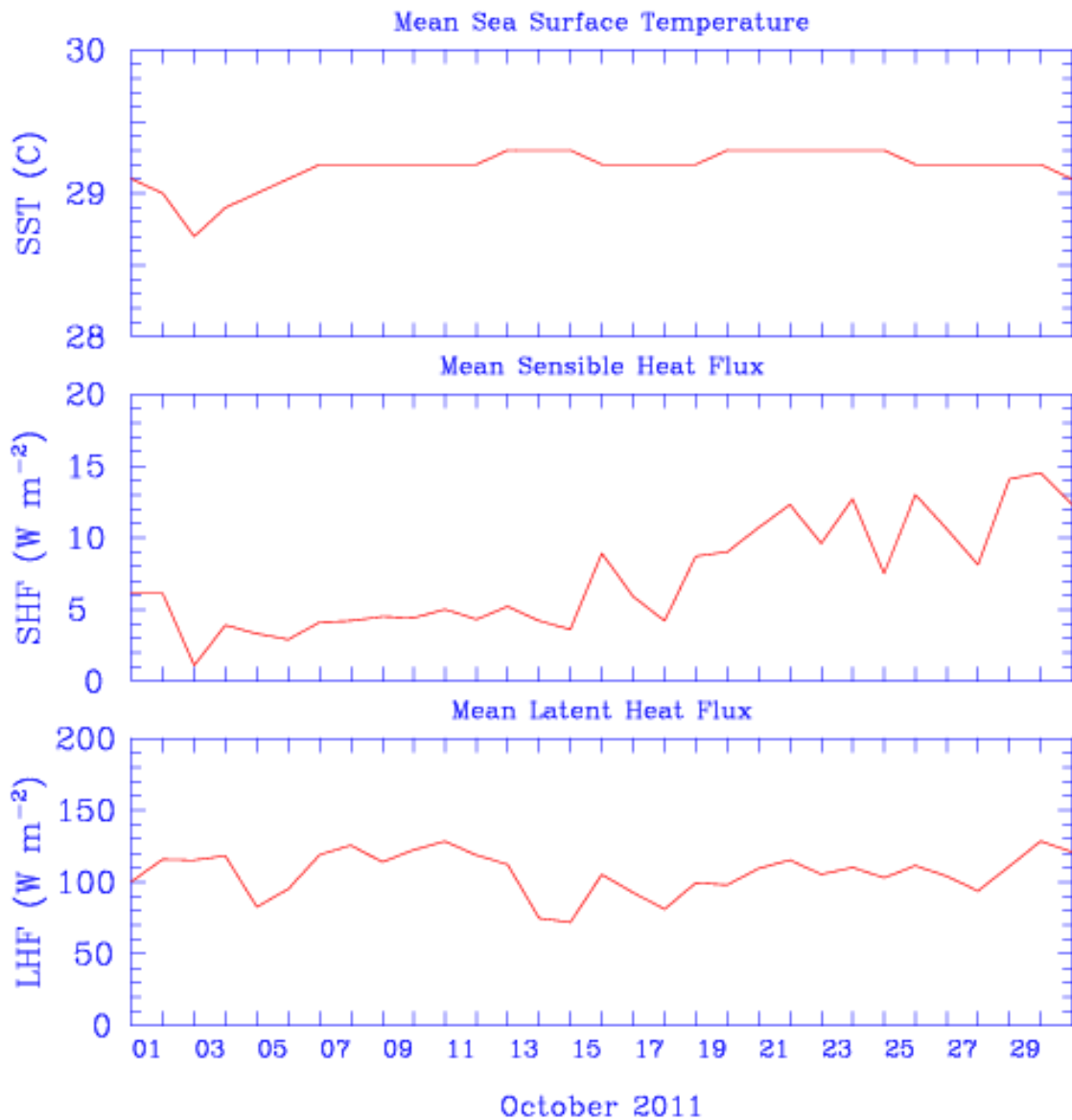


**Figure 5.** Observed surface fluxes of mean sea surface temperature (top), mean sensible heat flux (middle) and mean latent heat flux (bottom) for 30 days over the Northern Sounding Array.

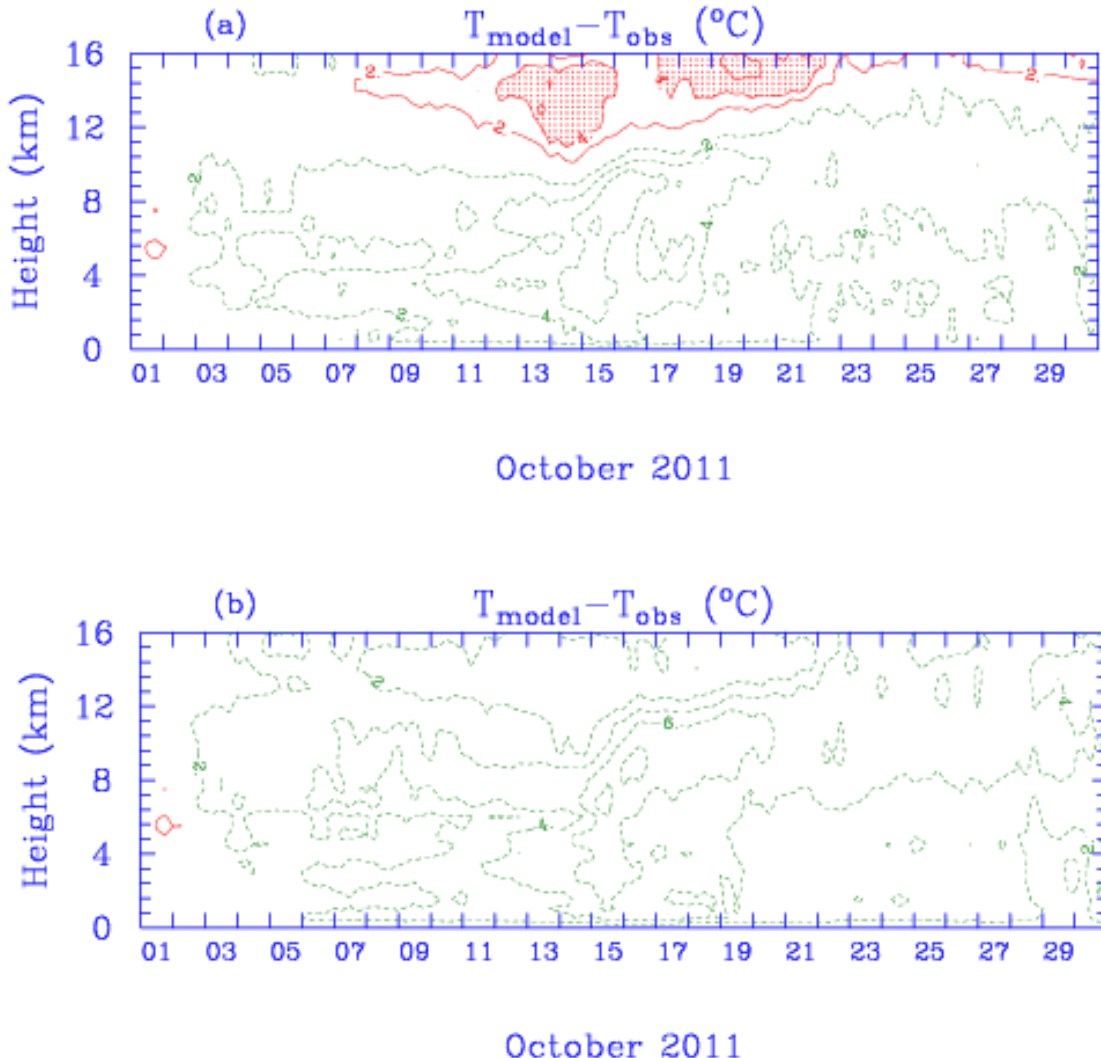


**Figure 6.** Temperature bias of the 2D (a) and 3D (b) model averaged for 30 days over the Northern Sounding Array. The bias is represented by the difference of the modeled temperature and the observed temperature value. Green represents negative values while red represents positive values.

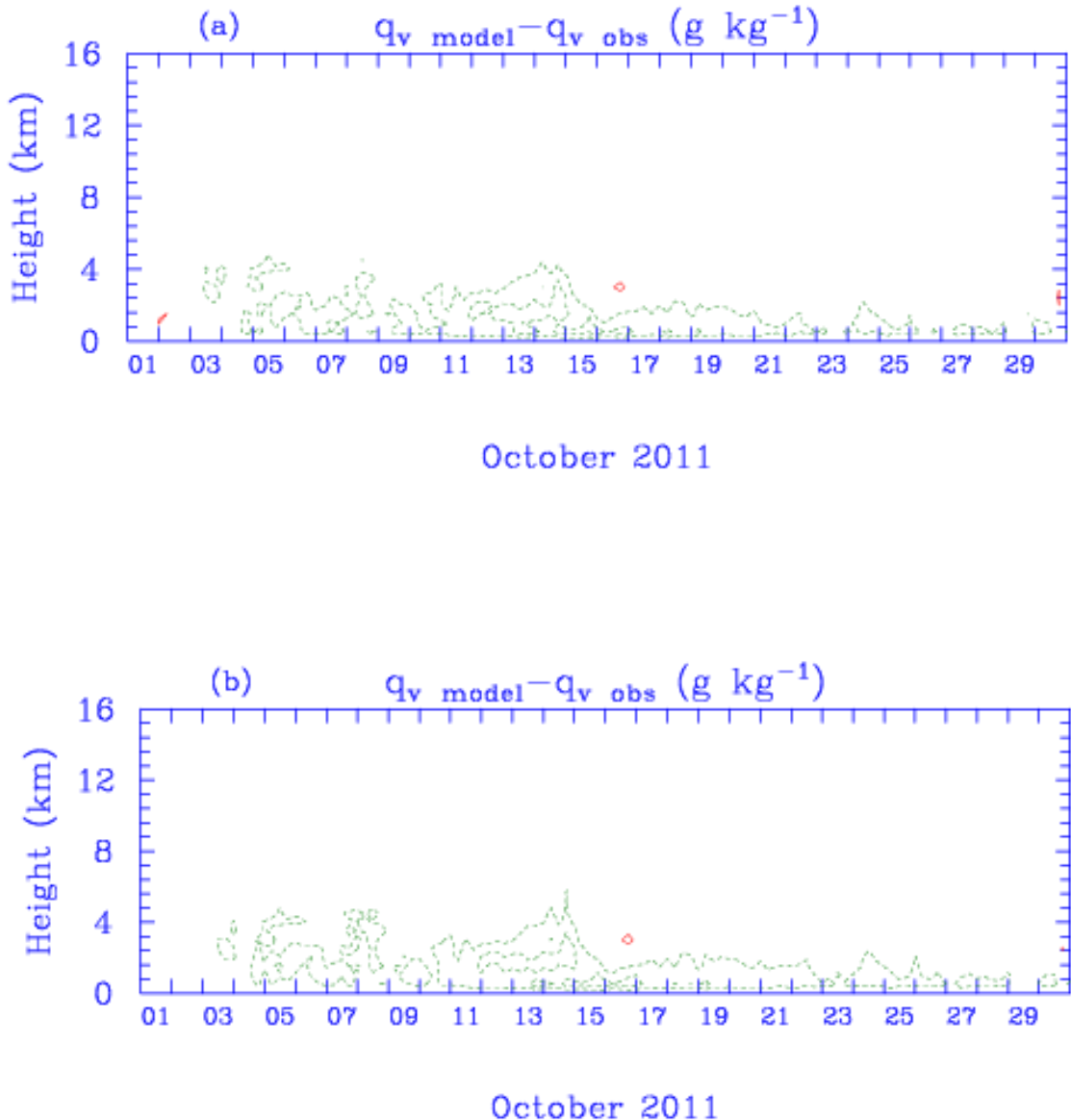


**Figure 7.** Moisture bias of the 2D (a) and 3D (b) model averaged for 30 days over the Northern Sounding Array. The bias is represented by the difference of the modeled moisture and the observed moisture value. Green represents negative values while red represents positive values.

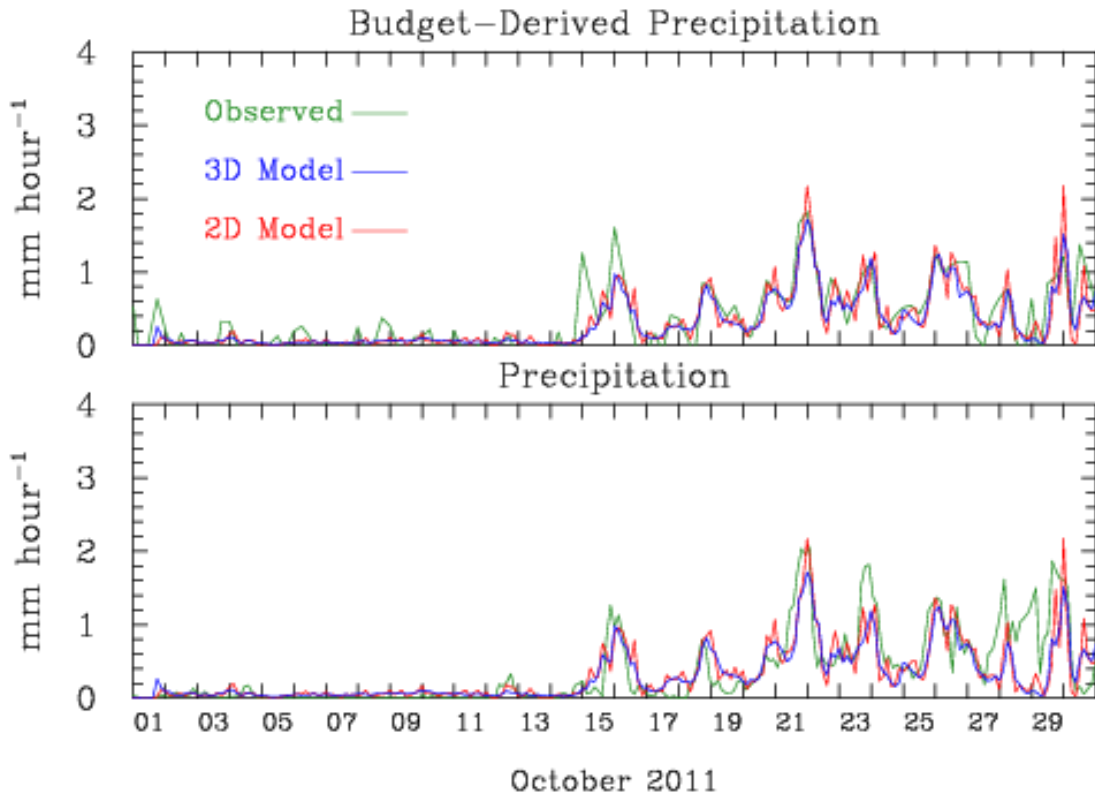


**Figure 8.** Model simulated precipitation compared to budget-derived precipitation and TRMM observed precipitation domain averaged for 30 days over the Northern Sounding Array. Green represents the observed and budget derived precipitation while red and blue represent the 2D and 3D models, respectively.

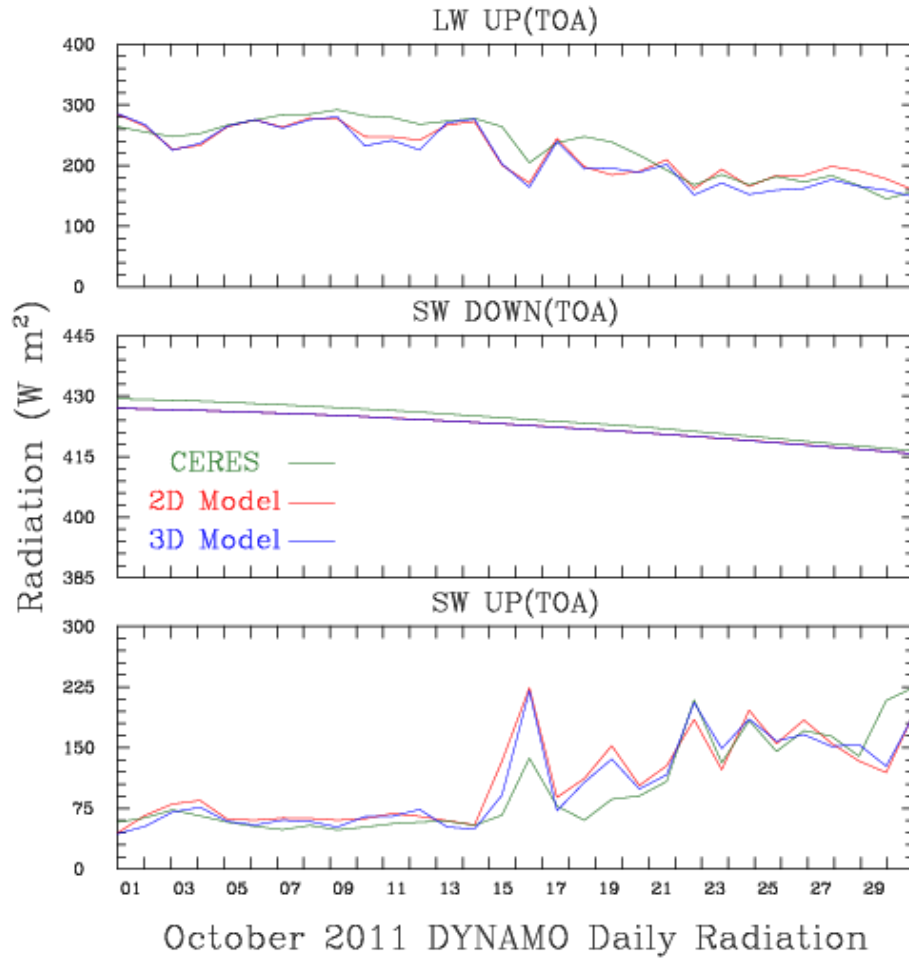


**Figure 9.** Model simulated radiative fluxes at the top of the atmosphere (TOA) compared to observed CERES values. The top figure represents upward longwave radiation, the middle figure represents downward shortwave radiation, and the bottom figure represents upward shortwave radiation. Green represents CERES observations while blue identifies 3D simulated radiation and red identifies 2D simulated radiation.

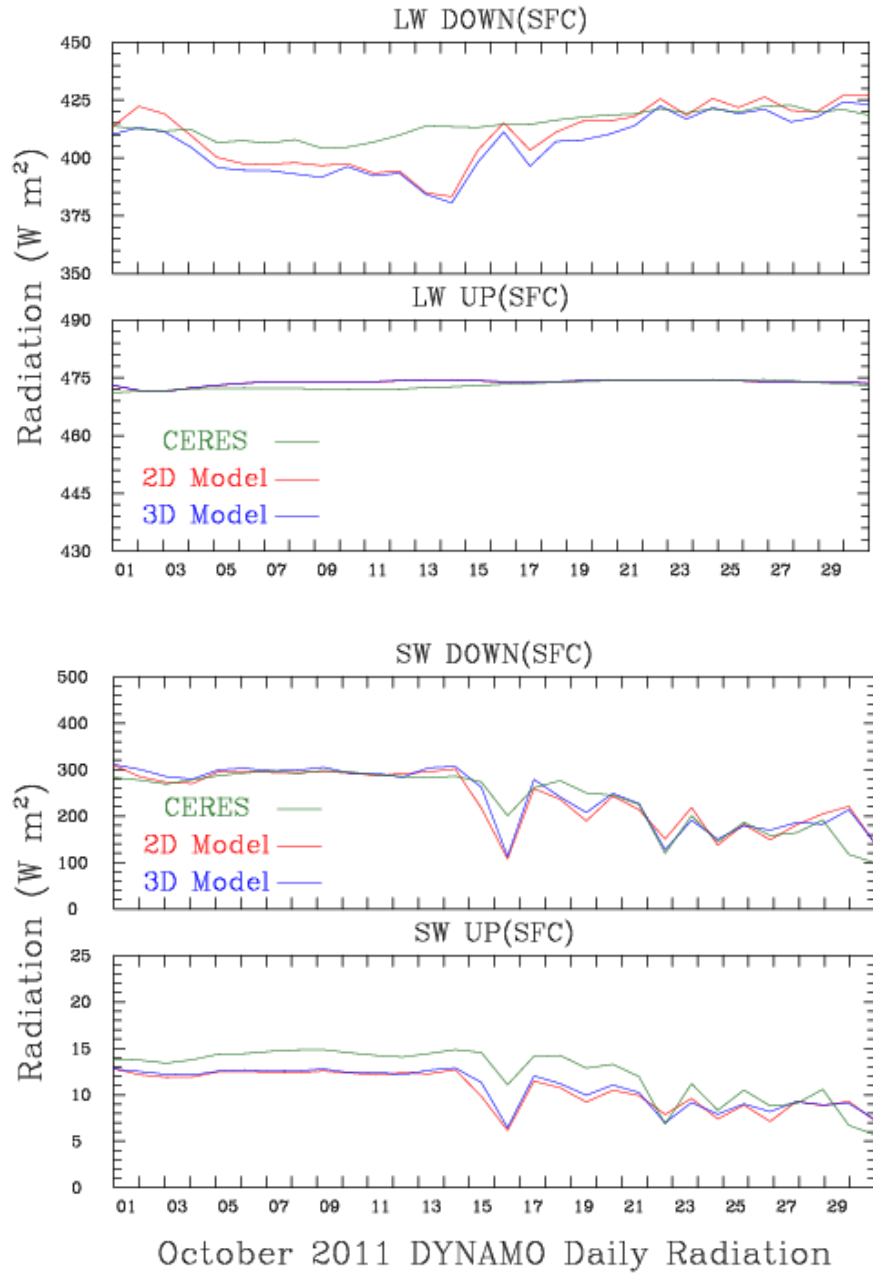


**Figure 10.** Model simulated radiative fluxes at the surface (SFC) compared to observed CERES values. The top figure represents downward longwave radiation, the second figure represents upward longwave radiation, and the bottom figures represents downward shortwave radiation and upward shortwave radiation. Green represents CERES observations while blue identifies 3D simulated radiation and red identifies 2D simulated radiation.

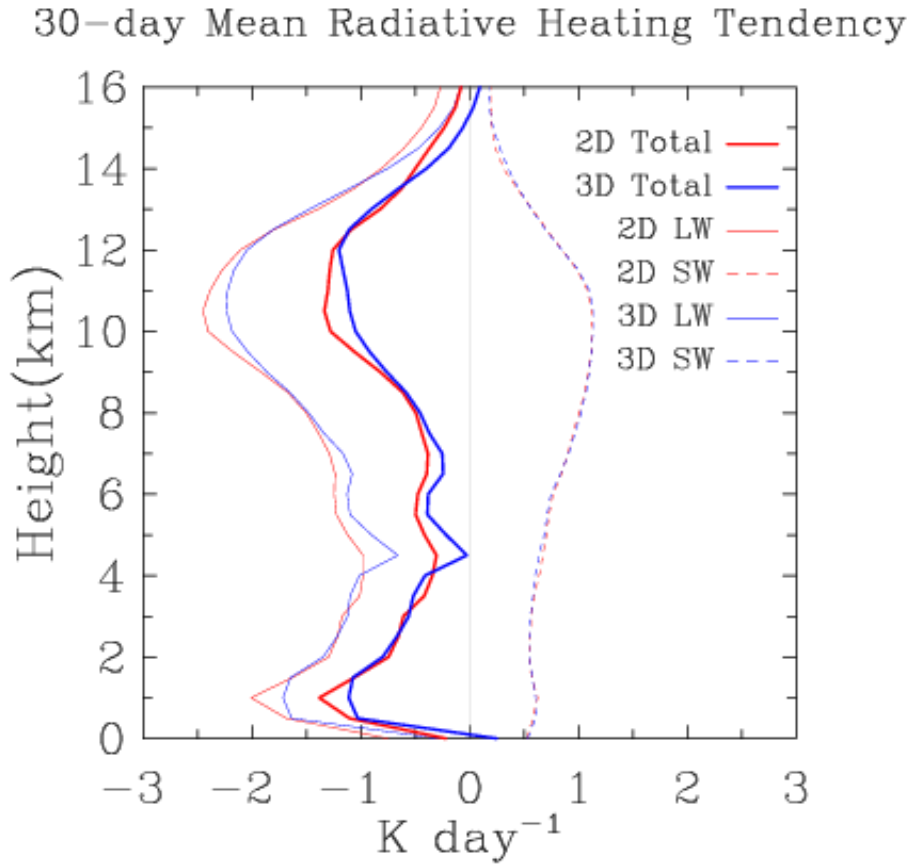


**Figure 11.** Vertical profile of time and domain averaged shortwave and longwave radiative heating tendencies. Red lines represent the 2D model while blue lines represent the 3D model. Solid lines represent the longwave tendency and dashed lines represent the shortwave tendency.

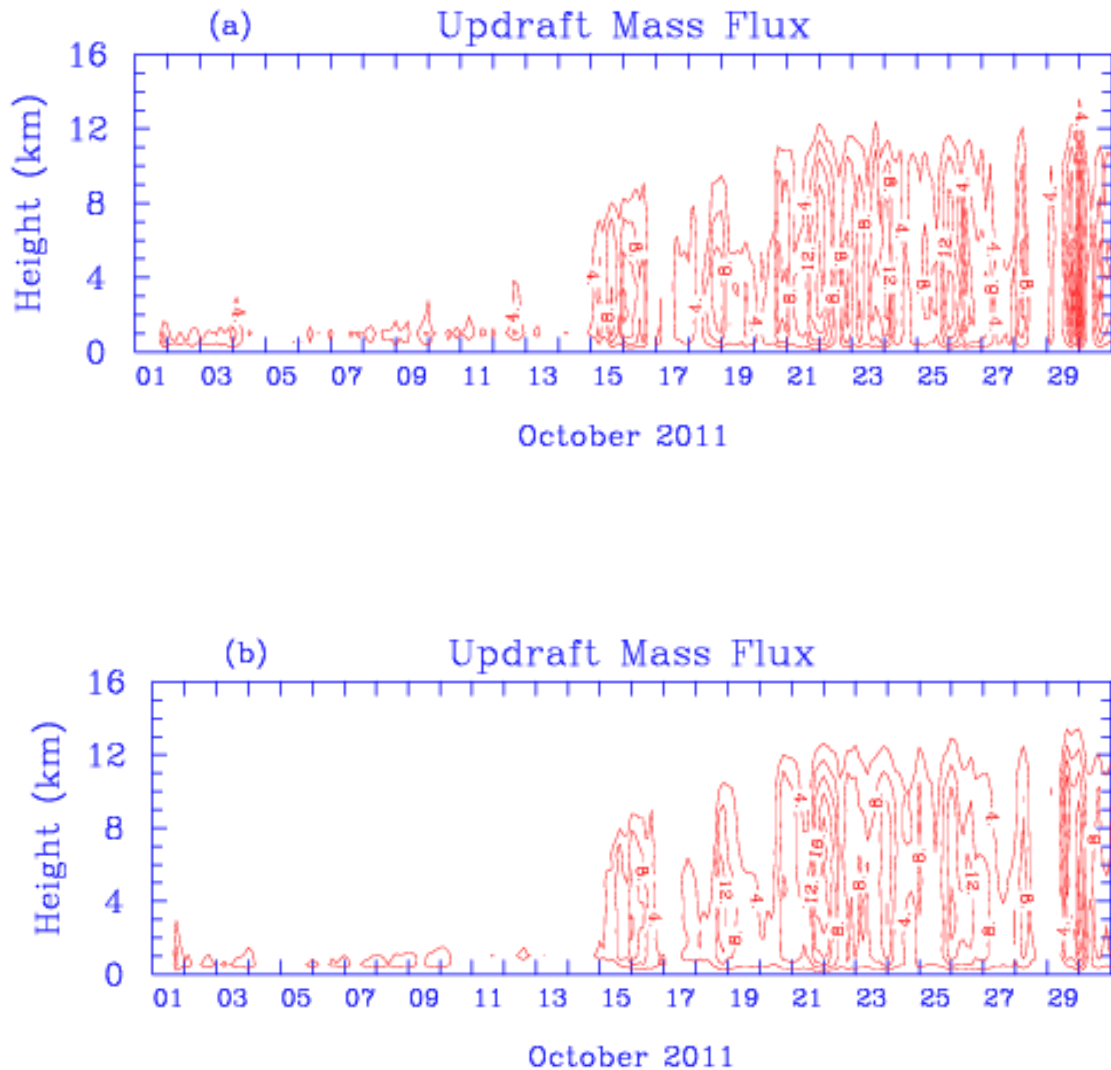


**Figure 12.** 2D (a) and 3D (b) modeled updraft mass flux (Mb/hr) domain averaged over the Northern Sounding Array for 30 days.

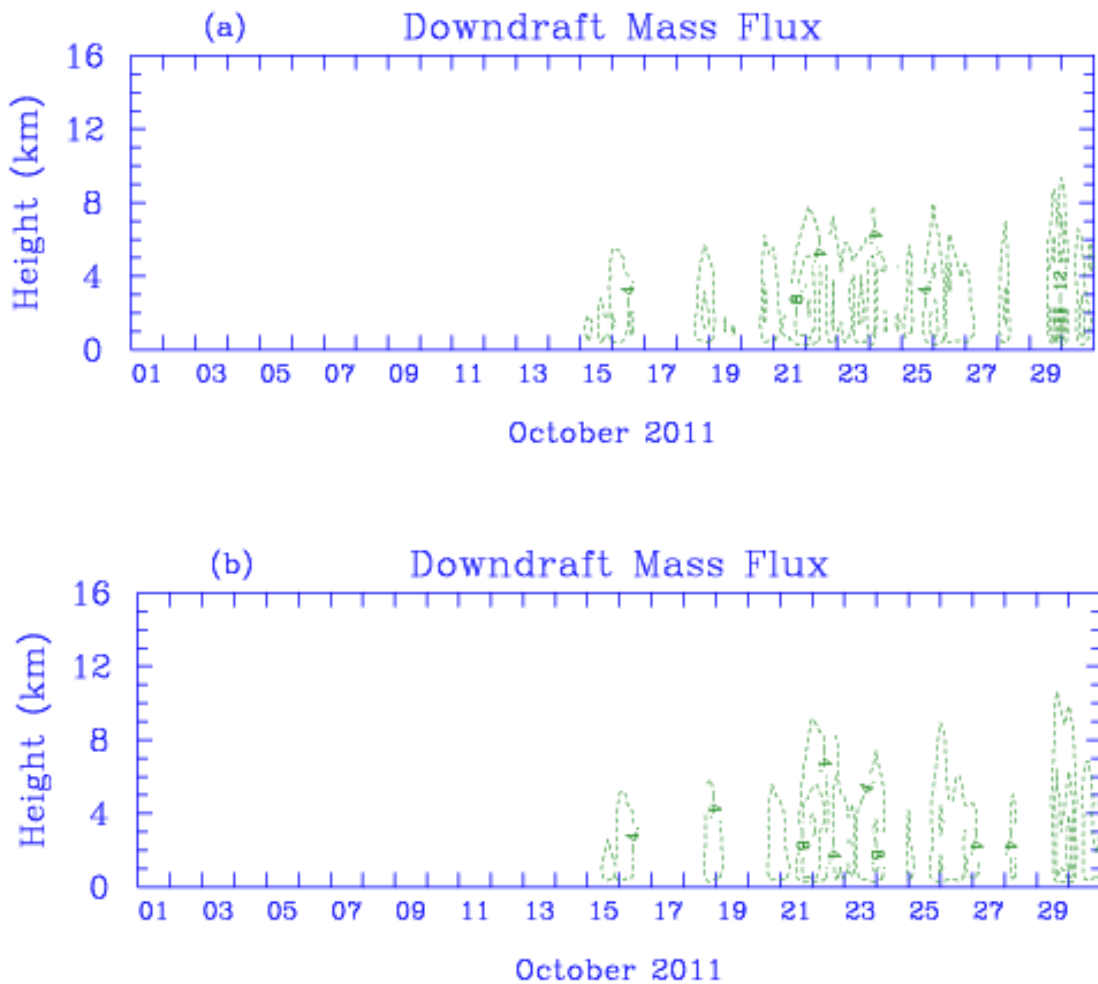


**Figure 13.** 2D (a) and 3D (b) modeled downdraft mass flux (Mb/hr) domain averaged over the Northern Sounding Array for 30 days.

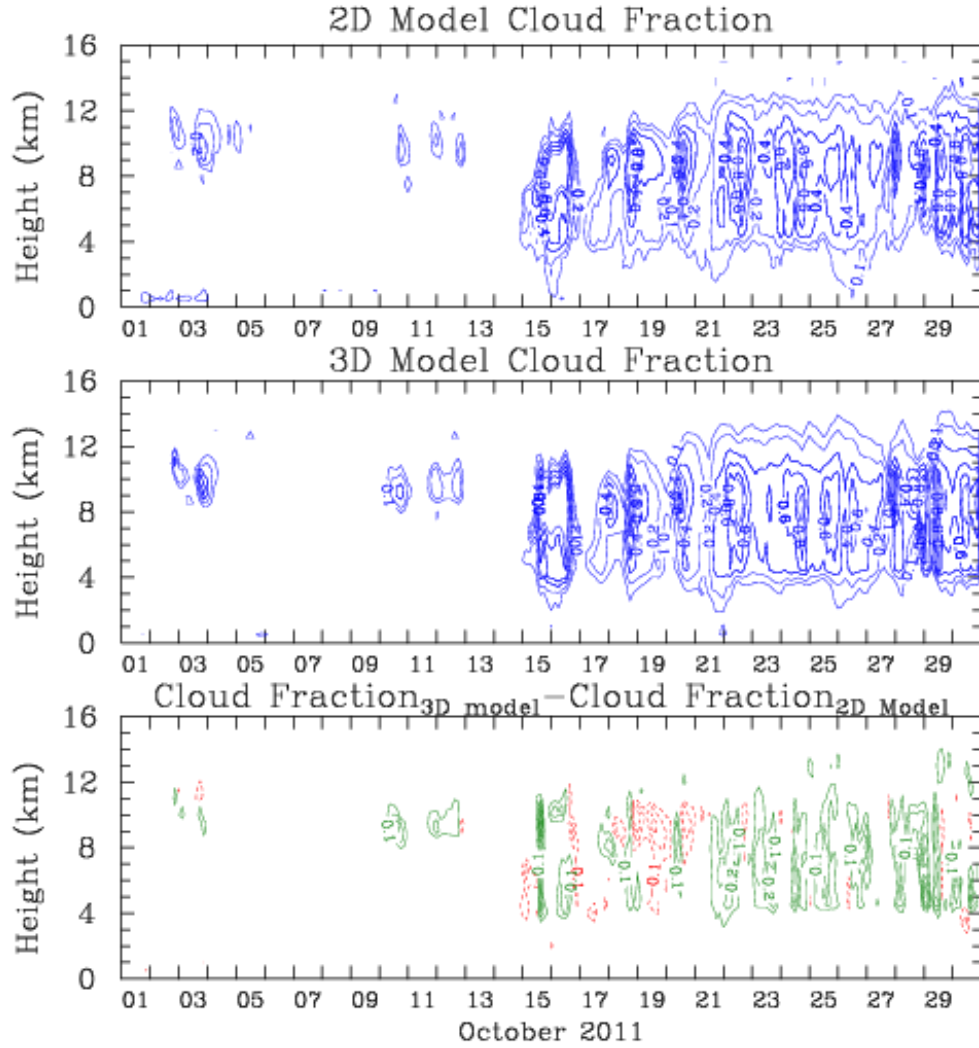


**Figure 14.** Model simulated cloud fraction averaged over the Northern Sounding Array for 30 days. The top figure represents the 2D model cloud fraction, the middle figure represents the 3D model cloud fraction, and the bottom figure represents the difference between the modeled cloud fraction. For the bottom figure, green represents positive values while red represents negative values.

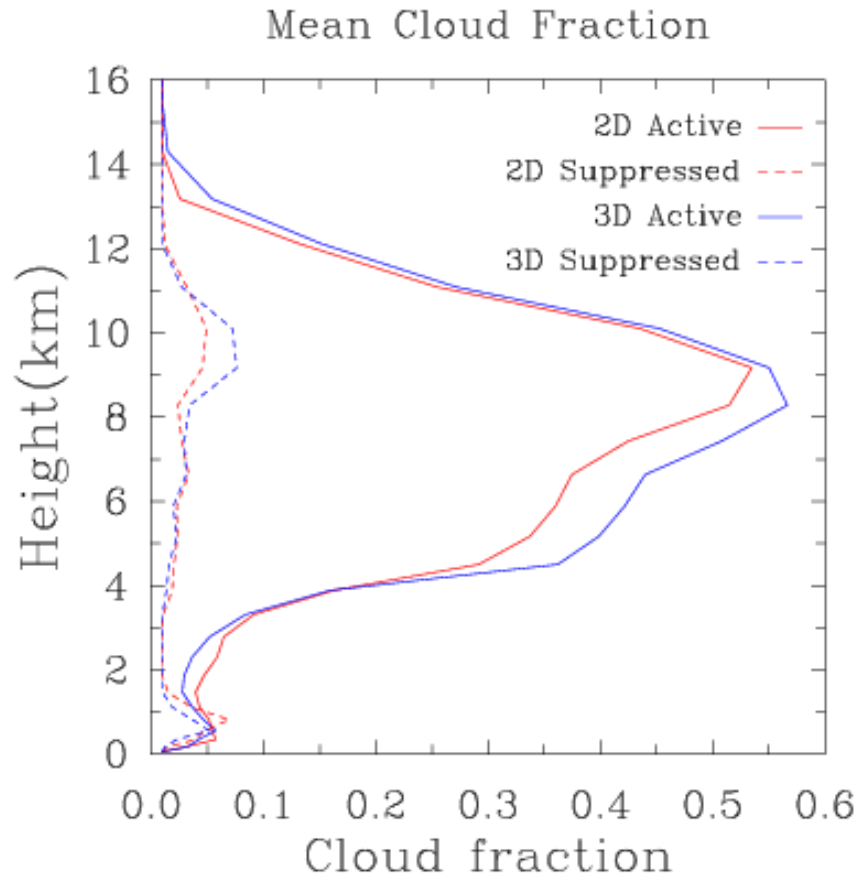


**Figure 15.** Vertical profile of domain and time averaged cloud fraction. Red represents the 2D model while blue represents the 3D model and solid lines represent the active MJO phase while dashed lines represent the suppressed MJO phase.

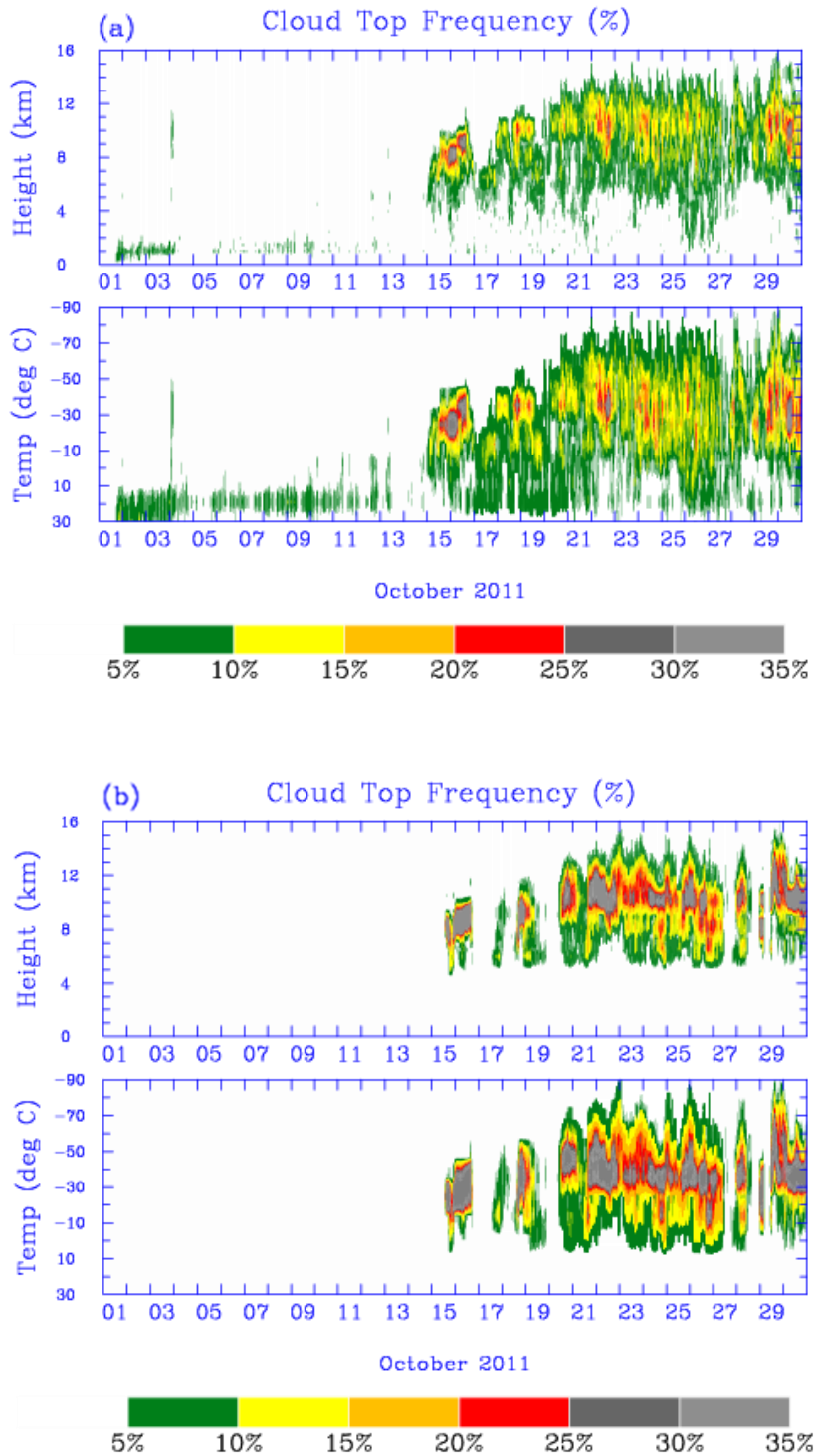


**Figure 16.** 2D (a) and 3D (b) modeled cloud top frequency domain averaged over the Northern Sounding array for 30 days. The top figure represents the cloud top frequency based on height and the bottom figure represents the cloud top frequency based on cloud top temperature.

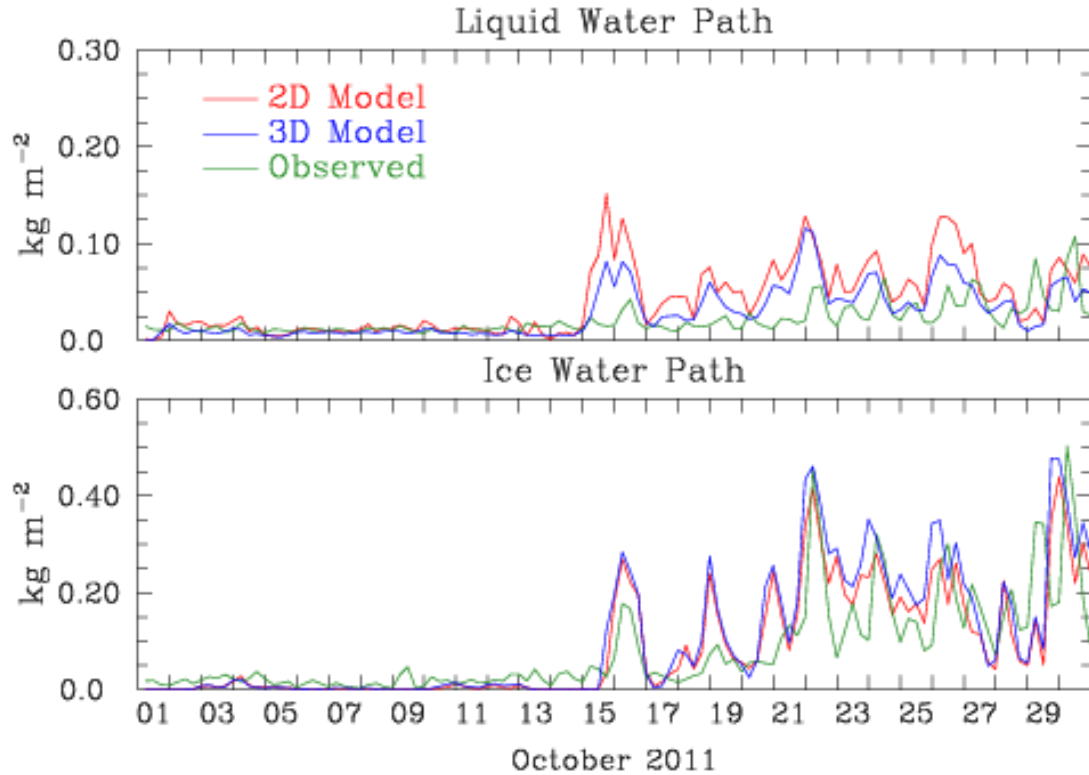


**Figure 17.** Cloud liquid and ice water path domain averaged over the Northern Sounding array for 30 days. The top figure represents the liquid water path while the bottom figure represents the ice water path. Red lines depict the 2D model, blue lines represent the 3D model, and green lines represent the observed data.

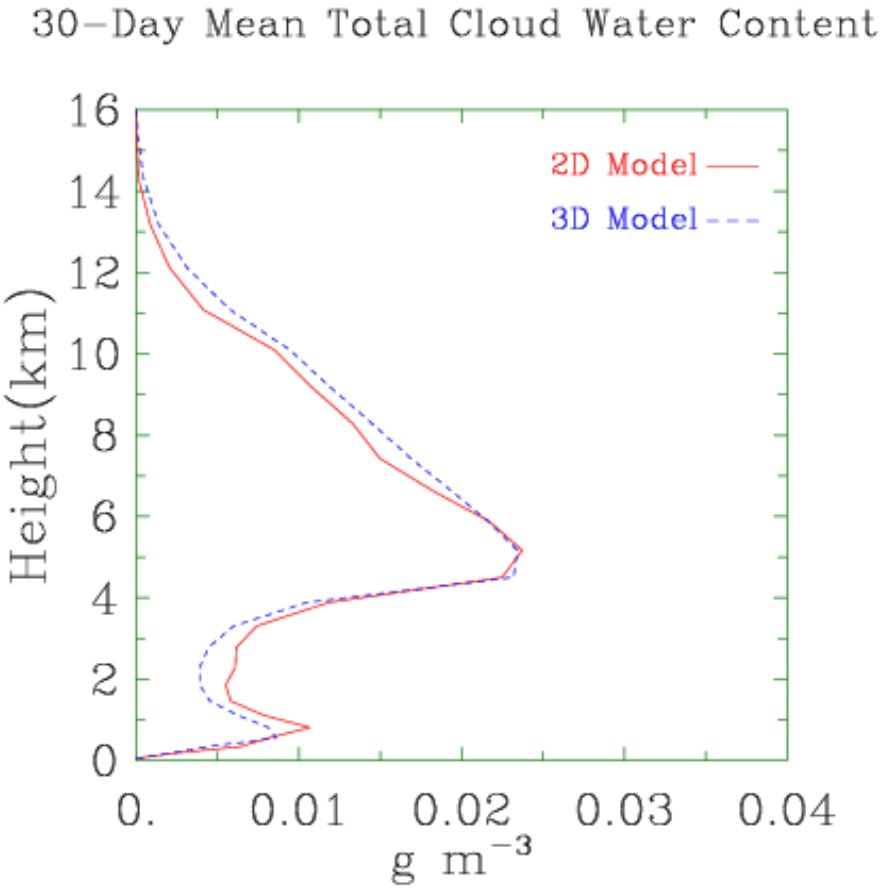


**Figure 18.** Vertical profile of domain and time averaged model simulated total cloud water content. Red represents the 2D model while blue represents the 3D model.

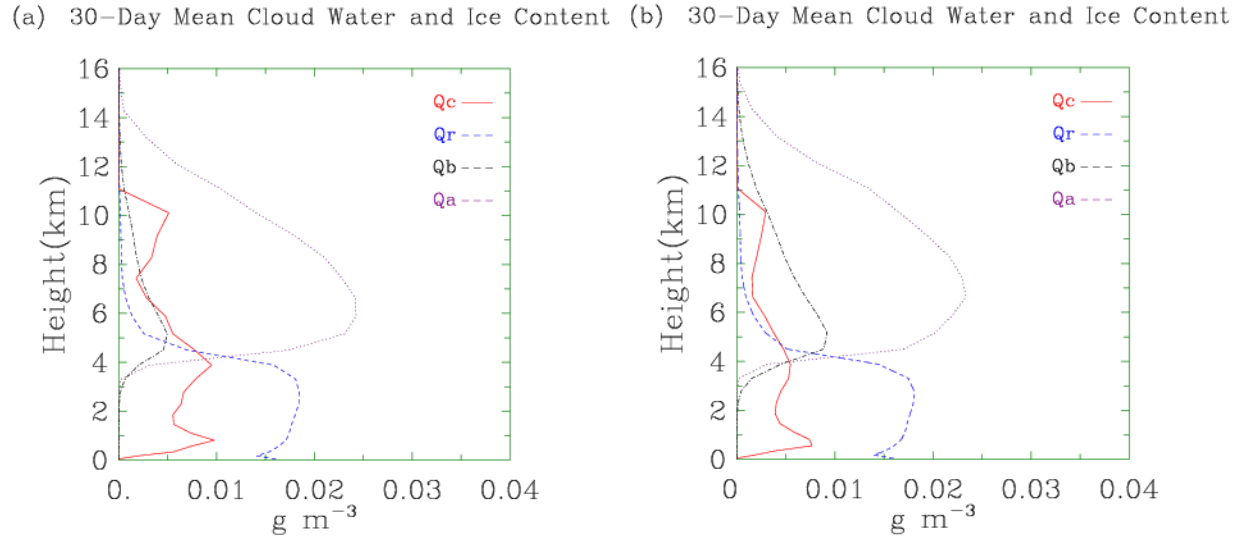


**Figure 19.** Vertical profile of domain and time averaged 2D (a) and 3D (b) simulated ice and water content. Red represents  $Q_c$ , blue represents  $Q_r$ , black represents  $Q_b$ , and purple represents  $Q_a$ .

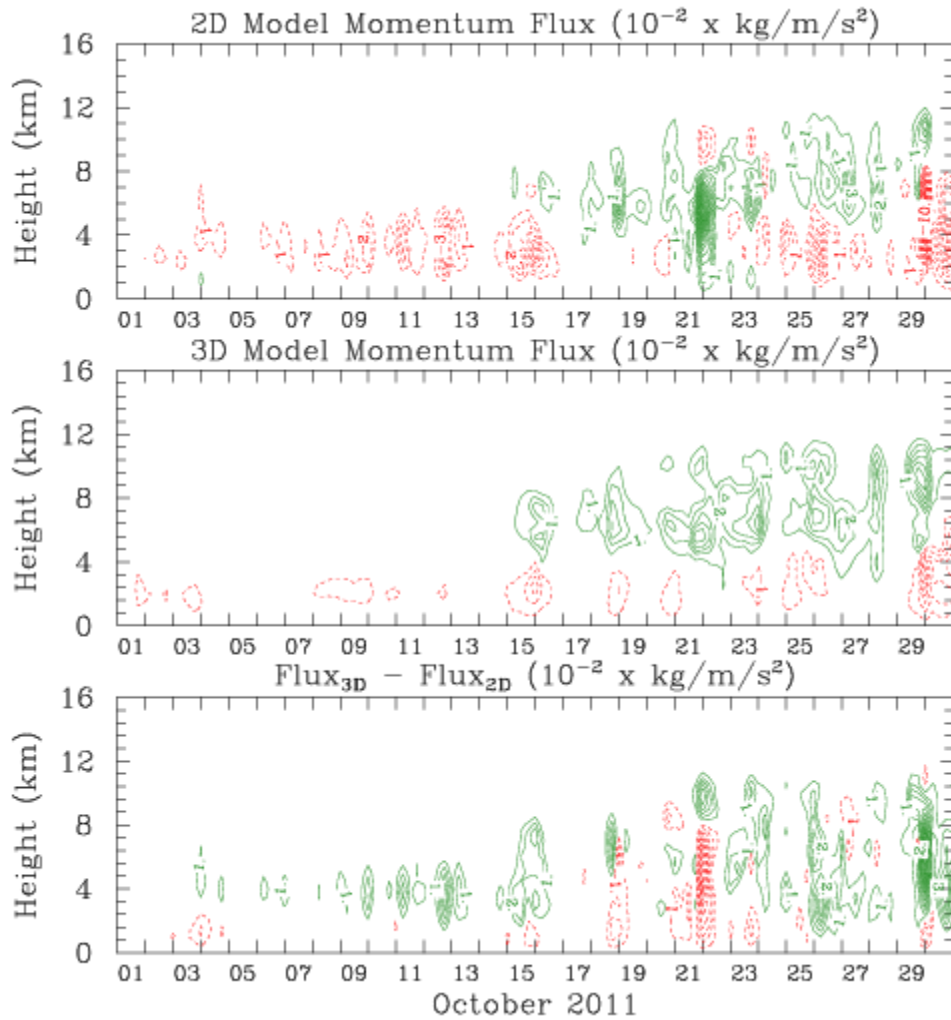


**Figure 20.** 2D simulated vertical momentum flux (top), 3D simulated vertical momentum flux (middle), difference between the 3D and 2D model (bottom) domain averaged over the Northern Sounding Array for 30 days. Red represents negative momentum flux values while green represents positive momentum flux values.

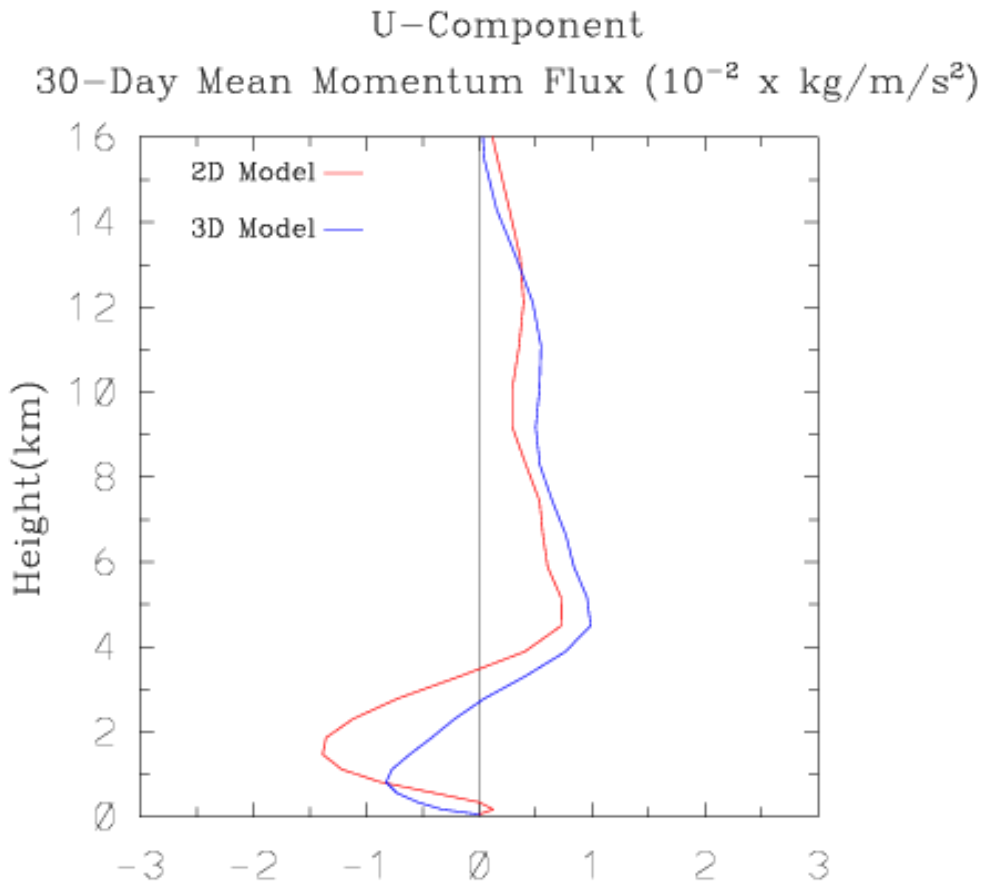


**Figure 21.** Vertical profile of time and domain averaged mean momentum flux from the u-component. Red lines represent the 2D model while blue lines represent the 3D model.

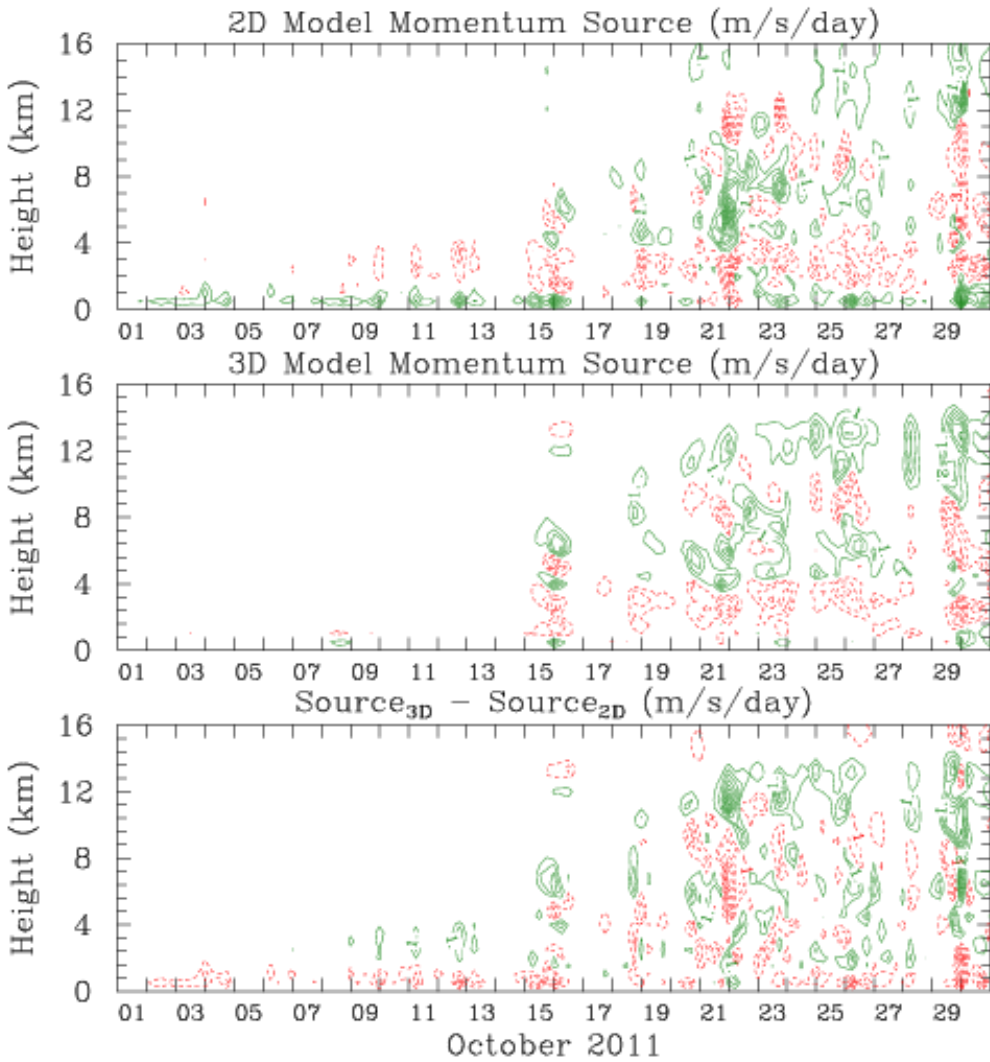


**Figure 22.** 2D simulated momentum source (top), 3D simulated momentum source (middle), and the difference between the 3D and 2D model (bottom) domain averaged over the Northern Sounding Array for 30 days. Red represents negative momentum source values while green represents positive momentum source values.

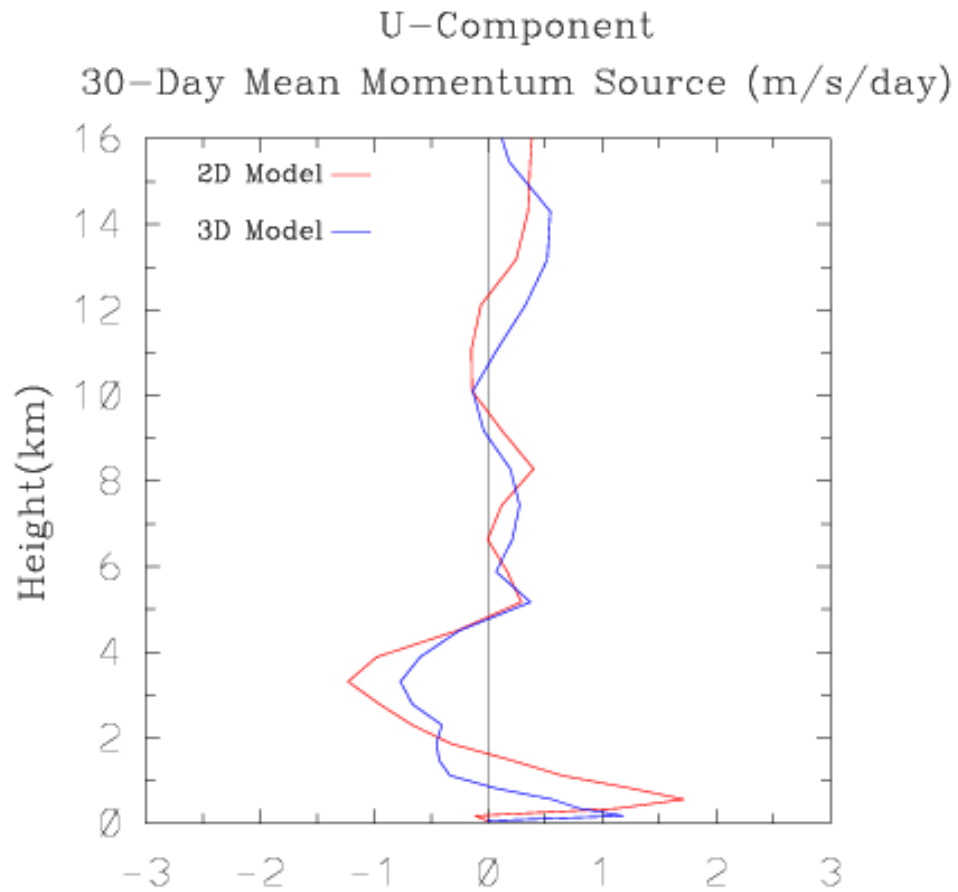


**Figure 23.** Vertical profile of time and domain averaged apparent momentum source. Red lines represent the 2D model while blue lines represent the 3D model.

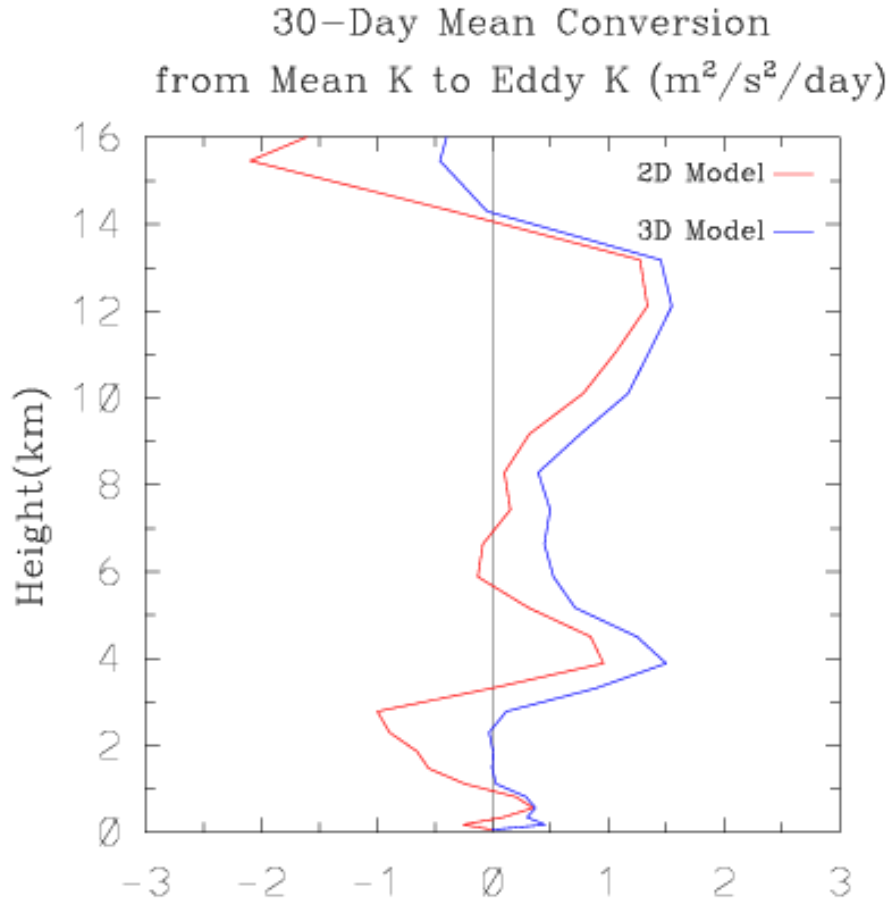


**Figure 24.** Vertical profile of time and domain averaged conversion of mean flow to eddy kinetic energy due to momentum transport. Red lines represent the 2D model and blue lines represent the 3D model.

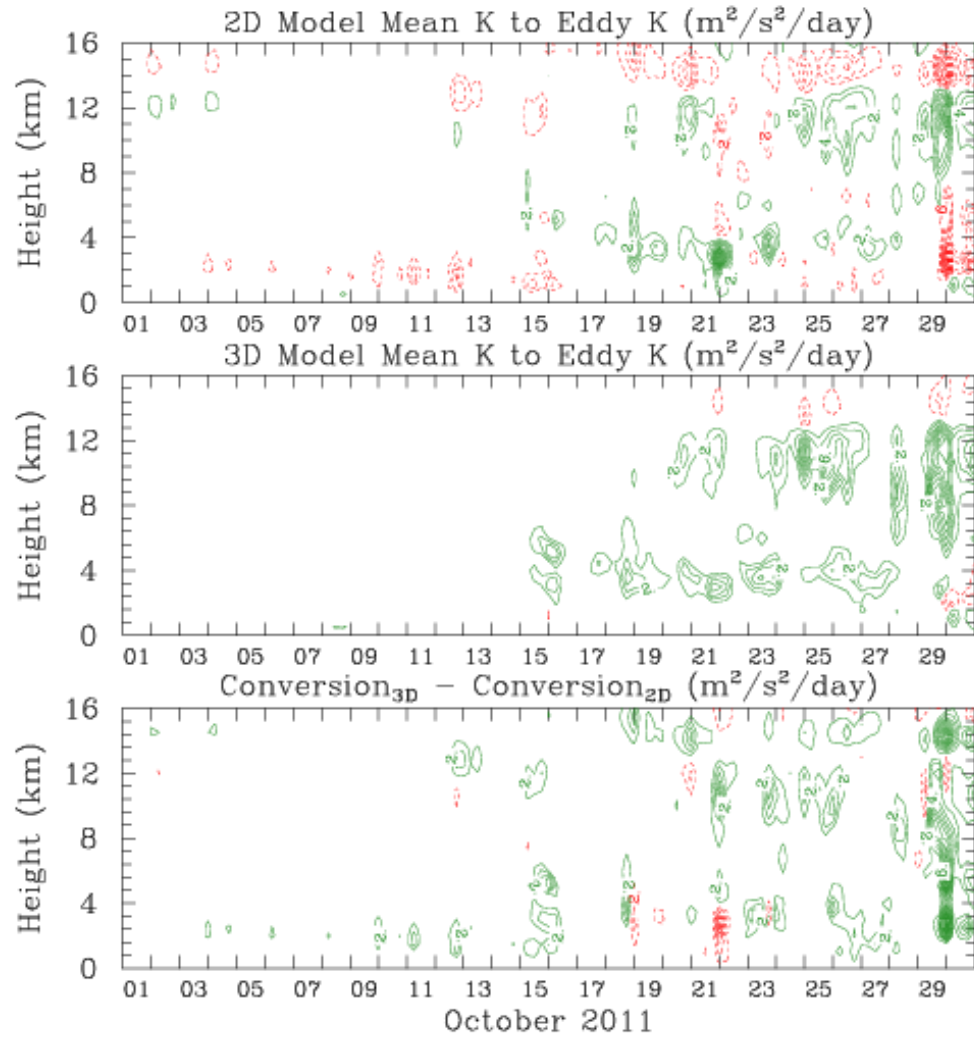


**Figure 25.** 2D simulated mean K to eddy K conversion (top), 3D simulated mean K to eddy K conversion (middle), and the difference between the 3D and 2D model (bottom) domain averaged over the Northern Sounding Array for 30 days. Red represents negative conversion values while green represents positive conversion values.

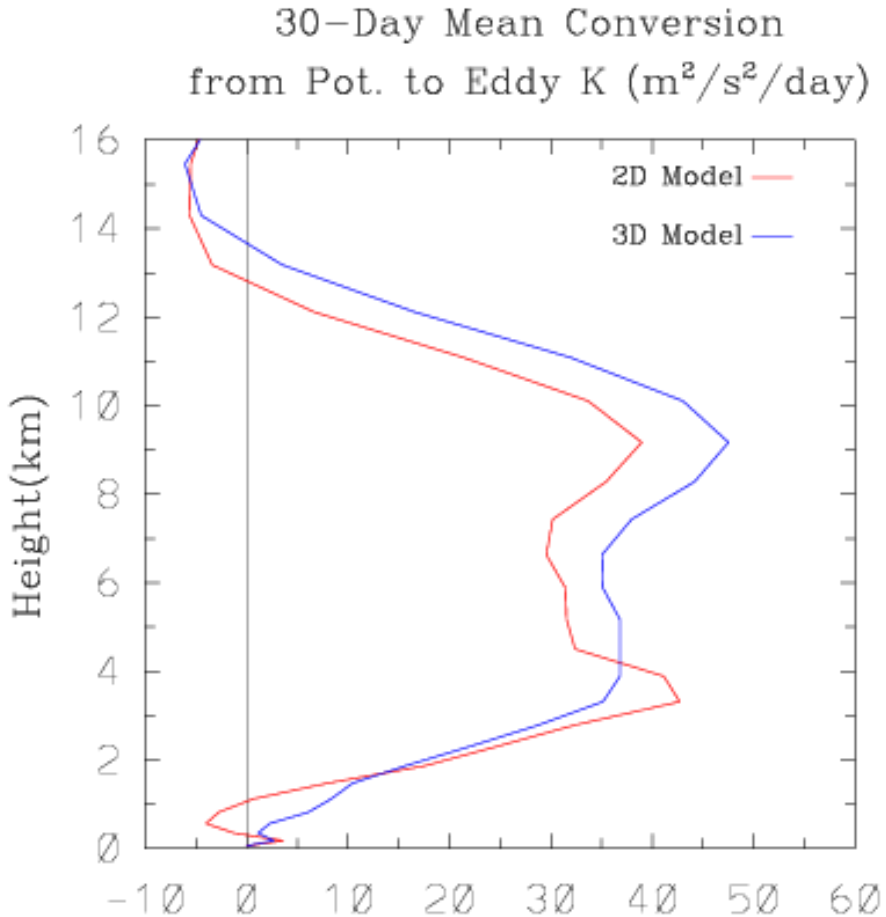


**Figure 26.** Vertical profile of time and domain averaged conversion of potential energy to eddy kinetic energy due to momentum transport. Red lines represent the 2D model and blue lines represent the 3D model.

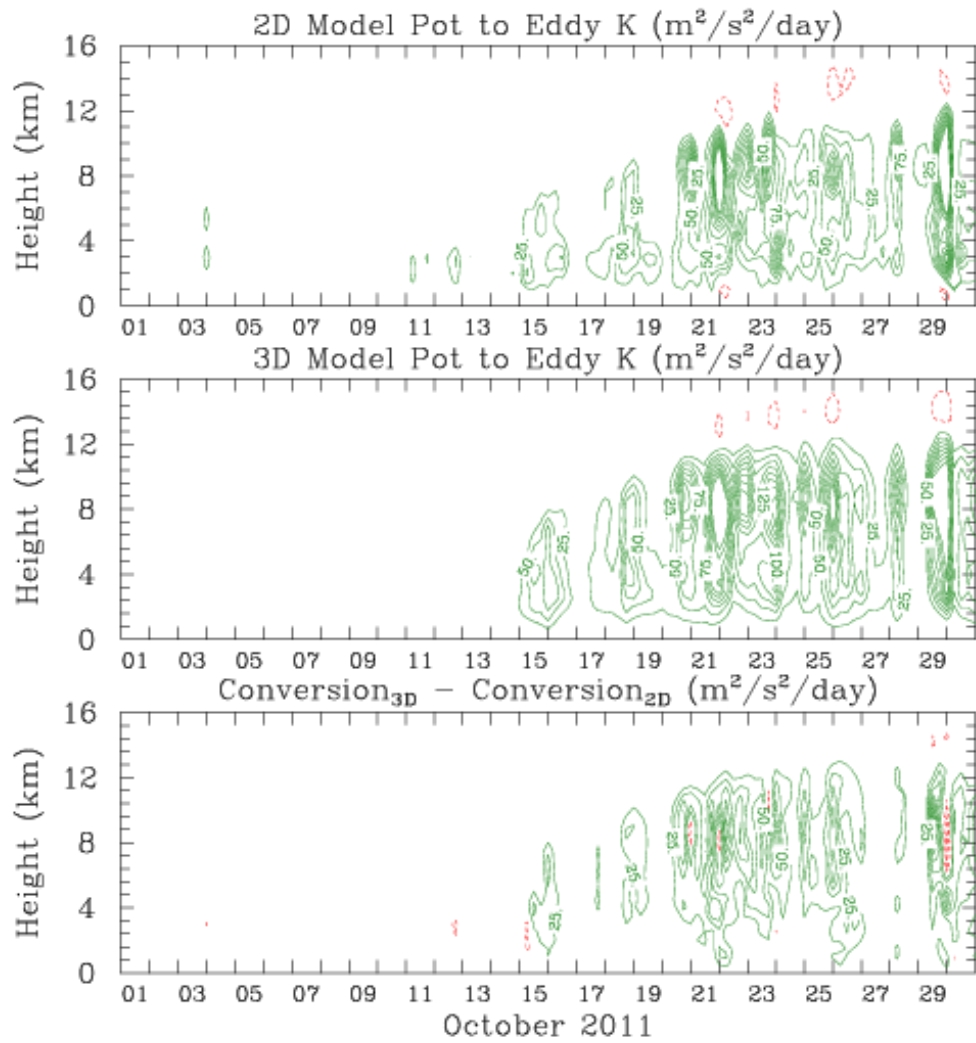


**Figure 27.** 2D simulated potential energy to eddy K conversion (top), 3D simulated potential energy to eddy K conversion (middle), and the difference between the 3D and 2D model (bottom) domain averaged over the Northern Sounding Array for 30 days. Red represents negative conversion values while green represents positive conversion values.

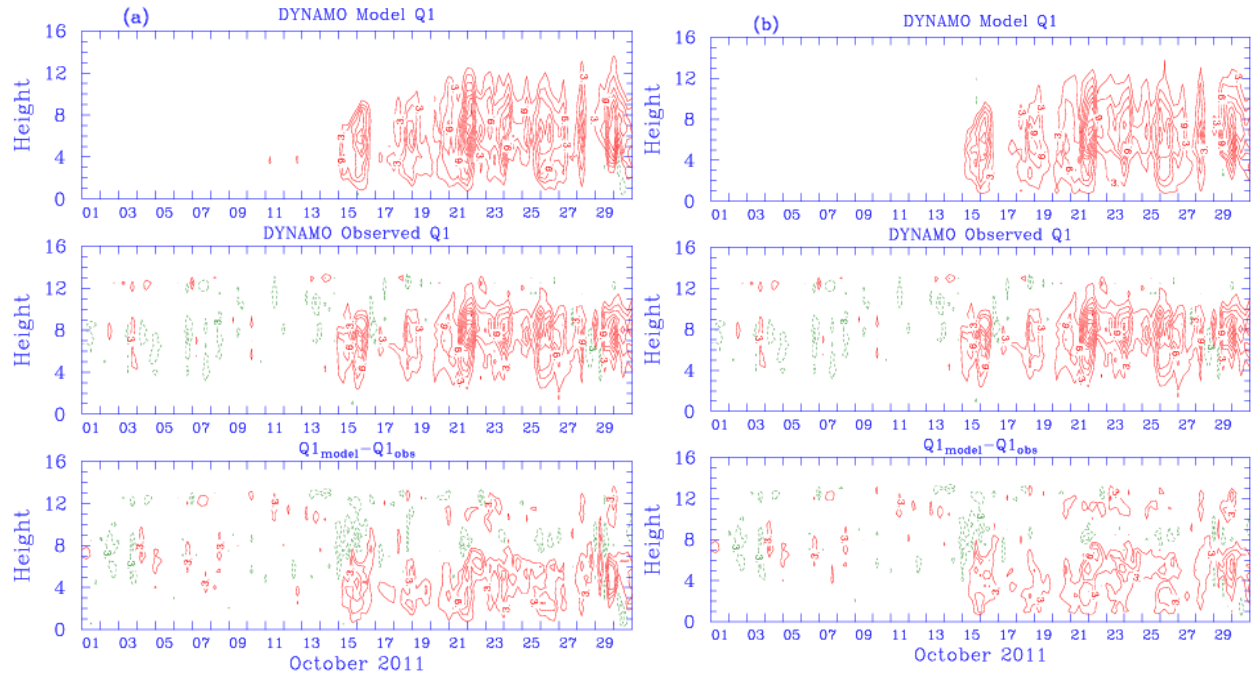


**Figure 28.** 2D (a) and 3D (b) simulated  $Q_1$  (top),  $Q_1$  calculated based on observations (middle), and the difference between the 3D modeled  $Q_1$  and observed  $Q_1$  domain averaged over the Northern Sounding Array for 30 days. Red represents positive  $Q_1$  values while green represents negative  $Q_1$  values.

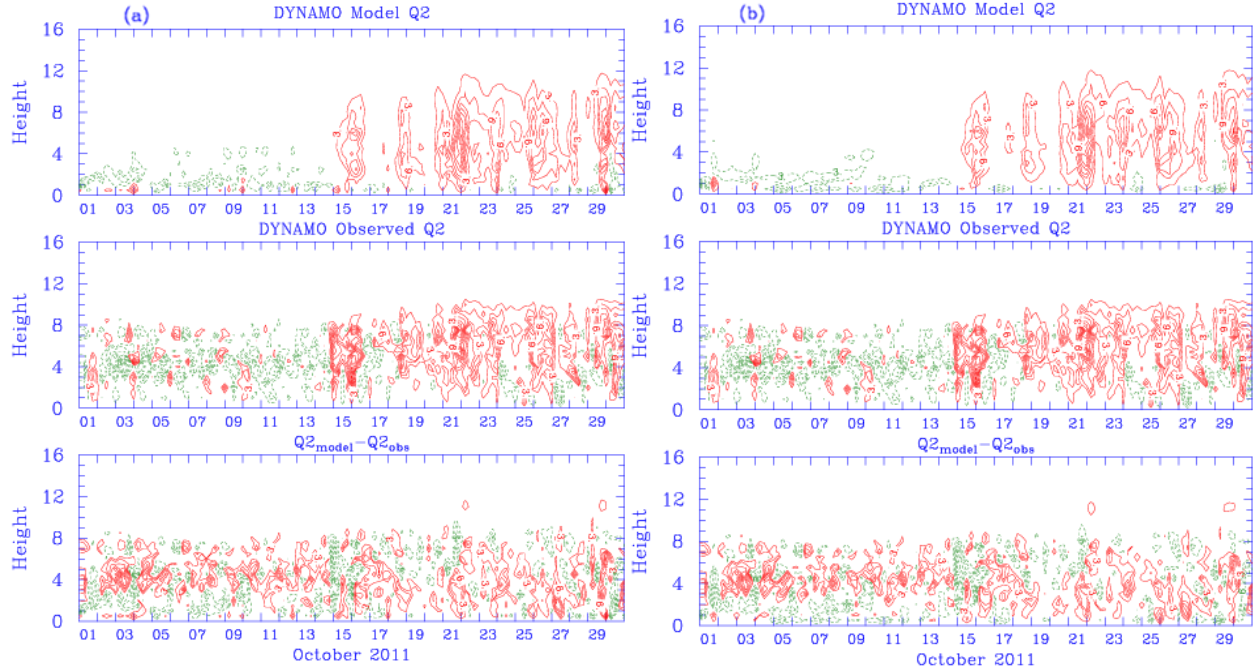


**Figure 29.** 2D (a) and 3D (b) simulated  $Q_2$  (top),  $Q_2$  calculated based on observations (middle), and the difference between the 3D modeled  $Q_2$  and observed  $Q_2$  domain averaged over the Northern Sounding Array for 30 days. Red represents positive  $Q_2$  values while green represents negative  $Q_2$  values.

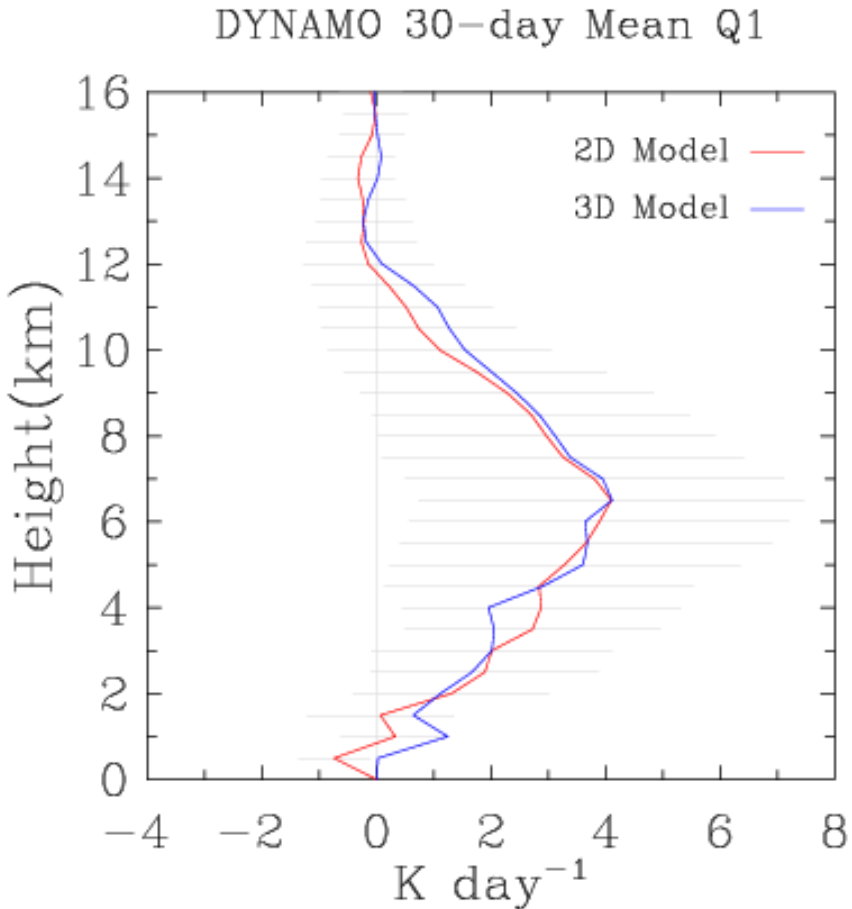


**Figure 30.** Vertical profile of time and domain averaged  $Q_1$  simulated over the Northern Sounding Array. Blue lines represent the 3D model while red lines represent the 2D model.

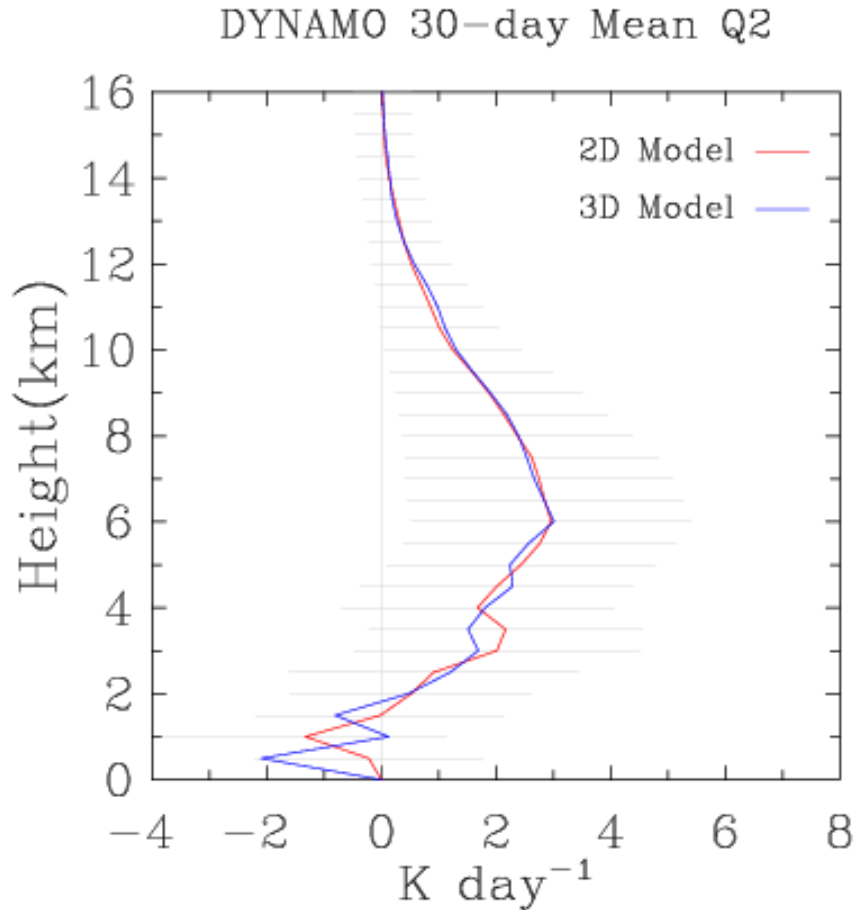


**Figure 31.** Vertical profile of time and domain averaged  $Q_2$  simulated over the Northern Sounding Array. Blue lines represent the 3D model while red lines represent the 2D model.

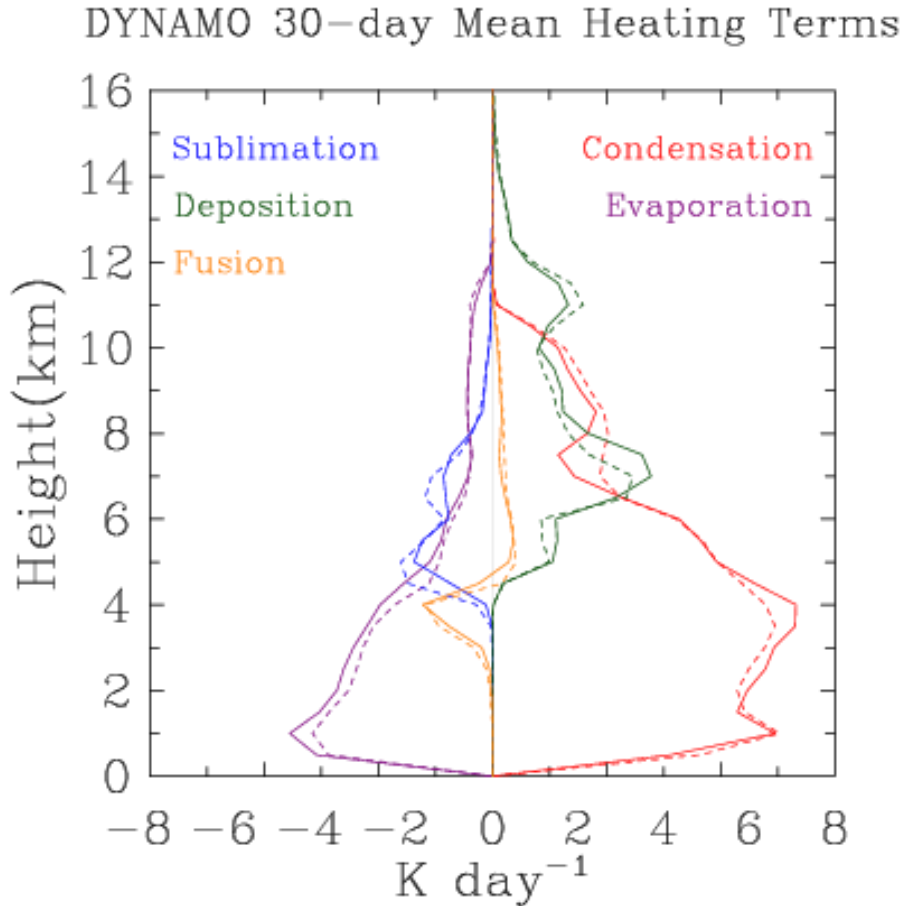


**Figure 32.** Vertical profile of time and domain averaged phase change heating terms simulated over the Northern Sounding Array. Red lines represent condensation, blue represents sublimation, green represents deposition, yellow represents fusion, and purple represents evaporation. Solid lines represent the 2D model while dashed lines represent the 3D model.

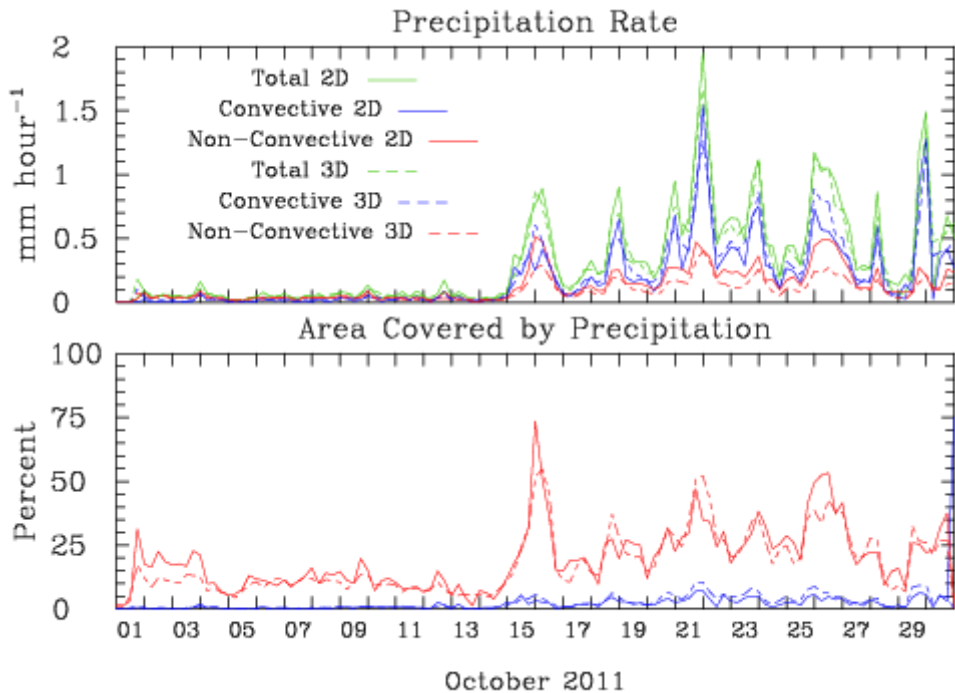


**Figure 33.** Model simulated convective and non-convective precipitation domain averaged over the Northern Sounding Array for 30 days. The top figure represents the precipitation rate and the bottom figure represents the domain area covered by precipitation. Red lines represent non-convective precipitation, blue lines represent convective precipitation, and purple lines represent total precipitation.

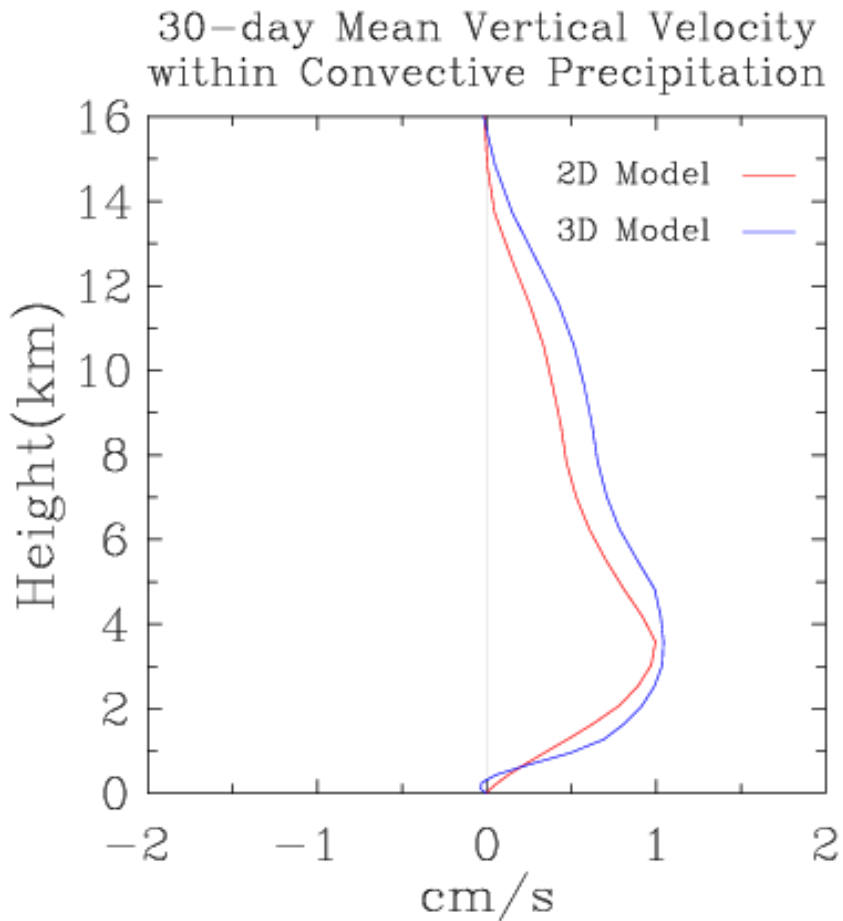


**Figure 34.** Vertical profile of time and domain averaged model simulated vertical motion within convective precipitation. Red represents the 2D model while blue represents the 3D model.

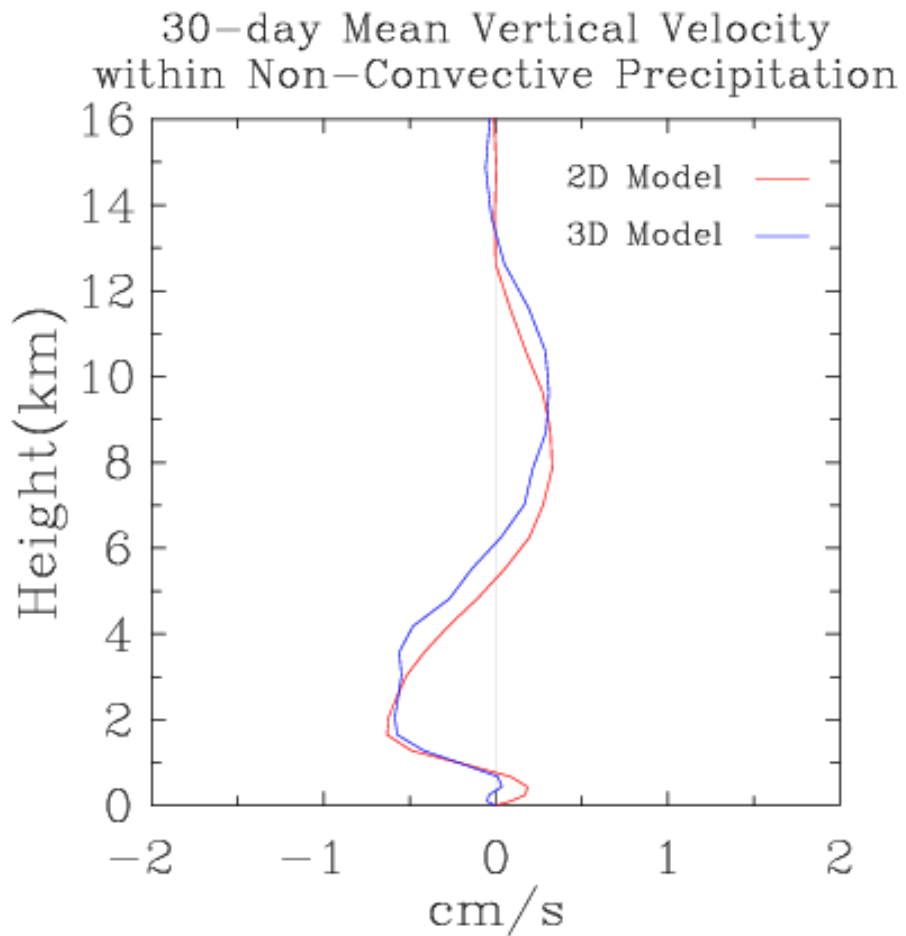


**Figure 35.** Vertical profile of time and domain averaged model simulated vertical motion within non-convective precipitation. Red represents the 2D model while blue represents the 3D model.

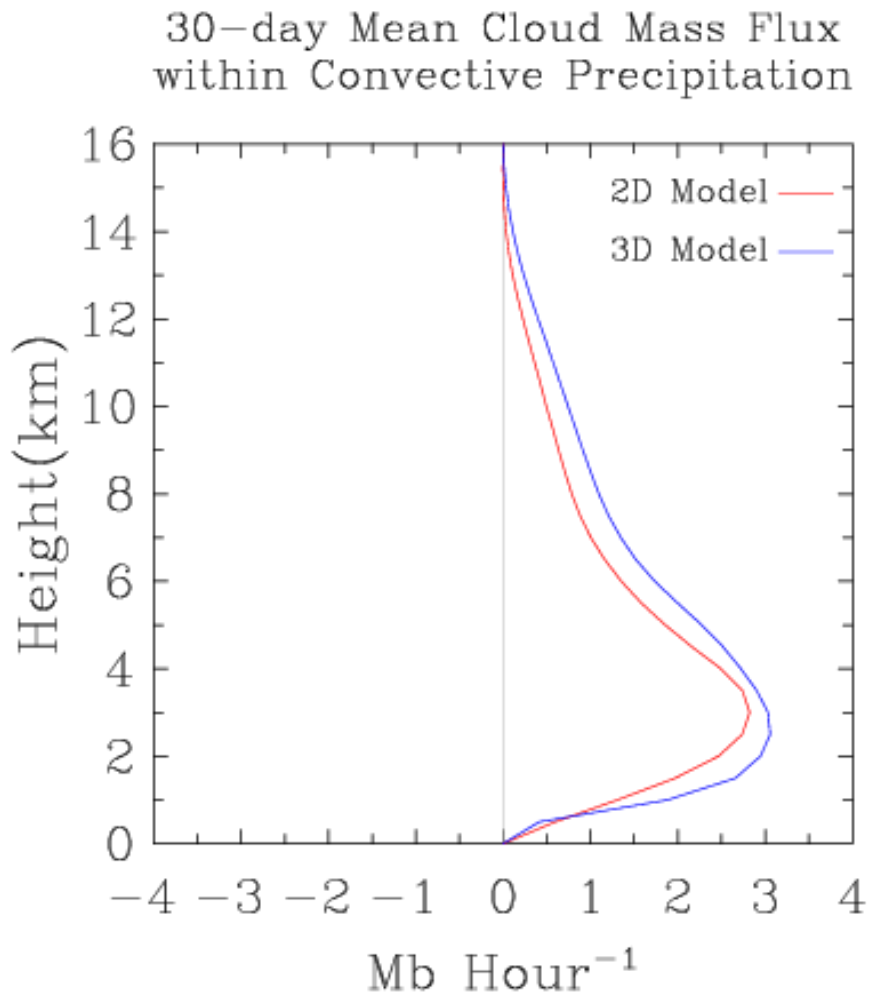


**Figure 36.** Vertical profile of time and domain averaged cloud mass flux within convective precipitation. Red represents the 2D model while blue represents the 3D model.

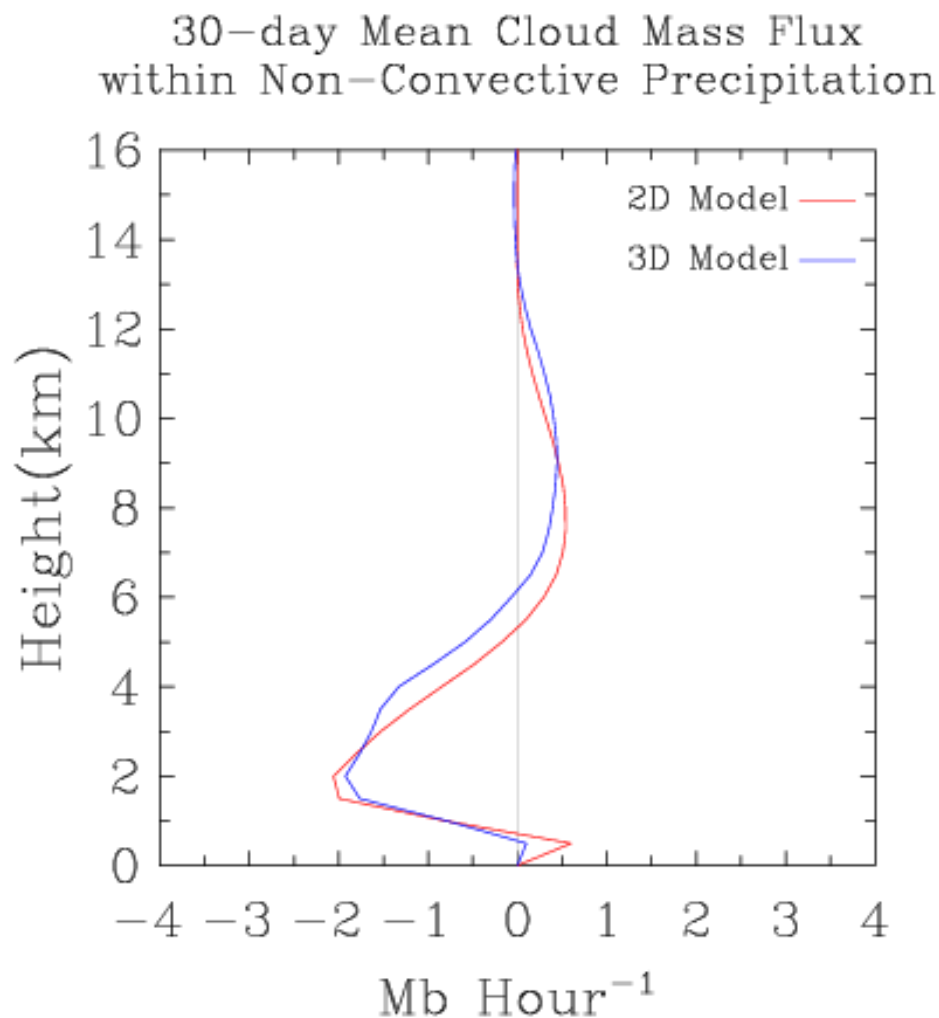


**Figure 37.** Vertical profile of time and domain averaged cloud mass flux within non-convective precipitation. Red represents the 2D model while blue represents the 3D model.

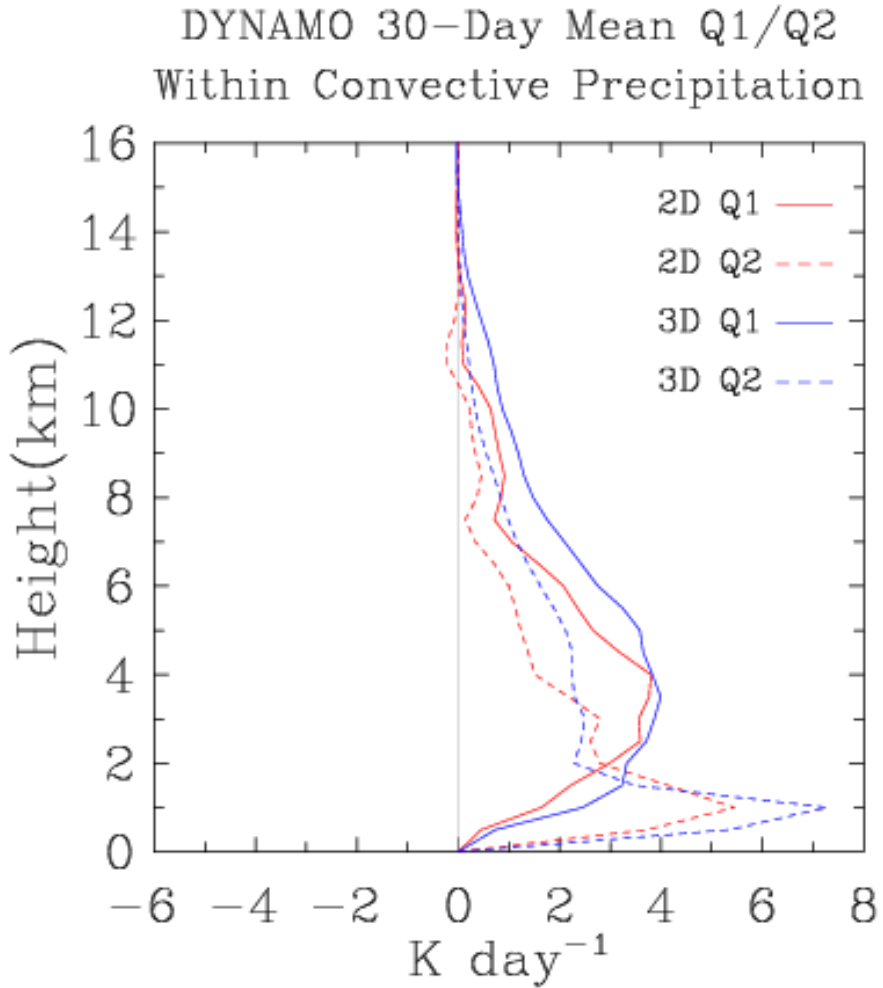


**Figure 38.** Vertical profile of time and domain averaged  $Q_1$  and  $Q_2$  over the Northern Sounding Array during convective precipitation. Red represents the 2D model while blue represents the 3D model. Solid lines depict  $Q_1$  and dashed lines depict  $Q_2$ .

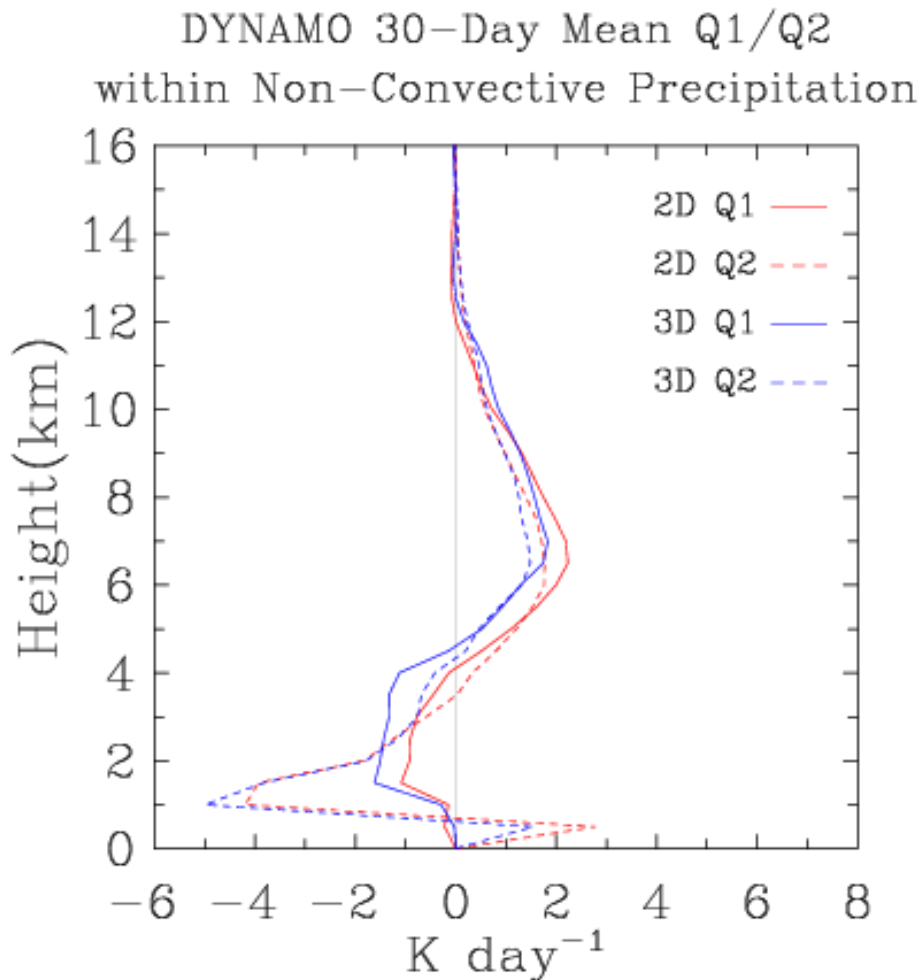


**Figure 39.** Vertical profile of time and domain averaged  $Q_1$  and  $Q_2$  over the Northern Sounding Array during non-convective precipitation. Red represents the 2D model while blue represents the 3D model. Solid lines depict  $Q_1$  and dashed lines depict  $Q_2$ .

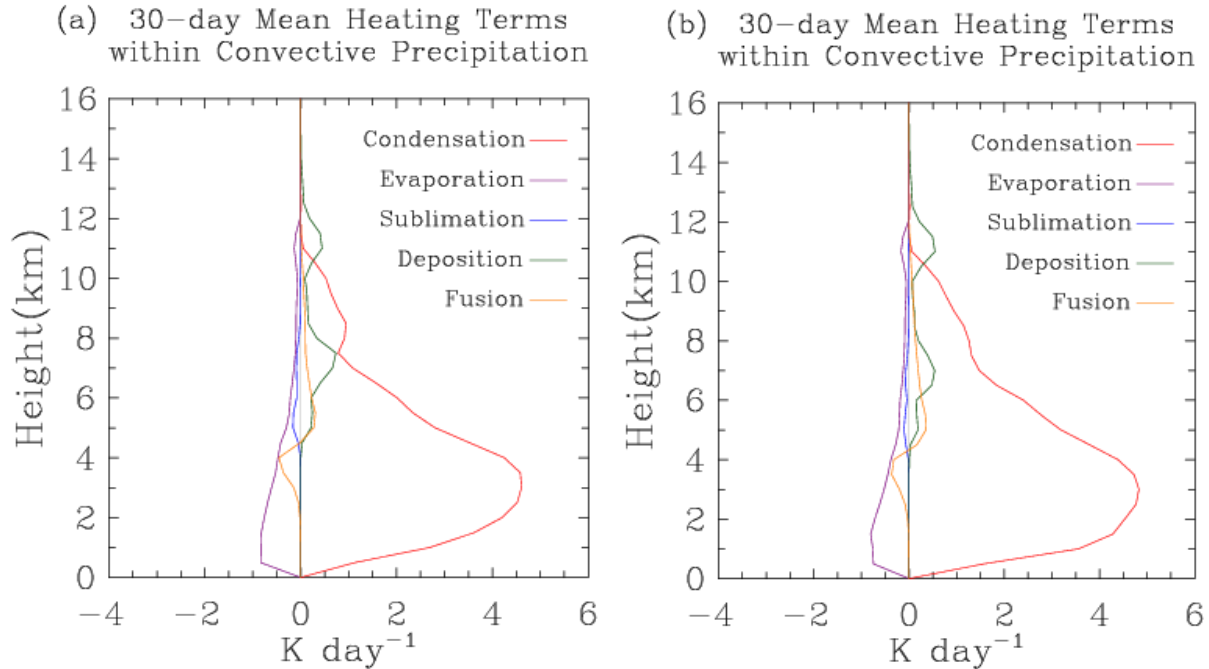


**Figure 40.** Vertical profile of time and domain averaged 2D (a) and 3D (b) model simulated convective mean heating terms over the Northern Sounding Array. Red represents condensation, purple represents evaporation, blue represents sublimation, green represents deposition, and yellow represents fusion.

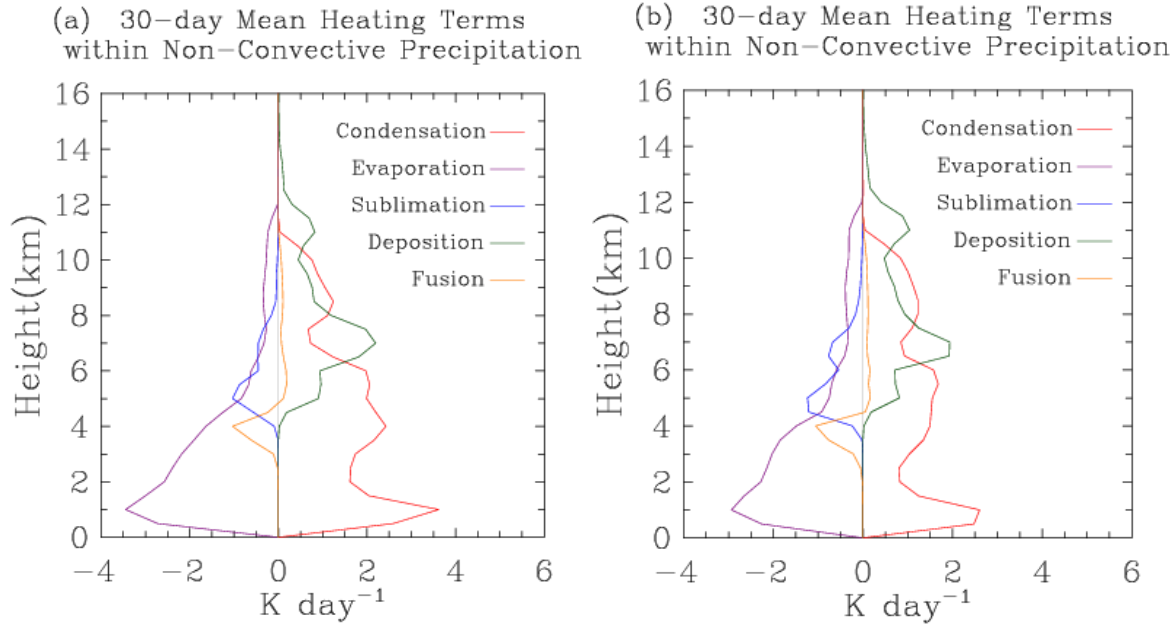


**Figure 41.** Vertical profile of time and domain averaged 2D (a) and 3D (b) model simulated non-convective mean heating terms over the Northern Sounding Array. Red represents condensation, purple represents evaporation, blue represents sublimation, green represents deposition, and yellow represents fusion.

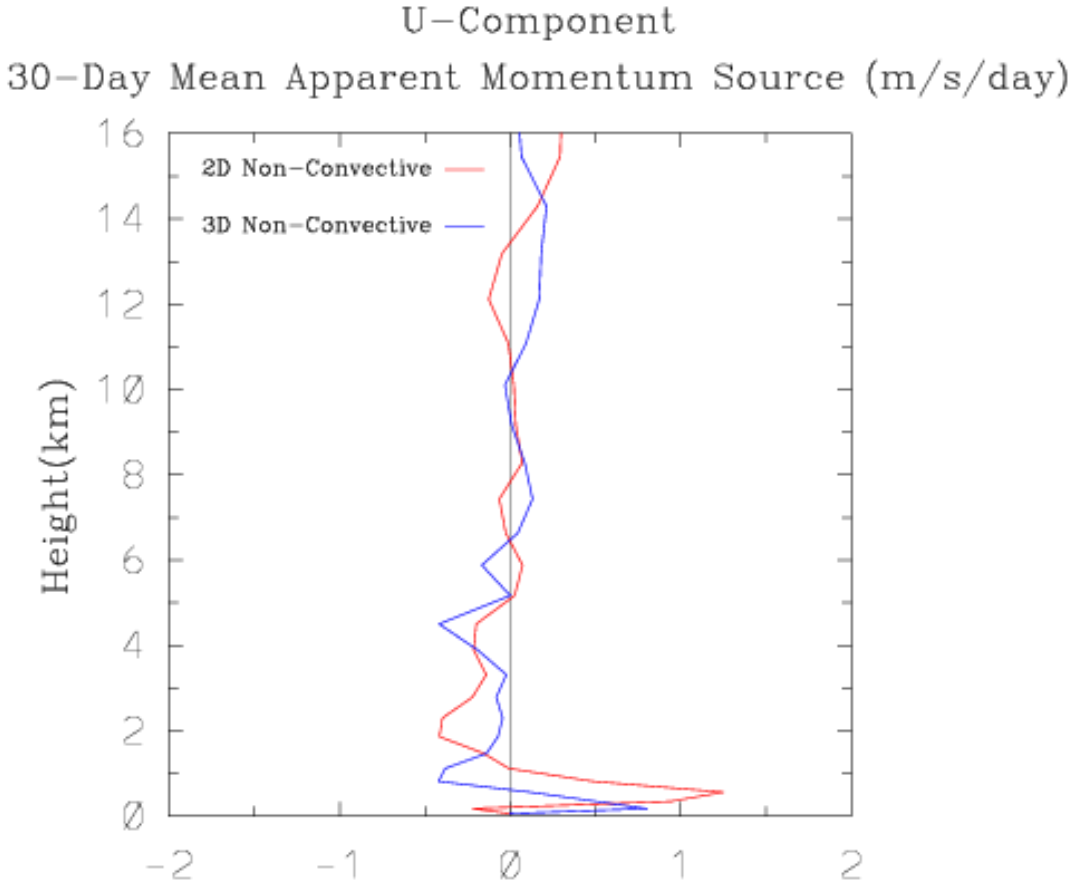


**Figure 42.** Vertical profile of time and domain averaged apparent momentum source within non-convective clouds. Red represents the 2D model while blue represents the 3D model.

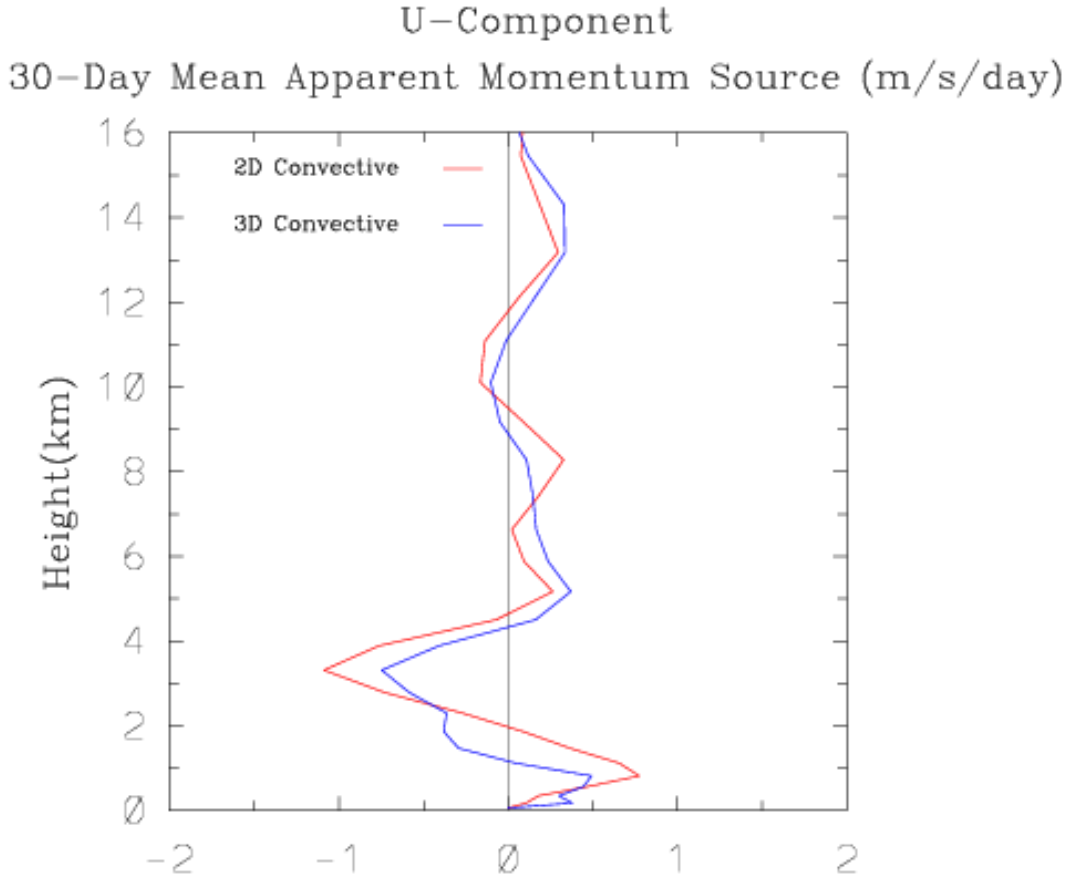


**Figure 43.** Vertical profile of time and domain averaged apparent momentum source within convective clouds. Red represents the 2D model while blue represents the 3D model.

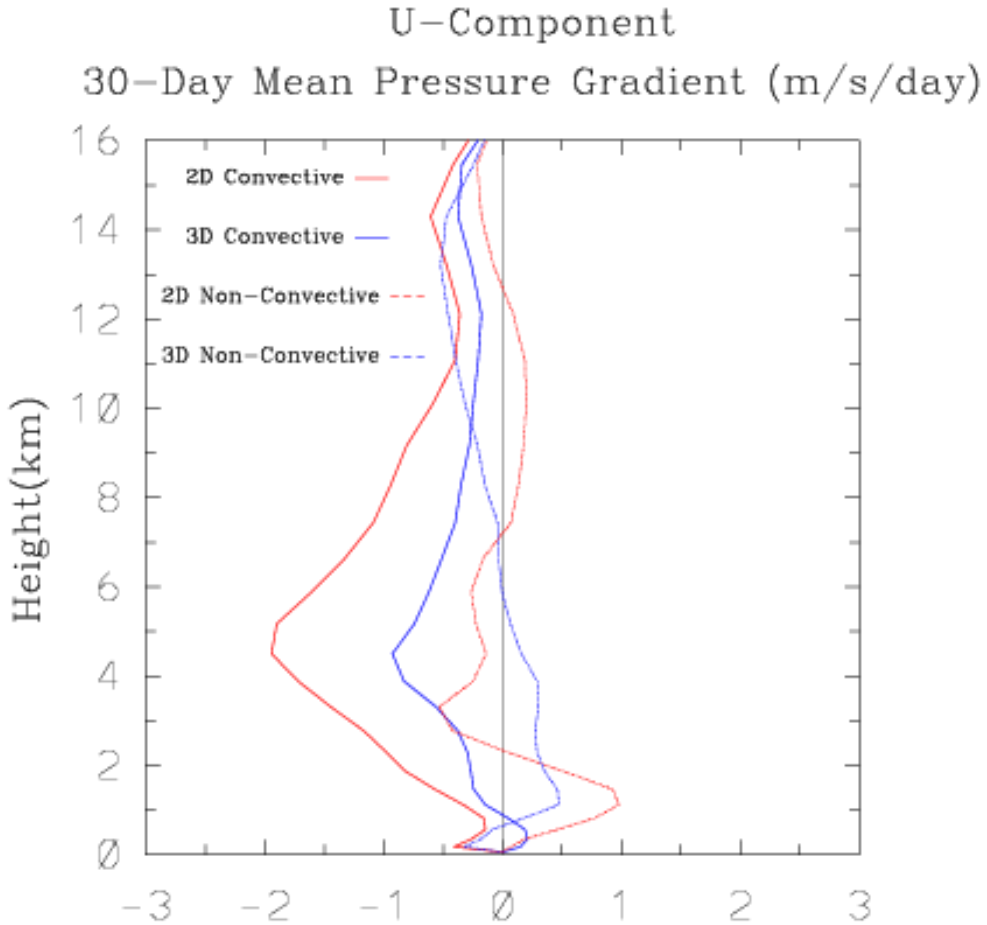


**Figure 44.** Vertical profile of time and domain averaged pressure gradient within convective and non-convective clouds. Red lines represent the 2D model while blue lines represent the 3D model. Solid lines depict convective values and dashed lines represent non-convective values.

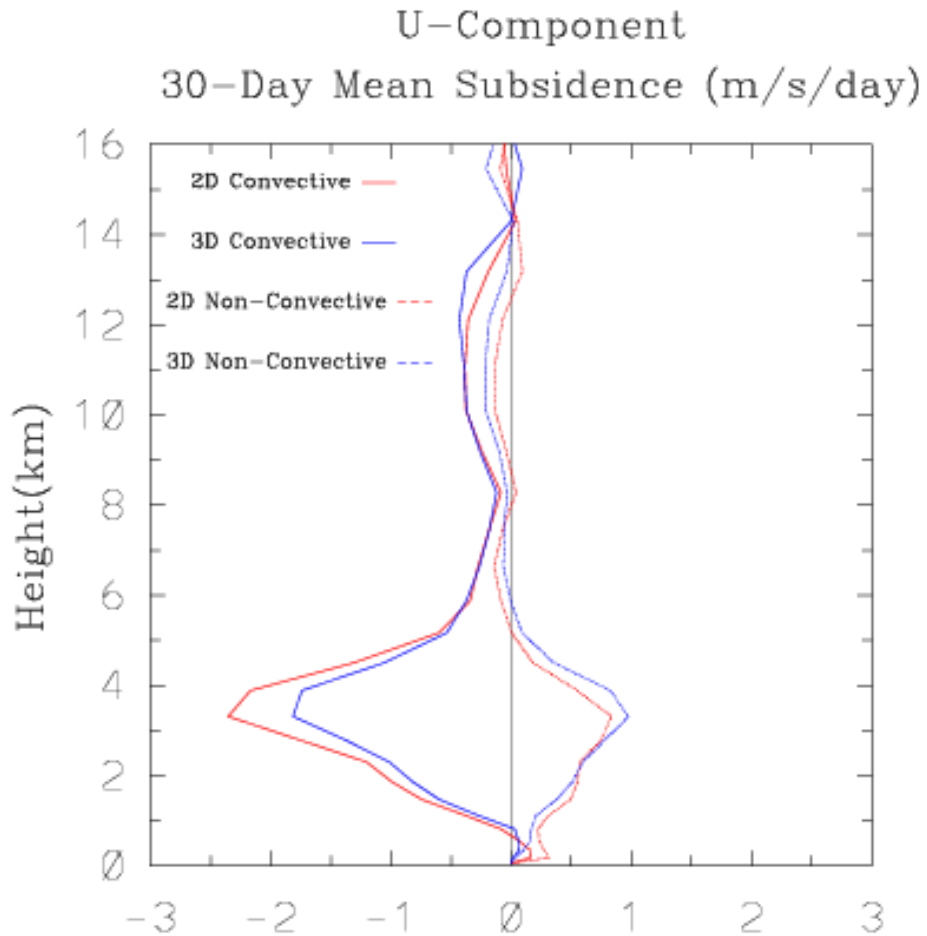


**Figure 42.** Vertical profile of time and domain averaged subsidence within convective and non-convective clouds. Red lines represent the 2D model while blue lines represent the 3D model. Solid lines depict convective values and dashed lines represent non-convective values.

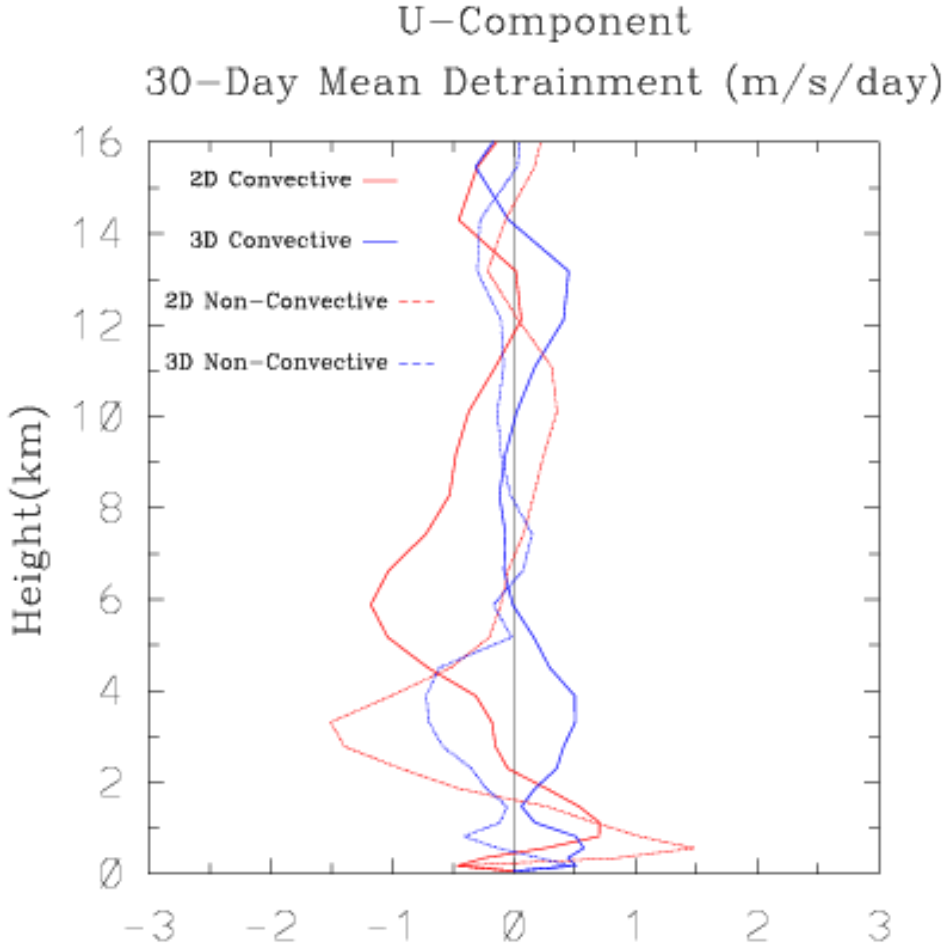


**Figure 43.** Vertical profile of time and domain averaged detrainment within convective and non-convective clouds. Red lines represent the 2D model while blue lines represent the 3D model. Solid lines depict convective values and dashed lines represent non-convective values.

**Table 1.** Mean and standard deviation values of 3D simulated radiative fluxes and 2D simulated radiative fluxes in W/m<sup>2</sup>.

	TOA LW Up	TOA SW Down	TOA SW Up	SFC LW Down	SFC LW Up	SFC SW Down	SFC SW Up
2D	214.956 ± 59.857	422.300 ± 75.923	105.327 ± 55.198	406.032 ± 73.922	473.796 ± 85.100	242.407 ± 74.702	10.770 ± 2.761
3D	221.770 ± 56.369	422.300 ± 75.923	109.208 ± 53.673	410.053 ± 74.733	473.781 ± 85.097	237.513 ± 72.260	10.535 ± 2.725

**Table 2.** Mean and standard deviation values of 3D simulated phase change heating terms and 2D simulated phase change heating terms.

	Condensation	Evaporation	Deposition	Sublimation	Fusion
2D	2.658 ± 2.612	-1.223 ± 1.453	0.903 ± 1.046	-0.304 ± 0.514	-0.001 ± 0.378
3D	2.708 ± 2.516	-1.125 ± 1.320	0.832 ± 0.933	-0.373 ± 0.632	0.014 ± 0.411

## REFERENCES

- Arakawa, A. and W.H. Schubert, 1974: Interaction of a Cumulus Cloud Ensemble with the Large-Scale Environment, Part I. *J. Atmos. Sci.*, 31, 674–01.
- Arakawa, A., 2004: The Cumulus Parameterization Problem: Past, Present, and Future. *J. Climate*, 17, 2493–2525.
- Asai, T., 1970: Three-dimensional features of thermal convection in a plane Couette flow. *J. Meteor. Soc. Japan*, 48, 18–29.
- Blade, I., and D. L. Hartmann, 1993: Tropical intraseasonal oscillation in a simple nonlinear model. *J. Atmos. Sci.*, 50, 2922–2939.
- Bony, S., B. Stevens, D.M.W. Dargan, C. Jakob, M. Kageyama, et al., 2015: Clouds, circulation and climate sensitivity. *Nature Geoscience*, 8, 261–268.
- Browning, K. A., 1990: Rain, rainclouds and climate. *Quart. J. Roy. Meteor. Soc.*, 116, 1025–1051.
- Cess, R., and Coauthors, 1990: Intercomparison and interpretation of climate feedback processes in 19 atmospheric general circulation models. *J. Geophys. Res.*, 95, 16 601–16 615.
- Chahine, M. T., 1992: The hydrological cycle and its influence on climate. *Nature*, 359, 373–380.
- Clark, T. L., W. D. Hall, and J. L. Coen, 1996: Source code documentation for the Clark-Hall cloud-scale model: Code version G3CH01. NCAR Tech. Note NCAR/TN-426+STR, 137.
- Donner, L.J., 1993: A Cumulus Parameterization Including Mass Fluxes, Vertical Momentum Dynamics, and Mesoscale Effects. *J. Atmos. Sci.*, 50, 889–906.
- Donner, L.J., C.J. Seman, and R.S. Hemler, 1999: Three-Dimensional Cloud-System Modeling of GATE Convection. *J. Atmos. Sci.*, 56, 1885–1912.
- Emanuel, K.A., 1991: A Scheme for Representing Cumulus Convection in Large-Scale Models. *J. Atmos. Sci.*, 48, 2313–2329.
- Fan, J. et al., 2017: Cloud-resolving model intercomparison of an MC3E squall line case: Part I—Convective updrafts, *J. Geophys. Res. Atmos.*, 122, 9351–9378.
- Feng, Z., S.A. McFarlane, C. Schumacher, S. Ellis, J. Comstock, and N. Bharadwaj, 2014: Constructing a Merged Cloud–Precipitation Radar Dataset for Tropical Convective Clouds during the DYNAMO/AMIE Experiment at Addu Atoll. *J. Atmos. Oceanic Technol.*, 31, 1021–1042.

- Ferrier, B., 1994: A Double-Moment Multiple-Phase Four-Class Bulk Ice Scheme. Part I: Description. *J. Atmos. Sci.*, 51, 249–280.
- Grabowski, W.W., X. Wu, M.W. Moncrieff, 1996: Cloud-Resolving Modeling of Tropical Cloud Systems during Phase III of GATE. Part I: Two-Dimensional Experiments. *Journal of the Atmospheric Sciences*, 53, 3684–3709.
- Grabowski, W.W., X. Wu, M. W. Moncrieff, and D. Hall, 1998: Cloud-resolving modeling of cloud systems during Phase III of GATE. Part II: Effects of resolution and the third spatial dimension. *J. Atmos. Sci.*, 55, 3264–3282.
- Grabowski, W.W., 2001: Coupling Cloud Processes with the Large-Scale Dynamics Using the Cloud-Resolving Convection Parameterization (CRCP). *J. Atmos. Sci.*, 58, 978–997.
- Guichard, F. and F. Couvreux, 2017: A short review of numerical cloud-resolving models. *Tellus A: Dynamic Meteorology and Oceanography*, 69.
- Hendon, H. H. and B. Liebmann, 1990: The intraseasonal (30–50 day) oscillation of the Australian summer monsoon. *J. Atmos. Sci.*, 47, 2909–2923.
- IPCC, 1995: Climate change 1995. The Science of Climate Change, J. T. Houghton, L. G. Meira Filho, B. A. Callander, N. Harris, A. Kattenberg, and K. Maskell, Eds., Cambridge University Press, 193–227.
- Johnson, R.H. and P.E. Ciesielski, 2013: Structure and Properties of Madden–Julian Oscillations Deduced from DYNAMO Sounding Arrays. *J. Atmos. Sci.*, 70, 3157–3179.
- Kessler, E., 1969: On the Distribution and Continuity of Water Substance in Atmospheric Circulations. *Meteor. Monogr.*, No. 32, Amer. Meteor. Soc., 84.
- Khairoutdinov, M. F., and D. A. Randall (2001), A cloud resolving model as a cloud parameterization in the NCAR Community Climate System Model: Preliminary results, *Geophys. Res. Lett.*, 28, 3617–3620.
- Kiehl, J. T., J. J. Hack, G. B. Bonan, B. A. Boville, B. P. Briegleb, D. L. Williamson, and P. J. Rasch, 1996: Description of the NCAR Community Climate Model (CCM3). NCAR Tech. Note TN-420+STR, 152.
- Klotzbach, P.J., 2014: The Madden–Julian Oscillation’s Impacts on Worldwide Tropical Cyclone Activity. *J. Climate*, 27, 2317–2330.
- Koenig, L.R., 1972: Parameterization of Ice Growth for Numerical Calculations of Cloud Dynamics. *Mon. Wea. Rev.*, 100, 417–423.
- Koenig, L. R., and F. W. Murray, 1976: Ice-bearing cumulus cloud evolution: Numerical simulation and general comparison against observations. *J. Appl. Meteor.*, 15, 747–762.

- Krishnamurti, T.N., H.S.Bedi, V.M.Hardiker, and L.Ramaswamy, 1998: An Introduction to Global Spectral Modeling. New York : Oxford University Press, 146-147.
- Kuo, H.L., 1965: On Formation and Intensification of Tropical Cyclones Through Latent Heat Release by Cumulus Convection. *J. Atmos. Sci.*, 22, 40-63.
- Labbouz, L., Z. Kipling, P. Stier, and A. Protat, 2018: How Well Can We Represent the Spectrum of Convective Clouds in a Climate Model? Comparisons between Internal Parameterization Variables and Radar Observations. *J. Atmos. Sci.*, 75.
- Lang, S., W. Tao, J. Simpson, and B. Ferrier, 2003: Modeling of Convective–Stratiform Precipitation Processes: Sensitivity to Partitioning Methods. *J. Appl. Meteor.*, 42, 505–527.
- Li, F., D. Rosa, W. D. Collins, and M. F. Wehner (2012), “Super-parameterization”: A better way to simulate regional extreme precipitation? *J. Adv. Model. Earth Syst.*, 4, M04002.
- Madden, R.A. and P.R. Julian, 1971: Detection of a 40–50 Day Oscillation in the Zonal Wind in the Tropical Pacific. *J. Atmos. Sci.*, 28, 702–708.
- Madden, R.A. and P.R. Julian, 1972: Description of Global-Scale Circulation Cells in the Tropics with a 40–50 Day Period. *J. Atmos. Sci.*, 29, 1109–1123.
- Mapes, B. E., S. Tulich, J. Lin, and P. Zuidema, 2006: The mesoscale convection life cycle: Building block or prototype for large-scale tropical waves? *Dyn. Atmos. Oceans*, 42, 3–29.
- Moeng, C., W.R. Cotton, C. Bretherton, A. Chlond, M. Khairoutdinov, S. Krueger, W.S. Lewellen, M.K. MacVean, J.R. Pasquier, H.A. Rand, A.P. Siebesma, B. Stevens, and R.I. Sykes, 1996: Simulation of a Stratocumulus-Topped Planetary Boundary Layer: Intercomparison among Different Numerical Codes. *Bull. Amer. Meteor. Soc.*, 77, 261–278.
- Moncrieff, M.W., S.K. Krueger, D. Gregory, J. Redelsperger, and W. Tao, 1997: GEWEX Cloud System Study (GCSS) Working Group 4: Precipitating Convective Cloud Systems. *Bull. Amer. Meteor. Soc.*, 78, 831–846.
- Morrison, H. and J.A. Milbrandt, 2015: Parameterization of Cloud Microphysics Based on the Prediction of Bulk Ice Particle Properties. Part I: Scheme Description and Idealized Tests. *J. Atmos. Sci.*, 72, 287–311.
- Morrison, H., 2016: Impacts of Updraft Size and Dimensionality on the Perturbation Pressure and Vertical Velocity in Cumulus Convection. Part II: Comparison of Theoretical and Numerical Solutions and Fully Dynamical Simulations. *J. Atmos. Sci.*, 73, 1455–1480.

- Phillips, V. T. J., and L. J. Donner, 2006: Cloud microphysics, radiation and vertical velocities in two- and three-dimensional simulations of deep convection. *Quart. J. Roy. Meteor. Soc.*, 132, 3011–3033.
- Randall, D., M. Khairoutdinov, A. Arakawa, and W. Grabowski, 2003: Breaking the Cloud Parameterization Deadlock. *Bull. Amer. Meteor. Soc.*, 84, 1547–1564.
- Redelsperger, J. L., and Coauthors, 2000: A GCSS model intercomparison for a tropical squall line observed during TOGA-COARE. I: Cloud-resolving models. *Quart. J. Roy. Meteor. Soc.*, 126, 823–863.
- Roundy, P.E., 2008: Analysis of Convectively Coupled Kelvin Waves in the Indian Ocean MJO. *J. Atmos. Sci.*, 65, 1342–1359.
- Schlesinger, R. E., 1984: Effects of the pressure perturbation field in numerical models of unidirectionally sheared thunderstorm convection: Two versus three dimensions. *J. Atmos. Sci.*, 41, 1571–1587.
- Schneider, T., C.M. Kaul, and K.G. Pressel, 2019: Possible climate transitions from breakup of stratocumulus decks under greenhouse warming. *Nature Geoscience*, 12, 163–167.
- Skamarock, W.C., M.L. Weisman, and J.B. Klemp, 1994: Three-Dimensional Evolution of Simulated Long-Lived Squall Lines. *J. Atmos. Sci.*, 51, 2563 -2584.
- Stephens, G.L., 2005: Cloud Feedbacks in the Climate System: A Critical Review. *J. Climate*, 18, 237–273.
- Sullivan, S. C., D. Lee, L. Oreopoulos, and A. Nenes, 2016: Role of updraft velocity in temporal variability of global cloud hydrometeor number. *Proc. Natl. Acad. Sci. USA*, 113, 5791–5796.
- Tang, Y., and B. Yu (2008), MJO and its relationship to ENSO, *J. Geophys. Res.*, 113, D14106.
- Tao, W. and S. Soong, 1986: A Study of the Response of Deep Tropical Clouds to Mesoscale Processes: Three-Dimensional Numerical Experiments. *J. Atmos. Sci.*, 43, 2653–2676.
- Tao, W.-K., J. Simpson, and S.-T. Soong, 1987: Statistical properties of a cloud ensemble: A numerical study. *J. Atmos. Sci.*, 44, 3175–3187.
- Tao, W., D. Johnson, C. Shie, and J. Simpson, 2004: The Atmospheric Energy Budget and Large-Scale Precipitation Efficiency of Convective Systems during TOGA COARE, GATE, SCSMEX, and ARM: Cloud-Resolving Model Simulations. *J. Atmos. Sci.*, 61, 2405–2423.
- Tiedtke, M., 1989: A Comprehensive Mass Flux Scheme for Cumulus Parameterization in Large-Scale Models. *Mon. Wea. Rev.*, 117, 1779–1800.

- Tompkins, A. M., 2000: The Impact of Dimensionality on Long-Term Cloud-Resolving Model Simulations. *Mon. Wea. Rev.*, 128, 1521–1535.
- Webb M. J. et al., 2015. The impact of parametrized convection on cloud feedback. *Phil. Trans. R. Soc. A* 373.
- Wilhelmson, R., 1974: The Life Cycle of a Thunderstorm in Three Dimensions. *J. Atmos. Sci.*, 31, 1629–1651.
- Wu, X., W.W. Grabowski, M.W. Moncrieff, 1998: Long-Term Behavior of Cloud Systems in TOGA COARE and Their Interactions with Radiative and Surface Processes. Part I: Two-Dimensional Modeling Study. *Journal of the Atmospheric Sciences*, 55, 2693-2714.
- Wu, X., W. Hall, W.W. Grabowski, M.W. Moncrieff, W.D. Collins, and J.T. Kiehl, 1999: Long-Term Behavior of Cloud Systems in TOGA COARE and Their Interactions with Radiative and Surface Processes. Part II: Effects of Ice Microphysics on Cloud-Radiation Interaction. *Journal of the Atmospheric Sciences*, 56, 3177-3195.
- Wu, X., X. Liang, and S. Park, 2007: Cloud-Resolving Model Simulations over the ARM SGP. *Mon. Wea. Rev.*, 135, 2841–2853.
- Xu, K.-M., and D. A. Randall, 1996: Explicit simulation of cumulus ensembles with the GATE Phase III data: Comparison with observations. *J. Atmos. Sci.*, 53, 3709–3736.
- Xu, W. and S.A. Rutledge, 2014: Convective Characteristics of the Madden–Julian Oscillation over the Central Indian Ocean Observed by Shipborne Radar during DYNAMO. *J. Atmos. Sci.*, 71, 2859–2877.
- Yanai, M., S. Esbensen, and J. Chu, 1973: Determination of Bulk Properties of Tropical Cloud Clusters from Large-Scale Heat and Moisture Budgets. *J. Atmos. Sci.*, 30, 611–627.
- Zeng, X. and Coauthors, 2007: Evaluating Clouds in Long-Term Cloud Resolving Model Simulations with Observational Data. *J. Atmos. Sci.*, 64, 4153-4177.
- Zeng, X., W.-K. Tao, S. Lang, A. Y. Hou, M. Zhang, and J. Simpson, 2008: On the sensitivity of atmospheric ensembles to cloud microphysics in long-term cloud-resolving model simulations. *J. Meteor. Soc. Japan*, 86A, 45–65.
- Zhang, C., 2005: Madden-Julian Oscillation, *Rev. Geophys.*, 43, RG2003.
- Zhang, G., X. Wu, 2003: Convective momentum transport and perturbation pressure field from a cloud-resolving model simulation. *Journal of the Atmospheric Sciences*. 60,1120-1139.

Zhao, M., J. Golaz, I.M. Held, V. Ramaswamy, S. Lin, Y. Ming, P. Ginoux, B. Wyman, L.J. Donner, D. Paynter, and H. Guo, 2016: Uncertainty in Model Climate Sensitivity Traced to Representations of Cumulus Precipitation Microphysics. *J. Climate*, 29, 543–560.